

**University of Alberta**

**Biochemical Imaging of Gliomas Using MR Spectroscopic Imaging for  
Radiotherapy Treatment Planning**

by

**Amr Ahmed Heikal**

A thesis submitted to the Faculty of Graduate Studies and Research  
in partial fulfillment of the requirements for the degree of

**Doctor of Philosophy**

in

**Medical Physics**

**Department of Physics**

©Amr Ahmed Heikal

Spring 2014

Edmonton, Alberta

Permission is hereby granted to the University of Alberta Libraries to reproduce single copies of this thesis and to lend or sell such copies for private, scholarly or scientific research purposes only. Where the thesis is converted to, or otherwise made available in digital form, the University of Alberta will advise potential users of the thesis of these terms.

The author reserves all other publication and other rights in association with the copyright in the thesis and, except as herein before provided, neither the thesis nor any substantial portion thereof may be printed or otherwise reproduced in any material form whatsoever without the author's prior written permission

To my wife and my daughter,

Dalia and Lena

## **Abstract**

This thesis discusses the main obstacles facing wide clinical implementation of magnetic resonance spectroscopic imaging (MRSI) as a tumor delineation tool for radiotherapy treatment planning, particularly for gliomas. These main obstacles are identified as 1. observer bias and poor interpretational reproducibility of the results of MRSI scans, and 2. the long scan times required to conduct MRSI scans. An examination of an existing user-independent MRSI tumor delineation technique known as the choline-to-NAA index (CNI) is conducted to assess its utility in providing a tool for reproducible interpretation of MRSI results. While working with spatial resolutions typically twice those on which the CNI model was originally designed, a region of statistical uncertainty was discovered between the tumor and normal tissue populations and as such a modification to the CNI model was introduced to clearly identify that region. To address the issue of long scan times, a series of studies were conducted to adapt a scan acceleration technique, compressed sensing (CS), to work with MRSI and to quantify the effects of such a novel technique on the modulation transfer function (MTF), an important quantitative imaging metric. The studies included the development of the first phantom based method of measuring the MTF for MRSI data, a study of the correlation between the k-space sampling patterns used for compressed sensing and the resulting MTFs, and the introduction of a technique circumventing some of side-effects of compressed sensing by exploiting the conjugate symmetry property of k-space. The work in this thesis provides two essential steps towards wide clinical implementation of MRSI-based tumor delineation. The proposed modifications to the CNI method coupled with the application of CS to MRSI address the two main obstacles outlined. However, there continues to be room for improvement and questions that need to be answered by future research.

## Acknowledgments

I would like to dedicate this thesis to my wife, Dalia. Words cannot begin to express what you have done for me. You truly are the best thing that ever happened to me. You have always supported me and you have always been my rock in hard times before good. You are the one who convinced me to pursue my dream and not settle for less. You have always believed in me even when it involved starting a new life in a new country and even pursuing a career in research as frustrating as that can sometime be. Above all you are the most wonderful mother and the most loving wife. You are one of a kind and no matter how much I write it will never be enough to thank you for what you have done for me and our family.

Lena you are too young to understand why your “Baba” was too busy all that time. I promise I will make up for it from now on. You have been such an amazing girl and I am so proud of you. I want you to know that you will always be my little girl.

Dr. Fallone, thank you for accepting me into this program and giving me the chance to change my career and my life. This program was and still is a great experience. Thank you for your support scientifically and financially. You have always provided great supervision, direction and feedback for my work. Dr. Wachowicz, shall I thank you for the endless discussions we had in CBIAR upstairs or CBIAR downstairs? You have always provided excellent supervisions and great feedback and support for my work as well as great insight. We have attempted some bold moves in this research, and I thank you for your encouragement. It isn't easy swimming against the tide. Dr. Robinson and Dr. Riauka, thank you for all the direction you've provided by being member of my supervisory committee. Dr. Murray, and Dr. Urtasun, thank you for your support and for the biological and clinical knowledge you bring to the table. Medical physics is a true interdisciplinary field and your feedback enriched my work. Dr. Yahya, while you have served for a very short period on my

committee it is great to have a resource like yourself for all the ambitious spectroscopy research conducted in this department.

To my mother and my brothers, Khaled and Hesham, I cannot thank you enough. You have been so supportive and encouraging. Unfortunately I don't get to see you often enough yet you are always there when I need you and I truly appreciate our close knit family.

Over the years I have been blessed by having great colleagues and officemates, most of whom have graduated and moved on to great careers. Every single one of them has had a positive influence on me as a person and as a would-be academic. While many have been thanked in my MSc Thesis, I would like to thank those who I have been lucky to know since. Tony, Joel and Katie, you are what I aspire to be as an academic. You set the standard for the model researcher and I will keep pointing at your work ethic as the example to follow for each new graduate student I meet. Jay, my fellow previous senior student, I wish you all the best in your career; you are a very bright man and I hope we take our CCPM exams together along with Danny and Moti. Eugene, I will miss your controversial discussion topic of the day, but I am certain that you'll have as illustrious career as an MRI scientist. Danielle, you are another example of the model PhD student I mentioned above. I wish you all the best in your research, and I hope you keep arguing with Eugene over his controversial topics. Andrei and Jean-David, my lunch-time comrades, I want you to know that there is a light at the end of the tunnel, just keep your heads down and keep going. Derek, Devin, Dan Michael, Danny, Moti, and Ayhan, my across the hall neighbors, I wish you all the best in your research and/or careers, but know that I will never forgive you for exporting Eugene to our office. Michael, good luck in your research and your karate. I want you to know that you are my target in the next 5K COMP fun run. David, you are very intelligent person and I wish you all the best. The other Amir, you are a very special man. I admire your work ethic and your sense of humor; I will miss both. Dylan, Brennan, Brian,

Hali and Daniel, I haven't gotten to know all of you very well except for Hali, my officemate, but I know that this is very hard program to get into and I wish you all the best in your chosen careers. It will take hard work but you will appreciate it later.

Finally to all Medical Physics, Physics and Oncology professors, mentors, staff, and the many friends I have made of the years, thank you for making this program as great as it is. This experience wouldn't have been as great as it was without you.

<b>CHAPTER ONE.....</b>	<b>1</b>
<b>1 INTRODUCTION .....</b>	<b>1</b>
1.1 ASTROCYTOMAS.....	1
1.2 THE RADIOTHERAPY PROCESS .....	2
1.3 IMAGING AND THE RADIOTHERAPY PROCESS .....	3
1.3.1 <i>Diagnostic and 3-D Imaging</i> .....	3
1.3.2 <i>MRI and Tumor Delineation</i> .....	4
1.3.3 <i>MRI vs. CT</i> .....	6
1.4 TREATMENT PLANNING .....	6
1.5 TREATMENT DELIVERY .....	8
<b>CHAPTER TWO.....</b>	<b>15</b>
<b>2 THEORY OF MAGNETIC RESONANCE IMAGING.....</b>	<b>15</b>
2.1 INTRODUCTION.....	15
2.2 QUANTUM MECHANICAL DESCRIPTION OF NMR .....	15
2.2.1 <i>Spin 1/2 in a static magnetic field (preparation)</i> .....	15
2.3 THE CLASSICAL DESCRIPTION OF NMR .....	18
2.3.1 <i>Magnetic moments in a static magnetic field B<sub>0</sub> (preparation)</i> .....	18
2.3.2 <i>The excitation process</i> .....	19
2.3.3 <i>Description of the signal-inducing excited state (acquisition stage)</i> .....	24
2.4 RELAXATION MECHANISMS AND THE BLOCH EQUATIONS .....	27
2.4.1 <i>Longitudinal relaxation</i> .....	27
2.4.2 <i>Transverse Relaxation</i> .....	29
2.5 SPATIAL ENCODING.....	31
2.5.1 <i>Slice Selection</i> .....	32
2.5.1.1 <i>Radio-Frequency excitation pulses</i> .....	34
2.5.2 <i>Frequency Encoding</i> .....	35
2.5.3 <i>Phase Encoding</i> .....	36
2.6 THE SIGNAL EQUATION .....	37
2.7 MR SPECTROSCOPY .....	40
2.8 LOCALIZATION TECHNIQUES OF MRS .....	41
2.8.1 <i>Stimulated Echo acquisition Mode (STEAM)</i> .....	42
2.8.2 <i>Point Resolved Spectroscopy (PRESS)</i> .....	42
2.8.3 <i>Spectroscopic Imaging (SI) (Chemical Shift Imaging)</i> .....	43
2.9 SIGNAL AND NOISE CONSIDERATIONS.....	45
2.9.1 <i>Signal</i> .....	45
2.9.2 <i>Noise</i> .....	46
2.9.3 <i>Signal-to-Noise Ratio (SNR)</i> .....	48
<b>CHAPTER THREE.....</b>	<b>50</b>
<b>3 AN UPDATED METHOD FOR AUTOMATIC TUMOR DELINEATION USING MRSI.....</b>	<b>50</b>
3.1 INTRODUCTION.....	50
3.2 MATERIALS AND METHODS.....	52
3.2.1 <i>MRSI sequence</i> .....	52
3.2.2 <i>Processing</i> .....	53
3.2.3 <i>Choline-to-NAA Index calculation</i> .....	53
3.2.4 <i>Tumor delineation</i> .....	55
3.3 RESULTS.....	57
3.4 DISCUSSION.....	61

3.4.1	<i>Correlation with Histology</i> .....	62
3.5	CONCLUSION .....	63
<b>CHAPTER FOUR.....</b>		<b>67</b>
<b>4 MTF BEHAVIOUR OF COMPRESSED SENSING MR SPECTROSCOPIC IMAGING .....</b>		<b>67</b>
4.1	INTRODUCTION.....	67
4.2	THEORY.....	69
4.2.1	<i>Modulation Transfer Function</i> .....	69
4.2.2	<i>Compressed Sensing</i> .....	70
4.3	MATERIALS AND METHODS.....	71
4.3.1	<i>Phantom</i> .....	71
4.3.2	<i>MTF calculation method</i> .....	72
4.3.3	<i>Sub-Nyquist Sampling</i> .....	74
4.3.4	<i>Imaging sequence</i> .....	75
4.3.5	<i>Simulated data</i> .....	76
4.3.6	<i>Reconstruction</i> .....	77
4.3.7	<i>Processing</i> .....	78
4.4	RESULTS AND DISCUSSION .....	79
4.5	CONCLUSIONS .....	86
<b>CHAPTER FIVE .....</b>		<b>90</b>
<b>5 EFFECT OF THE K-SPACE SAMPLING PATTERN ON THE MTF OF COMPRESSED SENSING MRSI .....</b>		<b>90</b>
5.1	INTRODUCTION.....	90
5.2	MATERIALS AND METHODS.....	93
5.2.1	<i>Phantom</i> .....	95
5.2.2	<i>Reconstruction</i> .....	96
5.2.3	<i>Processing</i> .....	97
5.2.4	<i>MTF calculation method</i> .....	98
5.2.5	<i>Sampling ratio</i> .....	98
5.3	RESULTS AND DISCUSSION .....	98
5.4	CONCLUSIONS .....	107
<b>CHAPTER SIX .....</b>		<b>110</b>
<b>6 CONJUGATE MAPPED COMPRESSED SENSING MRSI .....</b>		<b>110</b>
6.1	INTRODUCTION.....	110
6.2	THEORY.....	111
6.3	MATERIALS AND METHODS.....	113
6.3.1	<i>Imaging sequence</i> .....	113
6.3.2	<i>Conjugate Mapped Compressed Sensing (CmaCS)</i> .....	114
6.3.3	<i>Reconstruction</i> .....	115
6.3.4	<i>Processing</i> .....	116
6.3.5	<i>MTF calculation method</i> .....	116
6.4	RESULTS AND DISCUSSION .....	117
6.5	CONCLUSION: .....	121
<b>CHAPTER SEVEN .....</b>		<b>124</b>
<b>7 CONCLUSION AND FUTURE WORK.....</b>		<b>124</b>
7.1	CONCLUSION .....	124

7.2 FUTURE WORK.....	128
<b>BIBLIOGRAPHY.....</b>	<b>131</b>

## List of Tables

<b>Table 2-1: T1 value of different tissue at 1.5T and 3T. ....</b>	<b>28</b>
<b>Table 2-2: T2 values for brain tissue at 1.5 T.....</b>	<b>31</b>
<b>Table 3-1: Comparison between voxels designated as abnormal (CNI <math>\geq 2</math>) and voxels designated as uncertain (uncertainty limit <math>&gt; \text{CNI} \geq 2</math>) over twelve clinical subjects and three healthy volunteers. ....</b>	<b>60</b>

## List of Figures

Figure 2-1: The energy level diagram of a spin $\frac{1}{2}$ system observed in $B_0 = 0$ and $B_0 \neq 0$ .....	17
Figure 2-2: Magnetic moment vectors within a sample shown in: (a) The absence of a uniform external magnetic field resulting in random orientations zero net magnetization. (b) The magnetic moments are arranged in the parallel and anti-parallel orientation with respect to the applied magnetic field. The net magnetization vector $M_0$ resulting is shown as the big arrow.....	19
Figure 2-3: The rotating frame of reference $(x_p, y_p)$ with respect to the laboratory frame $(x, y)$ . The rotating frame rotates about the z-axis therefore, $z_p$ is equivalent to z.....	21
Figure 2-4: The magnetization vector precession about $B_{eff}$ in the rotating reference frame. ....	23
Figure 2-5: The motion of the magnetization vector during a $90^\circ$ excitation pulse shown in a. the laboratory frame and b. the rotating frame.....	24
Figure 2-6: Magnetization vector $M_0$ precessing in a negative sense about the z-axis in the presence of a static magnetic field $B_0$ applied along the z-direction.....	26
Figure 2-7: (a) the time domain induced e.m.f in the coil and (b) frequency profile of the detected signal. (Ignoring relaxation) .....	26
Figure 2-8: longitudinal relaxation of white matter at 3T following a $90^\circ$ pulse and an $180^\circ$ pulse. ....	29
Figure 2-9: longitudinal relaxation of white matter and grey matter at 3T following a $90^\circ$ pulse.....	29
Figure 2-10: Fluctuations in $\omega_0$ resulting in phase spread and loss of coherent signal.....	31
Figure 2-11: A description of the application of magnetic field gradients for spatial encoding.....	33
Figure 2-12: An ideal hard pulse envelope as shown in a. time domain and b. frequency domain. ....	34
Figure 2-13: An ideal soft pulse envelope as shown in a. time domain and b. frequency domain (assuming infinite time domain playtime).....	35

<b>Figure 2-14: a. Schematic of a gradient echo sequence. b. The k-space sampling trajectory caused by the application of the gradients in the sequence.....</b>	<b>39</b>
<b>Figure 2-15: Schematic for a STEAM sequence. The three 90° excitation pulses applied on the three orthogonal planes define a volume of interest (voxel) from which the signal is acquired. ....</b>	<b>42</b>
<b>Figure 2-16: Schematic of a PRESS Sequence. Similar to STEAM, the 90° excitation pulse along with the two 180° refocusing pulses applied on the three orthogonal planes define a volume of interest (voxel) from which the signal is acquired.....</b>	<b>43</b>
<b>Figure 2-17: A schematic of a 2-D PRESS sequence. ....</b>	<b>45</b>
<b>Figure 3-1: Histograms of CNI values for healthy volunteers.....</b>	<b>54</b>
<b>Figure 3-2: Histograms of CNI values for three GBM patients.....</b>	<b>54</b>
<b>Figure 3-3: Scatter plot of choline levels vs. NAA levels for a typical clinical GBM subject.....</b>	<b>56</b>
<b>Figure 3-4: T1 weighted contrast enhanced images of adjacent MRSI slices showing voxels with <math>CNI \geq 2</math>. ....</b>	<b>57</b>
<b>Figure 3-5: T1 weighted contrast enhanced images of adjacent MRSI slices showing voxels classified using the modified CNI method. Green voxels represent tumor, while white voxels represent voxels with mixed probability (uncertain).....</b>	<b>57</b>
<b>Figure 3-6: T1 weighted contrast enhanced image of a GBM patient showing spectra at different voxel locations. Peaks 1 and 2 correspond to choline and NAA, respectively. ....</b>	<b>59</b>
<b>Figure 3-7: T2 weighted contrast enhanced image of a healthy volunteer showing spectra at different voxel locations. Peaks 1 and 2 correspond to choline and NAA, respectively. The middle two columns show the preferential effect of CSF on the NAA peak.....</b>	<b>59</b>
<b>Figure 3-8: Percentage of VOI designated as abnormal and as uncertain for clinical subjects (n=12) and healthy volunteers (n=3). ....</b>	<b>61</b>
<b>Figure 4-1: Left: T2-weighted image of the phantom with the white box showing the MRSI field-of-view. Right: Fully sampled acetate area map. The high-lighted pie-shaped region the region of interest used for MTF calculation. The dashed arrow signifies the location of the arc profile</b>	

shown in Figure 2. The black box region is the uniform region used to normalize the arc profiles. ....	72
Figure 4-2: Arc profile of the acetate-area images along with the mathematically generated input modulation square wave .....	74
Figure 4-3: Frequency response of the arc profile of the acetate-area image .....	74
Figure 4-4: Left: The probability distribution function used for generating the k-space sampling pattern. Right: k-space sampling pattern used for 4-fold acceleration.....	75
Figure 4-5: Simulated phantom geometry along with the simulated MRSI grid showing metabolite peaks with and without noise .....	77
Figure 4-6: MTF of fully sampled simulations and showing the effect of processing filters and noise on the MTF.....	80
Figure 4-7: Calculated MTFs for CS reconstructions from simulation using varying weights for different peak SNRs .....	81
Figure 4-8: Calculated MTFs for simulated CS reconstructions using varying weights for a peak SNR value similar to that of the physical phantom.....	82
Figure 4-9: MTF of noiseless simulations using different CS reconstruction weights.....	83
Figure 4-10: The best MTF achievable for CS-MRSI over a wide range of peak SNR.....	84
Figure 4-11: Reconstructed MRSI spectra overlaid on T2-weighted images of the phantom.....	84
Figure 4-12: MTF of the experimental CS dataset compared to equivalent Nyquist-sampled low-resolution and the fully-sampled Fourier reconstructions .....	85
Figure 5-1: Examples of the probability distribution function (PDF) (left), a corresponding profile through the centre of k-space (middle) and an example of a corresponding k-space sampling pattern (right) for (a) a step, (b) a $1/r^2$ , and (c) a half-Gaussian PDF.....	95
Figure 5-2: (a) T2-weighted image of the phantom with the white box showing the MRSI field-of-view. (b) Fully sampled acetate area map. The high-lighted pie-shaped region the region of interest used for MTF	

calculation. The dashed arrow signifies the location of the arc profile shown in figure 2. The black box region is the uniform region used to normalize the arc profiles. .... 96

Figure 5-3: MTFs of experimental CS dataset compared to the equivalent Nyquist-sampled low-resolution (16×16) and the fully-sampled (32×32) Fourier reconstructions. MTFs of simulations are shown for comparison.. 99

Figure 5-4: Simulated acetate area reconstructions for (a) full Nyquist sampling (32×32), (b) CS equivalent low-resolution sampling (16×16), (c) 4× CS-MRSI using a step PDF, and (d) 4× CS-MRSI using a 1/r<sup>2</sup> PDF..... 100

Figure 5-5: MTFs of acetate area simulations of full Nyquist sampled (32×32) reconstructions, CS equivalent low-resolution (16×16) reconstructions, 4× CS-MRSI using a step PDF and a 1/r<sup>2</sup> PDF ..... 101

Figure 5-6: Comparison between the CS-MTF and the sampling-modulated NS-MTF of (a) step PDF, (b) 1/r<sup>2</sup> PDF, and (c) half-Gaussian PDF ..... 102

Figure 5-7: Comparison between the prescribed PDF and the average sampling ratio for k-space sampling patterns generated using the original algorithm. (a) Step PDF. (b) 1/r<sup>2</sup> PDF. (c) Half-Gaussian PDF..... 103

Figure 5-8: Comparison between the prescribed PDF and the average sampling ratio for k-space sampling patterns generated using the density-constrained algorithm. (a) Step PDF. (b) 1/r<sup>2</sup> PDF. (c) Half-Gaussian PDF.104

Figure 5-9: Side-by-side comparison of the CS-MTF, the sampling-modulated NS-MTF and the PDF-modulated NS-MTF resulting from the unconstrained (left) and constrained (right) algorithms for (a) step PDF, (b) 1/r<sup>2</sup> PDF and (c) half-Gaussian PDF..... 105

Figure 5-10: (a) Coefficients of determination between the PDF-modulated NS-MTF and the CS-MTF for step, 1/r<sup>2</sup>, and half-Gaussian PDFs. (b) Norm of residuals between the PDF-modulated NS-MTF and the CS-MTF for step, 1/r<sup>2</sup>, and half-Gaussian PDFs. .... 106

Figure 6-1: An illustration of 2-D complex conjugate symmetry in k-space ..... 112

Figure 6-2: (a) T2-weighted image of the phantom with the white box showing the MRSI field-of-view. (b) Fully sampled acetate area map. The high-lighted pie-shaped region the region of interest used for MTF calculation. The dashed arrow signifies the location of the arc profile shown in figure 2. The black box region is the uniform region used to normalize the arc profiles. .... 113

<b>Figure 6-3: (a) an example of k-space sampling pattern. (b) Conjugate-filled k-space. The lines show the 4 quadrants of k-space. ....</b>	<b>115</b>
<b>Figure 6-4: Acetate area maps for (a) Nyquist sampled (32×32), (b) 4-times CS time-equivalent NS (16×16), (c) 4-times, (d) 5-times, (e) 6-times conventional CS, (f) 4-times, (g) 5-times, and (h) 6-times CMaCS reconstructions. ....</b>	<b>117</b>
<b>Figure 6-5: MTFs of 4-, 5-, and 6-times accelerated reconstructions for simulated datasets using (a) conventional CS, and (b) CMaCS. ....</b>	<b>118</b>
<b>Figure 6-6: Comparison between CMaCS-MTF and 2× PDF-modulated NS-MTF (capped at 1) for (a) 4-times, (b) 5-times, and (c) 6-times acceleration. ....</b>	<b>119</b>
<b>Figure 6-7: MTFs of 4-, 5-, and 6-times accelerated reconstructions for experimentally acquired datasets using (a) conventional CS, and (b) CMaCS. ....</b>	<b>120</b>

# Chapter One

## 1 Introduction

---

### **1.1 Astrocytomas**

The World Health Organization (WHO) regularly publishes detailed tumor classification guidelines to aid in identifying and classifying different types of tumors. The WHO classification is based on the premise that each tumor type results from abnormal proliferation of a specific cell type and that the behavior of the tumor and its response to treatment is dictated by that cell type.<sup>1</sup> Hence, accurate classification of tumor cell type is important in determining treatment choices and predicting prognosis. Astrocytic tumors are a specific yet diverse class of those tumors that span a wide range of neoplasm with very distinct clinical, histological and genetic features. Astrocytic tumors arise from astrocytes, a type of glial cell that form most types of cells in the brain, and are classified into four grades: Pilocytic Astrocytoma (non-invasive) (grade I), Astrocytoma (grade II), Anaplastic (malignant) Astrocytoma (grade III) (also commonly referred to as Glioma), and Glioblastoma Multiforme (GBM) (grade IV).<sup>1, 2</sup> High grade gliomas are associated with very poor prognosis; ~60 weeks median survival is reported after a combination of surgery, radiotherapy and chemotherapy. Studies also report no significant changes in survival rate for GBMs between the early 1980's and the late 1990's even with changes in treatment protocols.<sup>3</sup> Further complicating matters is the fact that individual histologically defined types of astrocytomas are even more diverse at a biological level. There are noted clinical and genetic differences between primary gliomas (grades III and IV) and secondary gliomas resulting from progression from lower grades. While it is not clear whether those distinctions affect prognosis it remains that they would likely respond differently to different treatments.<sup>1, 2</sup>

## **1.2 The Radiotherapy Process**

When an individual is diagnosed with cancer there are usually three treatment options: surgery, radiotherapy, and chemotherapy. Surgical resection is the most desired option for most solid tumors. However, combined modality treatments are usually used to improve survival and tumor control. For instance, Glioblastoma Multiforme is usually treated with surgery followed by radiotherapy and chemotherapy, as studies have shown that this combination leads to a significant improvement in tumor control.<sup>4-7</sup>

The radiotherapy process consists of a series of stages that start with the patient being diagnosed with a tumor and ends with patient follow-up after treatment. The process can be represented by a chain that is as strong as its weakest link. The main links on the chain are tumor definition, treatment planning, and treatment delivery.<sup>8</sup> With advancements in treatment planning and delivery systems, tumor definition (delineation) has become the stage most in need of refinement. One of the characteristics of Glioblastomas is microscopic disease invasion outside of the gross tumor volume which is hard to detect using conventional imaging techniques. Left untreated or under-treated, microscopic disease accounts for a large portion of GBM recurrences.<sup>9-12</sup> Conversely, biological imaging modalities such as Magnetic Resonance Spectroscopic Imaging (MRSI) and Positron Emission Tomography (PET) have been able to detect microscopic disease and predict progression outside the visible tumor volume.<sup>13-17</sup> Incorporating those biological modalities in the radiotherapy process can lead to improved biological delineation of the tumors which may in turn lead to the reduction of microscopic disease related recurrences and improved tumor control.<sup>18-20</sup>

This thesis will discuss the improvements that can be introduced to biologically based tumor delineation using MRSI. This chapter discusses the role of imaging in the radiotherapy process, specifically, the role MRI and MRSI play in tumor delineation. It also briefly discusses some of the

basics of contouring and the advancements in treatment delivery that have led to the increasing importance of biological imaging of solid tumors.

### **1.3 Imaging and the Radiotherapy Process**

Imaging is essential to the radiotherapy processes especially in the case of solid tumors as it is involved in a number of its stages. Firstly, imaging plays a primary role in the diagnosis and the prognosis of cancer. Secondly, when radiotherapy is the treatment of choice, 3-D imaging becomes important for tumor delineation, organ localization and dose calculations. Finally, imaging on the treatment unit, in the form of mega-voltage x-rays (portal imaging), mega-voltage computed tomography (MVCT), on-board kilo-voltage CT, and more recently conjoined or integrated MRI systems, is used for position verification and in some cases tumor tracking or dose reconstruction. This section briefly describes the uses of different imaging modalities in the diagnosis and treatment planning of cancer.

#### **1.3.1 Diagnostic and 3-D Imaging**

Imaging modalities can be divided into two main categories; anatomic and functional modalities. Anatomic modalities such as X-Ray, Computed Tomography (CT), Magnetic Resonance Imaging (MRI) and Ultra-Sound (US) provide images of anatomic structures. They rely on different mechanisms for imaging the anatomic structures and can sometimes indicate the functionality of an organ. However, anatomic modalities are generally unable to detect metabolic or biochemical changes within tissue.

On the other hand, functional and metabolic modalities such as Positron Emission Tomography (PET), Single Photon Emission Computed Tomography (SPECT), functional MRI (fMRI) and MR Spectroscopic Imaging (MRSI) provide images of the metabolism or functionality of different organs. Those modalities depend on either radiopharmaceutical

uptake in the case of PET and SPECT, changes in blood oxygenation levels for fMRI or on biochemical compositions within the imaged body as in MRSI.

CT is of specific importance to the radiotherapy process. Besides being a good diagnostic imaging modality of generally high-spatial resolution with short scan times, CT is an x-ray based modality and hence its images provide the electron density information necessary for dose calculations and treatment planning. Accordingly, a planning CT is used as the basis for most radiotherapy treatment planning. The contrast mechanism of CT relies on differences in x-ray attenuation coefficients between the imaged tissue types. This allows CT to provide excellent contrast between soft tissue, bony structures and air. However, contrast within the soft tissue (soft tissue contrast) is poor in CT due to the similarity of the attenuation coefficients within soft tissue. Thus, relying on CT alone for tumor delineation and organ localization in soft tissue may lead to poor organ definitions due to the reduced contrast. As a result soft tissue contrast is sometimes enhanced by using different x-ray energies or by using a contrast agent. The contrast agent is a high electron density material that is usually injected or swallowed by the patient and is imaged directly by CT.

### **1.3.2 MRI and Tumor Delineation**

Because MRI most commonly relies on hydrogen protons for signal, it may appear that the only source of contrast in MRI is proton density. In that case it is not much different from CT which relies on electron density for contrast. However, MRI can detect subtle changes in tissue caused by changes in tissue specific molecular environment or the surrounding chemistry. Such changes can manifest themselves as changes in the available detectable MRI signal and more is accurately referred to as relaxation. That difference in relaxation is the most used contrast mechanism in MRI.

Differences in relaxation arise from the differences in chemical composition between tissue types. (See *Chapter II* for the explanation of relaxation mechanisms in MRI.) These changes in relaxation can be detected in MRI and used for contrast. By optimizing the scan parameters, the relative signal received from different tissues can be changed without the need of any exogenous contrast agents. In the case of the brain, white matter would appear brighter than grey matter on scans optimized to exploit longitudinal relaxation (T1 weighted), while on T2 weighted scans (optimized for contrast in transverse relaxation) white matter would appear darker than grey matter. Sources of contrast in MRI are not limited to relaxation; other sources of contrast include diffusion, perfusion, and magnetization transfer which is used for non-invasive angiography.

In GBM studies, MRI scans are routinely used for treatment planning.<sup>18, 19</sup> Due to the breakage of the blood brain barrier at the tumor site, a contrast agent in the blood stream enhances the appearance of the tumor while the surrounding edema and necrosis are left un-enhanced, providing very high contrast in T1 weighted scans. These scans are the most commonly used scans for GBM delineation. In addition, T2 weighted scans show the extent of the tumor and the surrounding edema. Also, MRI diffusion and perfusion studies can be performed to define and evaluate tumor malignancy and stage.<sup>21</sup>

The same scanners used for MRI are able to perform biochemical imaging in the form of MR Spectroscopy (MRS). MRS relies on the chemical shift phenomenon to distinguish between different chemical compounds in the same way an *in-vitro* NMR experiment would. Combined with spatial encoding, MRS can be transformed into MRSI where an image can be produced describing the biochemical composition of the imaged subject.

### **1.3.3 MRI vs. CT**

In radiotherapy treatment planning, the electron density of tissue is important in order to perform correct dose calculations. While many methods have been proposed to perform MRI based treatment planning, CT remains the most widely used and dependable source of electron density information. It is in the versatility of MRI that its strength lies. A single MR study can be used to produce anatomic images with multiple contrast, along with biochemical information that can potentially be used for biological assessment.<sup>21</sup>

Combining the excellent soft tissue contrast of MRI for better tumor (target) delineation with the electron density information provided by CT for dose calculations can lead to more conformal plans compared to using CT alone. Furthermore, the use of MRSI adds the dimension of biological targeting to the otherwise purely anatomically based tumor delineation. Image registration techniques such as slice alignment using fiducial makers, or mutual information are used to fuse CT images with their corresponding MRI and MRSI counterparts. The resulting fused images are used in the treatment planning system for tumor delineation, organ localization and dose calculations.<sup>20</sup>

## **1.4 Treatment Planning**

The goal of radiotherapy is to deliver a prescribed dose of radiation to the tumor while minimizing the dose delivered to the surrounding normal tissue. To achieve this goal a treatment plan is developed in which the target tumor volume as well as the organs at risk are contoured. Those volumes are contoured using the images acquired in the previous 3-D imaging stage. Accordingly, the quality of those images, whether anatomic or biochemical, affects the target contours and in turn the outcome of the treatment.

Generally, three contours are used to define the target for radiation; the gross tumor volume (GTV), the clinical target volume (CTV), and the

planning target volume (PTV). The GTV is usually contoured by the clinician and is defined by the boundaries of the visible tumor on the anatomic scan. In GBM the GTV is defined on the T1 contrast enhanced images by the boundaries of contrast enhancement (edge enhancement). The CTV includes the GTV and extends beyond it to include possible regions of microscopic disease. The margin between GTV and CTV varies according to the tumor site and stage. For GBM the margin between GTV and CTV is typically 2 cm as it is here that most recurrences exist.<sup>10, 11, 22</sup> PTV is then defined to include both GTV and CTV and is the main target for treatment planning. The PTV is larger than CTV and accounts for setup errors and patient movement. The margin of the PTV usually doesn't exceed 5 mm from the CTV depending on the tumor site, immobilization devices, reproducibility of patient setup and organ movements.<sup>10, 11</sup> The PTV is the volume to which the prescribed dose is to be delivered.

One may add two more volumes; the irradiated volume (IV) and the biological target volume (BTV).<sup>8, 17</sup> Although not used in the initial planning, the IV represents the actual irradiated volume for a beam selection. The IV is always larger than the desired PTV due to build up and exit doses. In the beam selection and optimization stage which follows target definition, the treatment planning goal is to reduce the dose to normal tissue, commonly referred to as organs at risk (OAR), within the IV in order to reduce complications.

Unlike the previously mentioned GTV, the BTV is defined using biochemical or functional modalities.<sup>17</sup> It outlines regions of tumor activity and is interpreted differently depending on the tumor type and stage.<sup>17</sup> In some cases the BTV can be used to define dose boost volumes or nonuniform margins for tumor extent and microscopic disease.<sup>14</sup>

Following target definition, the treatment protocol and beam arrangements are selected. Dose calculations are performed and the treatment plan is optimized for the goals of the treatment.

## **1.5 Treatment Delivery**

Delivering radiation therapy can be done using two commonly used techniques: external beam radiotherapy using x-ray or gamma ray emitting units, or brachytherapy using sources placed inside or in close proximity to tumors. Only advancements in external beam radiotherapy will be discussed in this section.

External beam radiation devices range from kilo-voltage (kV) x-ray units that are used for superficial treatments through cobalt units and linear accelerators (linacs). With the exception of Cobalt units, all external beam radiotherapy units rely on producing x-rays through bremsstrahlung. Electrons are accelerated and focused onto a lead/tungsten target which causes them to decelerate rapidly and thereby produce x-rays, hence the name bremsstrahlung (braking radiation). In kV units the electrons are accelerated using conventional x-ray tubes. However, in a linac, due to the high electron energies needed (6MeV and greater), the electron acceleration process is achieved using high frequency wave guides that differ in design according to the manufacturers.

Some of the most notable advancements in treatment delivery are beam shaping devices. The introduction of multi-leaf collimators has led to the development of Intensity Modulated Radiotherapy (IMRT). The ability to modulate the dose within the PTV provides the opportunity of dose boosting to the BTV.

Portal imaging devices and on-board imagers outfitted to linacs as well as mega-voltage CT are readily used for setup verification purposes. However, there is great potential for utilizing those devices for Image Guided Adaptive Radiotherapy in which the treatment plan is adjusted on a dose-to-dose basis to compensate for organ movements and previous setup errors. Moreover, there has been an avalanche of interest in recent years to integrate MRI systems with linacs with the ultimate goal of real-time tumor tracking.

All the above mentioned advancements in treatment delivery have had a great influence on either improving the outcome or reducing the toxicity of radiotherapy.<sup>23-26</sup> Novel planning techniques and algorithms combined with IMRT and Helical Tomotherapy have all provided the means of producing and, in most cases, delivering a treatment plan that is highly conformal to the PTV. This leads to treatments that can be tailored to boost dose to the predefined margins within the tumor while sparing radiosensitive organs, hence, improving tumor control probability and minimizing normal tissue complications.

With the advancements of delivery techniques it has become clear that tumor definition is currently one of the most important links in the radiotherapy process. The GTV for most tumors is usually visible using conventional anatomic imaging modalities. It is the microscopic extent and the biological activity of the tumors that these modalities fail to detect (e.g. in GBM most recurrences arise within 2 cm from the visible GTV). Using a biochemical imaging modality to probe metabolite concentrations that can be linked to tumor growth and characterization, a BTV may be added to the delineation stage.

MRSI is a multi-voxel non-invasive biochemical imaging modality that can be used for this purpose. It has been shown that MRSI can be used to probe different metabolite concentrations in the brain and the prostate. Those studies have been correlated with physical biopsies taken from tumor sites.<sup>12, 14, 18, 20, 21</sup> However, wide clinical implementation of MRSI in the radiotherapy process has been lagging due to two main practical shortcomings: Firstly, interpretation of MRSI data has been largely inconsistent for clinical implementation. It is largely based on qualitative assessment of the metabolite peaks by radiologists or oncologist based on spectra whose quality is heavily dependent on the institutional scanning and processing protocols used. Accordingly, efforts to biologically delineate tumors from MRSI have been largely subjective and irreproducible. This has been the main limiting factor in performing

serial or population based studies. Also, MRSI scans are highly dependent on the scanner and scanning sequence used, adding to the complexity of performing inter-institution studies. Moreover, correlation with histology has relied on stereotactic biopsies which, while being a largely accurate method, provide only a point based correlation with MRSI. Two-dimensional correlation, especially at the tumor/normal tissue boundaries is very poorly reported.

Secondly, most commonly used MRSI sequences suffer from long scan times ( $\sim 15$  minutes) and poor spatial resolution ( $\sim 1 \text{ cm}^3$ ). With advancements in treatment delivery, there has arisen a need to improve the spatial resolution of MRSI scans to be considered clinically viable. However, increasing the resolution ( $\sim 0.5 \text{ cm}^3$ ) usually corresponds to increasing the scan time ( $\sim 30$  minutes), rendering MRSI increasingly harder to incorporate in everyday clinical MRI studies.

The purpose of this thesis is to tackle the two main practical hurdles to implementing MRSI in the radiotherapy process outlined above. Chapter Two introduces the reader to the theory of MRI, contrast mechanisms, signal and noise considerations, as well as a detailed introduction to MRSI, its theory, and acquisition techniques. Chapter Three discusses our proposal for a modification to an automatic delineation technique of GBM in an effort to improve the objectivity and reproducibility of biological target delineation for radiotherapy planning. Chapter Four discusses accelerating MRSI acquisitions using compressed sensing - currently a popular technique in MRI circles - in which we investigate the possible costs and benefits of such technique on the image quality of MRSI scans. Chapter Five investigates the correlation between the manner in which compressed sensing is implemented and its effects on image quality. Chapter Six discusses recent results in our effort to exploit inherent properties of spatial frequency space (k-space) to reduce the cost of compressed sensing on image quality. This chapter consists mainly of simulations and outlines future work that may need to be conducted on the

subject. Finally, Chapter Seven summarizes the conclusions reached in this work and outlines areas of future development and research towards wider clinical application of MRSI in biological tumor delineation.

## References:

1. P. Kleihues, D. N. Louis, B. W. Scheithauer, L. B. Rorke, G. Reifenberger, P. C. Burger and W. K. Cavenee, "The WHO classification of tumors of the nervous system," *Journal of neuropathology and experimental neurology* **61** (3), 215-225; discussion 226-219 (2002).
2. D. N. Louis, H. Ohgaki, O. D. Wiestler, W. K. Cavenee, P. C. Burger, A. Jouvret, B. W. Scheithauer and P. Kleihues, "The 2007 WHO classification of tumours of the central nervous system," *Acta neuropathologica* **114** (2), 97-109 (2007).
3. N. Laperriere, L. Zuraw and G. Cairncross, "Radiotherapy for newly diagnosed malignant glioma in adults: a systematic review," *Radiotherapy and oncology : journal of the European Society for Therapeutic Radiology and Oncology* **64** (3), 259-273 (2002).
4. H. A. Fine, K. B. Dear, J. S. Loeffler, P. M. Black and G. P. Canellos, "Meta-analysis of radiation therapy with and without adjuvant chemotherapy for malignant gliomas in adults," *Cancer* **71** (8), 2585-2597 (1993).
5. K. Kristiansen, S. Hagen, T. Kollevold, A. Torvik, I. Holme, R. Nesbakken, R. Hatlevoll, M. Lindgren, A. Brun, S. Lindgren, G. Notter, A. P. Andersen and K. Elgen, "Combined modality therapy of operated astrocytomas grade III and IV. Confirmation of the value of postoperative irradiation and lack of potentiation of bleomycin on survival time: a prospective multicenter trial of the Scandinavian Glioblastoma Study Group," *Cancer* **47** (4), 649-653 (1981).
6. U. Lassen, P. E. Kristjansen, A. Wagner, M. Kosteljanetz and H. S. Poulsen, "Treatment of newly diagnosed glioblastoma multiforme with carmustine, cisplatin and etoposide followed by radiotherapy. A phase II study," *J. Neurooncol.* **42** (2), 161-166 (1999).
7. A. Brandes, M. Soesan and M. V. Fiorentino, "Medical treatment of high grade malignant gliomas in adults: an overview," *Anticancer research* **11** (2), 719-727 (1991).
8. J. Van Dyk, *The Modern Technology of Radiation Oncology*. (Medical Physics Publishing, 1999).
9. E. Alexander, 3rd and J. S. Loeffler, "Radiosurgery for primary malignant brain tumors," *Seminars in surgical oncology* **14** (1), 43-52 (1998).
10. C. F. Hess, J. C. Schaaf, R. D. Kortmann, M. Schabet and M. Bamberg, "Malignant glioma: patterns of failure following individually tailored limited volume irradiation," *Radiother. Oncol.* **30** (2), 146-149 (1994).
11. S. W. Lee, B. A. Fraass, L. H. Marsh, K. Herbort, S. S. Gebarski, M. K. Martel, E. H. Radany, A. S. Lichter and H. M. Sandler, "Patterns of failure following high-dose 3-D conformal radiotherapy for high-grade astrocytomas: a quantitative dosimetric study," *Int. J. Radiat. Oncol. Biol. Phys.* **43** (1), 79-88 (1999).
12. K. E. Wallner, J. H. Galicich, G. Krol, E. Arbit and M. G. Malkin, "Patterns of failure following treatment for glioblastoma multiforme and

- anaplastic astrocytoma," *Int. J. Radiat. Oncol. Biol. Phys.* **16** (6), 1405-1409 (1989).
13. S. A. Kwee, M. N. Coel, J. Lim and J. P. Ko, "Combined use of F-18 fluorocholine positron emission tomography and magnetic resonance spectroscopy for brain tumor evaluation.," *J. Neuroimaging* **14** (3), 285-289 (2004).
  14. A. Pirzkall, X. Li, J. Oh, S. Chang, M. S. Berger, D. A. Larson, L. J. Verhey, W. P. Dillon and S. J. Nelson, "3D MRSI for resected high-grade gliomas before RT: tumor extent according to metabolic activity in relation to MRI," *Int. J. Radiat. Oncol. Biol. Phys.* **59** (1), 126-137 (2004).
  15. J. Walecki, E. Tarasow, B. Kubas, Z. Czernicki, J. Lewko, J. Podgorski, M. Sokol and P. Grieb, "Hydrogen-1 MR spectroscopy of the peritumoral zone in patients with cerebral glioma: assessment of the value of the method," *Acad. Radiol.* **10** (2), 145-153 (2003).
  16. J. Pallud, B. Devaux, F. Nataf, F. X. Roux and C. Dumas-Duport, "Spatial delimitation of low grade oligodendrogliomas," *Neurochirurgie.* **51** (3-4), 253-259 (2005).
  17. C. C. Ling, J. Humm, S. Larson, H. Amols, Z. Fuks, S. Leibel and J. A. Koutcher, "Towards multidimensional radiotherapy (MD-CRT): biological imaging and biological conformality," *Int. J. Radiat. Oncol. Biol. Phys.* **47** (3), 551-560 (2000).
  18. S. J. Nelson, E. Graves, A. Pirzkall, X. Li, A. A. Chan, D. B. Vigneron and T. R. McKnight, "In Vivo molecular imaging for planning radiation therapy of gliomas: an application of 1H MRSI," *J. Magn. Reson. Imaging* **16** (4), 464-476 (2002).
  19. T. R. McKnight, S. M. Noworolski, D. B. Vigneron and S. J. Nelson, "An automated technique for the quantitative assessment of 3D-MRSI data from patients with glioma," *Journal of magnetic resonance imaging : JMRI* **13** (2), 167-177 (2001).
  20. J. Chang, S. Thakur, G. Perera, A. Kowalski, W. Huang, S. Karimi, M. Hunt, J. Koutcher, Z. Fuks, H. Amols and A. Narayana, "Image-fusion of MR spectroscopic images for treatment planning of gliomas," *Med. Phys.* **33** (1), 32-40 (2006).
  21. A. Di Costanzo, T. Scarabino, F. Trojsi, G. M. Giannatempo, T. Popolizio, D. Catapano, S. Bonavita, N. Maggialelli, M. Tosetti, U. Salvolini, V. A. d'Angelo and G. Tedeschi, "Multiparametric 3T MR approach to the assessment of cerebral gliomas: tumor extent and malignancy," *Neuroradiology* **48** (9), 622-631 (2006).
  22. G. Kantor, H. Loiseau, A. Vital and J. J. Mazon, "Gross tumor volume (GTV) and clinical target volume (CTV) in adult gliomas," *Cancer Radiother.* **5** (5), 571-580 (2001).
  23. M. J. Zelefsk, H. Chan, M. Hunt, Y. Yamada, A. M. Sippy and H. Amols, "Long-term outcome of high dose intensity modulated radiation therapy for patients with clinically localized prostate cancer," *J. Urol.* **176** (4), 1415-1419 (2006).

24. C. D. Fuller, C. R. J. Thomas, A. Wong, S. X. Cavanaugh, B. J. Salter, T. S. Herman and M. Fuss, "Image-guided intensity-modulated radiation therapy for gallbladder carcinoma," *Radiother. Oncol.* **81** (1), 65-72 (2006).
25. S. E. Combs, S. Konkell, D. Schulz-Ertner, M. W. Munter, J. Debus, P. E. Huber and C. Thilmann, "Intensity modulated radiotherapy (IMRT) in patients with carcinomas of the paranasal sinuses: clinical benefit for complex shaped target volumes," *Radiat. Oncol.* **1**, 23 (2006).
26. D. Rades, F. Fehlauer, J. Wroblewski, D. Albers, S. E. Schild and R. Schmidt, "Prognostic factors in head-and-neck cancer patients treated with surgery followed by intensity-modulated radiotherapy (IMRT), 3D-conformal radiotherapy, or conventional radiotherapy," *Oral Oncol.* **doi:10.1016/j.oraloncology.2006.05.006.** (2006).

## Chapter Two

### 2 Theory of Magnetic Resonance Imaging

---

#### 2.1 Introduction

In Chapter One we have introduced the role that MRI plays in the radiotherapy process and how biological imaging has the potential to improve outcomes in radiotherapy. This Chapter explains in detail the basic physics of nuclear magnetic resonance (NMR), MRI and MRSI.

The physics of NMR can be described using both classical and quantum mechanics. While the classical description is simpler to understand, a brief quantum mechanical description of NMR will be introduced to describe the basic theory of the behavior of spins in the presence of a static uniform magnetic field. Since the classical description will be used for the chapter as a whole, the quantum mechanical description of the preparation stage will be discussed first so as not to disrupt the continuity of the chapter. The process of producing and acquiring an NMR signal can best be described by breaking it into three basic stages; the preparation stage, the excitation stage, and the acquisition stage.

#### 2.2 Quantum Mechanical Description of NMR

##### 2.2.1 Spin $\frac{1}{2}$ in a static magnetic field (preparation)

Consider a system consisting primarily of protons with spin  $\frac{1}{2}$  as our sample for the NMR experiment. Spin angular momentum of nuclei is a vector quantity defined as:

$$\mathbf{S} = \frac{h}{2\pi} \mathbf{I} \quad (2-1)$$

where  $h$  is Planck's constant and  $\mathbf{I}$  is the quantum mechanical spin operator. The magnetic dipole moment associated with  $\mathbf{S}$  is:

$$\boldsymbol{\mu} = \gamma \mathbf{S} = \gamma \frac{h}{2\pi} \mathbf{I} \quad (2-2)$$

where  $\gamma$  is the gyromagnetic ratio of the nuclei. For hydrogen protons,  $\gamma = 267.513 \times 10^6$  radians/(second · Tesla).

The interaction energy of a magnetic dipole moment with a static magnetic field  $\mathbf{B}_0$  is defined by:

$$E = -\boldsymbol{\mu} \cdot \mathbf{B}_0 \quad (2-3)$$

In a static uniform field oriented along the z-direction, Eq. 2-3 becomes:

$$E = -\frac{\gamma}{2\pi} h \mathbf{I}_z \cdot \mathbf{B}_0 \quad (2-4)$$

The Zeeman Hamiltonian ( $H_{B_0}$ ) can hence be used to describe the interaction of the spins with the static magnetic field as:

$$H_{B_0} = -\frac{\gamma}{2\pi} h B_0 \mathbf{I}_z \quad (2-5)$$

For hydrogen nuclei (protons),  $\mathbf{I}_z$ , the quantum mechanical spin operator, has two eigenstates,  $+1/2$  and  $-1/2$ . Applying the Zeeman Hamiltonian to the energy eigenstates in the spin wave function, we get the energy eigenvalues corresponding to those eigenstates:

$$H_{B_0}(|\alpha\rangle + |\beta\rangle) = E(|\alpha\rangle + |\beta\rangle) = -\frac{\gamma}{2\pi} h B_0 / 2 |\alpha\rangle - \frac{\gamma}{2\pi} h B_0 / 2 |\beta\rangle \quad (2-6)$$

where  $|\alpha\rangle$  and  $|\beta\rangle$  are spin states oriented parallel and anti-parallel to  $\mathbf{B}_0$ , respectively.

Accordingly, when a spin  $\frac{1}{2}$  system is placed in a uniform static magnetic field there are only two possible energy states in which the spin can be described. The whole system can either be a mixture of those states or purely one or the other.<sup>1</sup> From Eq. 2-6 the Zeeman energy separation between the eigenstates can also be written as:

$$\Delta E = \frac{\gamma}{2\pi} h B_0 \quad (2-7)$$

$$\Delta E = h f_0$$

where  $f_0$  is referred to as the Larmor frequency and  $\omega_0$  as the angular Larmor frequency such that:

$$f_0 = \frac{\gamma}{2\pi} B_0 \quad (2-8)$$

$$\omega_0 = \gamma B_0$$

At 3T,  $f_0 = 127.728$  MHz, and  $\omega_0 = 802.539 \times 10^6$  radian/second, respectively.

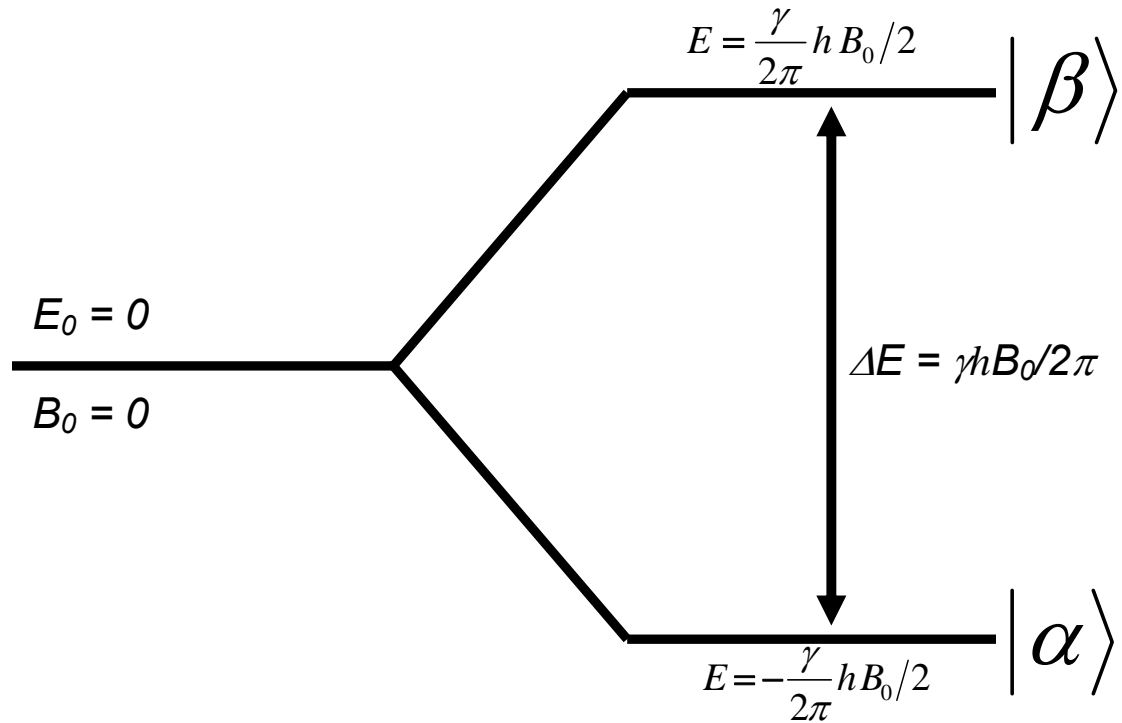


Figure 2-1: The energy level diagram of a spin  $\frac{1}{2}$  system observed in  $B_0 = 0$  and  $B_0 \neq 0$

In thermal equilibrium, the relative populations of the spins in the eigenstates is defined by the Boltzman distribution <sup>2</sup>:

$$N_{|\beta\rangle} / N_{|\alpha\rangle} = e^{-\Delta E/kT} \quad (2-9)$$

where  $N$  is the spin population of a particular state,  $k$  is Boltzman constant ( $1.38 \times 10^{-23}$  J/K) and  $T$  is the temperature in Kelvin.

Accordingly, in the absence of the magnetic field, where  $\Delta E = 0$ , the spins have equal probability to be oriented in any direction resulting in a net magnetization of zero. However, in the presence of a static magnetic field, where  $\Delta E \neq 0$ , the spins will orient themselves either parallel or anti-parallel to the field but due to the population statistics described in Eq. 2-9, there is a net longitudinal magnetization parallel to  $\mathbf{B}_0$ .

### **2.3 The classical description of NMR**

Consider a volume containing an arbitrary sample of protons each with magnetic moment  $\mu$ . The net magnetization within the sample volume is equal to the sum of the magnetic moment vectors of the protons in the sample:

$$\mathbf{M}_0 = \sum_{\text{volume}} \mu_i \quad (2-10)$$

In the absence of a magnetic field the magnetic moment vectors are oriented randomly as shown in Fig. 2-2a. Accordingly, the magnetic moments cancel each other in vector sum and the net magnetization of the sample is zero.<sup>2</sup>

#### **2.3.1 Magnetic moments in a static magnetic field $\mathbf{B}_0$ (preparation)**

In thermal equilibrium in the presence of a static magnetic field  $\mathbf{B}_0$  the magnetic moments of the protons present in our sample would align in a direction either parallel or anti-parallel to the magnetic field. As

discussed earlier, the population of spins in the parallel orientation will be greater than that in the anti-parallel orientation resulting in a net magnetization along the direction of the applied static magnetic field.

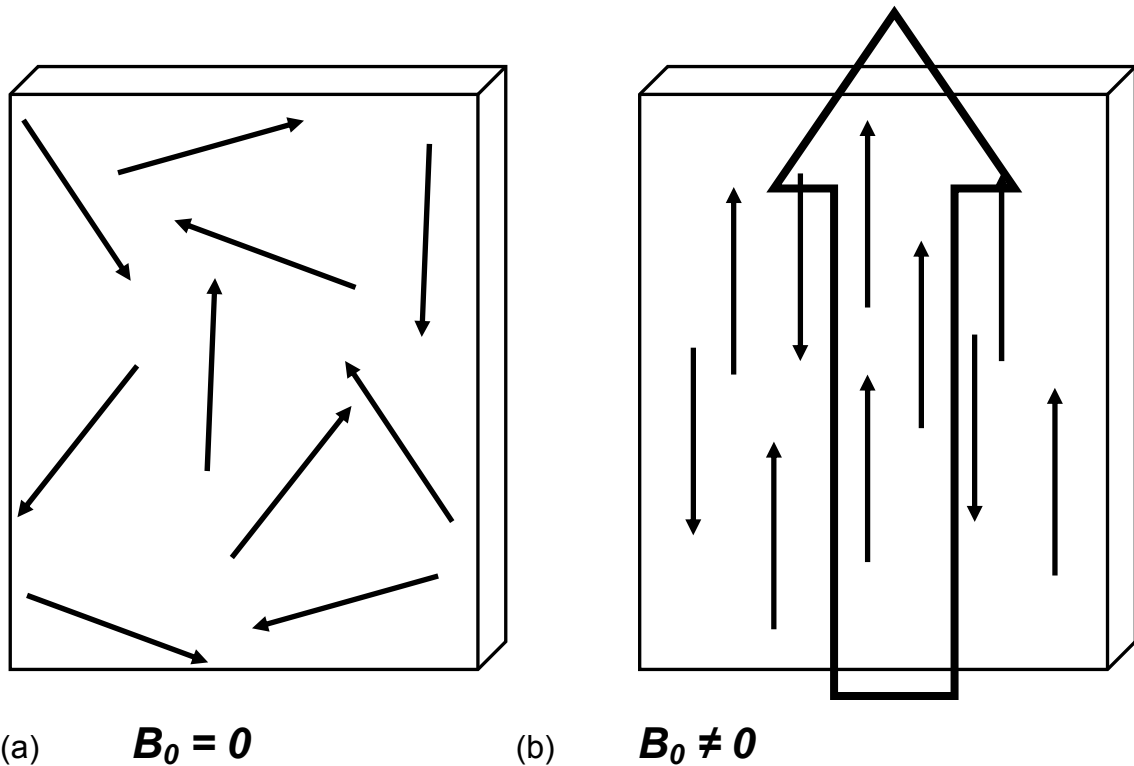


**Figure 2-2: Magnetic moment vectors within a sample shown in: (a) The absence of a uniform external magnetic field resulting in random orientations zero net magnetization. (b) The magnetic moments are arranged in the parallel and anti-parallel orientation with respect to the applied magnetic field. The net magnetization vector  $M_0$  resulting is shown as the big arrow.**

### 2.3.2 The excitation process

The aim of the excitation process is to disrupt the thermal equilibrium state of the magnetization vector  $M_0$ , and produce a component of the magnetization vector in the xy-plane which can be detected using an antenna. The excitation process is achieved by applying a circularly polarized (rotating) magnetic field  $B_1$  with angular frequency  $\omega$  clockwise in the xy-plane.  $B_1$  is applied by a radio-frequency (RF) pulse

in the presence of and orthogonal to the static magnetic field  $\mathbf{B}_0$ . The total magnetic field  $\mathbf{B}$  experienced by the spins then becomes:

$$\mathbf{B} = \mathbf{B}_0 + \mathbf{B}_1(t) \quad (2-11)$$

where  $\mathbf{B}_0 = (0,0,B_0)$  and  $\mathbf{B}_1 = (B_1 \cos \omega t, -B_1 \sin \omega t, 0)$  resulting in:

$$\mathbf{B} = (B_1 \cos \omega t, -B_1 \sin \omega t, B_0) \quad (2-12)$$

where the z-axis is defined along the axis of  $\mathbf{B}_0$  and the xy-plane is referred to as the transverse plane.

The time varying orthogonal magnetic field causes the magnetic dipole moment to experience torque causing a time varying change in angular momentum. Equating the rate of change of angular momentum to the torque experienced by the dipole moment:

$$\frac{h}{2\pi} \frac{d\mathbf{I}}{dt} = \boldsymbol{\mu} \times \mathbf{B} \quad (2-13)$$

Multiplying both sides by  $\gamma$  and from Eq. 2-2, we obtain:

$$d\boldsymbol{\mu} / dt = \gamma \boldsymbol{\mu} \times \mathbf{B} \quad (2-14)$$

Considering Eq. 2-10, the equation of motion now becomes:

$$\frac{d}{dt} (\sum \boldsymbol{\mu}) = d\mathbf{M} / dt = \gamma \sum \boldsymbol{\mu} \times \mathbf{B} \quad (2-15)$$

or

$$d\mathbf{M} / dt = \gamma \begin{vmatrix} \hat{i} & \hat{j} & \hat{k} \\ M_x & M_y & M_z \\ B_1 \cos \omega t & -B_1 \sin \omega t & B_0 \end{vmatrix} \quad (2-16)$$

which can be written as:

$$\begin{aligned} dM_x / dt &= \gamma(M_y B_0 + M_z B_1 \sin \omega t) \\ dM_y / dt &= \gamma(M_z B_1 \cos \omega t - M_x B_0) \\ dM_z / dt &= \gamma(-M_x B_1 \sin \omega t - M_y B_1 \cos \omega t) \end{aligned} \quad (2-17)$$

Equation 2-17 shows that the motion of the magnetization vector under both  $\mathbf{B}_1$  and  $\mathbf{B}_0$  becomes fairly complex since it involves rotation around the z-axis superimposed with rotation about the transverse axes. In order to better visualize the motion of  $\mathbf{M}$  and to simplify the mathematics we will consider a reference frame other than the Cartesian laboratory frame. The new reference frame is a rotating reference frame rotating with angular frequency  $\omega$  equal to that of the circularly polarized  $\mathbf{B}_1$ .<sup>1, 3</sup> In the rotating frame now both  $\mathbf{B}_1$  and  $\mathbf{B}_0$  appear to be static in the xy-plane and z-axis, respectively.

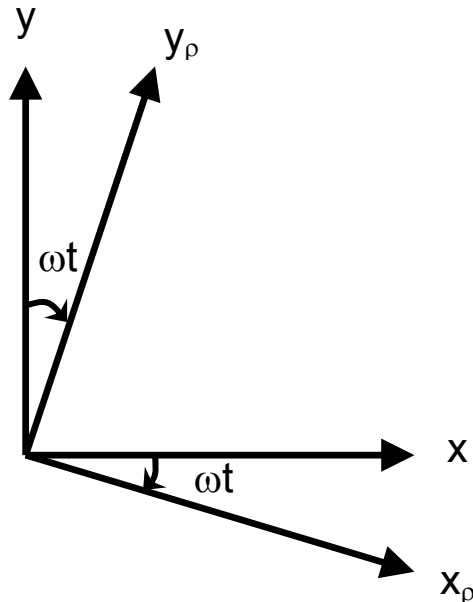


**Figure 2-3: The rotating frame of reference ( $x_p, y_p$ ) with respect to the laboratory frame ( $x, y$ ). The rotating frame rotates about the z-axis therefore,  $z_p$  is equivalent to  $z$ .**

From Figure 2-5, the components of the magnetization vector  $\mathbf{M}_p$  in the rotating frame are related to the magnetization vector  $\mathbf{M}$  in the laboratory frame through:

$$\begin{aligned}
M_{x\rho} &= M_x \cos \omega t - M_y \sin \omega t \\
M_{y\rho} &= M_x \sin \omega t + M_y \cos \omega t \\
M_{z\rho} &= M_z
\end{aligned}
\tag{2-18}$$

The derivation of these equations and substitution with the derivatives in the laboratory frame from Eq. 2-17 now yield the equations of motion in the rotating frame:

$$\begin{aligned}
dM_{x\rho} / dt &= (\gamma B_0 - \omega) M_{y\rho} \\
dM_{y\rho} / dt &= -(\gamma B_0 - \omega) M_{x\rho} + \gamma B_1 M_{z\rho} \\
dM_{z\rho} / dt &= -\gamma B_1 M_{y\rho}
\end{aligned}
\tag{2-19}$$

These equations can now be combined in one simple equation of motion:

$$d\mathbf{M}_\rho / dt = \gamma \mathbf{M}_\rho \times \mathbf{B}_{\text{eff}} \tag{2-20}$$

where,

$$\mathbf{B}_{\text{eff}} = B_1 \hat{i}_\rho + (B_0 - \omega / \gamma) \hat{k}_\rho \tag{2-21}$$

where,  $\hat{i}_\rho$  and  $\hat{k}_\rho$  are unit vectors in the  $x_\rho$  and  $z_\rho$  directions, respectively.

The resulting equation of motion in the rotating frame is of the same form as the one in the laboratory frame Eq. 2-15. The major difference is the presence of the effective time-dependent magnetic field  $\mathbf{B}_{\text{eff}}$  instead of  $\mathbf{B}$ .  $\mathbf{B}_{\text{eff}}$  also has components in the  $x_\rho$  and  $z_\rho$  directions implying that the magnetization vector will precess in a cone about the  $\mathbf{B}_{\text{eff}}$  axis with frequency  $\omega_{\text{eff}} = \gamma B_{\text{eff}}$  in the laboratory frame.

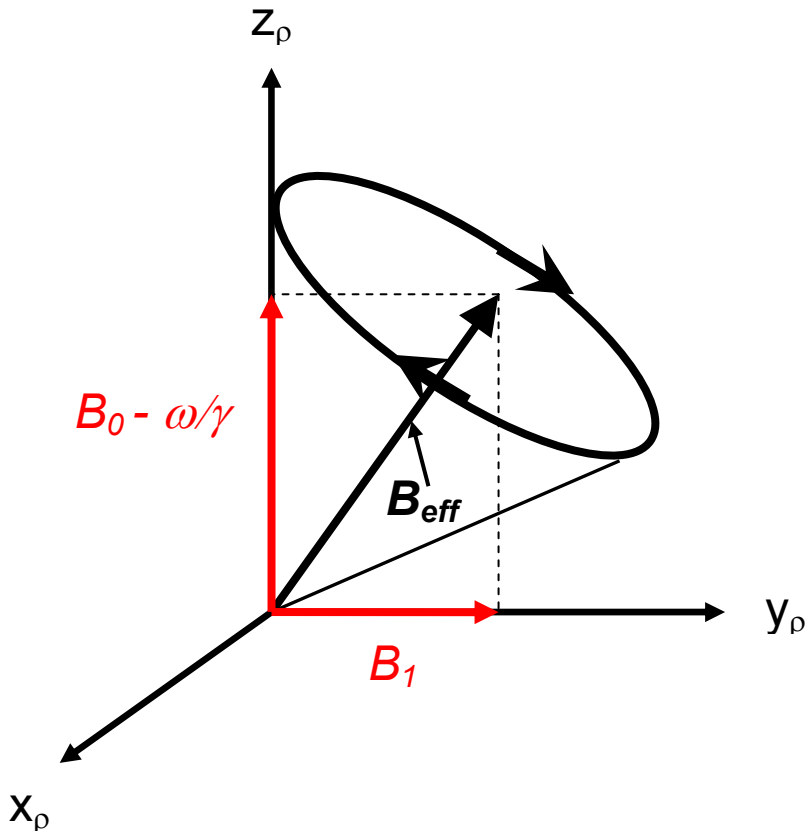


Figure 2-4: The magnetization vector precession about  $B_{eff}$  in the rotating reference frame.

If the angular frequency of the circularly polarized  $B_1$  field is  $\omega = \gamma B_0$ ,  $B_0$  is eliminated from Eq. 2-20 and  $B_{eff}$  becomes  $B_1$ . This is referred to as the resonance condition. Accordingly, if  $B_1$  is applied parallel to the  $y_\rho$ -axis the magnetization vector will precess in a circular motion in the  $z_\rho$ -plane. The circularly polarized magnetic field  $B_1$ , is produced by an RF pulse, and is usually referred to as an excitation pulse. The excitation pulse causes the magnetization vector to tip from the equilibrium position along the z-axis to the transverse plane resulting in a signal that can be detected using an antenna which is explained in the following section.<sup>4</sup>

The angle between the magnetization vector and the z-axis resulting from an excitation pulse is known as the flip angle which is defined as:

$$\alpha(t) = \gamma \int B_1(t) dt \quad (2-22)$$

Accordingly, if  $\mathbf{B}_1$  is applied for time  $t = \pi/2\gamma B_1$  the resulting flip angle would be  $\pi/2$  which is known as a  $90^\circ$  flip angle (pulse). Similarly,  $t = \pi/\gamma B_1$  results in an  $180^\circ$  flip angle (pulse).

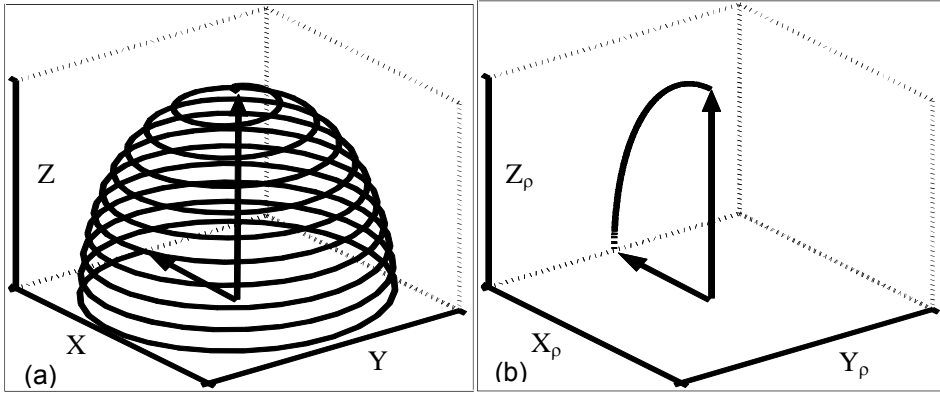


Figure 2-5: The motion of the magnetization vector during a  $90^\circ$  excitation pulse shown in a. the laboratory frame and b. the rotating frame.

### 2.3.3 Description of the signal-inducing excited state (acquisition stage)

In the laboratory frame, after excitation, the magnetization vector may have a longitudinal component  $M_z$  along the z-axis and a transverse component  $\mathbf{M}_{xy}$  in the xy-plane. After excitation,  $\mathbf{B}_1$  is turned off and the magnetization vector is now under the influence of only one magnetic field i.e.  $\mathbf{B}_0$ . The transverse component of the magnetization vector is described here in complex form as:

$$\mathbf{M}_{xy} = (M_x, M_y, 0) = M_x + iM_y \quad (2-23)$$

where,  $i = \sqrt{-1}$ .

The equations of motion for the transverse component of the moment vectors can be expressed by equating the rate of change of angular momentum to the torque experienced by those moment vectors.<sup>5</sup>

$$\frac{\hbar}{2\pi} \frac{d\mathbf{I}}{dt} = \boldsymbol{\mu} \times \mathbf{B}_0 \quad (2-24)$$

From Eq. 2-2, we obtain:

$$d\boldsymbol{\mu} / dt = \gamma \boldsymbol{\mu} \times \mathbf{B}_0 \quad (2-25)$$

From Eq. 2-10 the equation of motion now becomes:

$$\frac{d}{dt} (\sum \boldsymbol{\mu}_{xy}) = d\mathbf{M}_{xy} / dt = \gamma \sum \boldsymbol{\mu}_{xy} \times \mathbf{B}_0$$

$$d\mathbf{M}_{xy} / dt = \gamma \mathbf{M}_{xy} \times \mathbf{B}_0 \quad (2-26)$$

$$d\mathbf{M}_{xy} / dt = \gamma \begin{vmatrix} \hat{i} & \hat{j} & \hat{k} \\ M_x & M_y & 0 \\ 0 & 0 & B_0 \end{vmatrix} = \gamma (M_y B_0 \hat{i} - M_x B_0 \hat{j}), \quad (2-27)$$

or, in complex form:

$$d\mathbf{M}_{xy} / dt = \gamma (M_y B_0 + i(-M_x B_0))$$

$$d\mathbf{M}_{xy} / dt = \gamma B_0 (M_y - iM_x) \quad (2-28)$$

$$d\mathbf{M}_{xy} / dt = -i\gamma B_0 M_{xy}$$

Solving the differential equation above with the initial condition that  $\mathbf{M}_{xy} = iM_0$  at  $t = 0$ :

$$\mathbf{M}_{xy}(t) = iM_0 \exp(-i\gamma B_0 t) \quad (2-29)$$

Thus the magnetization vector precesses around the z-axis with frequency  $\omega_0 = \gamma B_0$ . The rotation is in the negative sense (clockwise) for protons where  $\gamma$  is positive. It is important to note that the  $\mathbf{M}_{xy}$  rotates about the z-axis in the same manner and frequency required to achieve the on-resonance excitation described in the excitation stage.

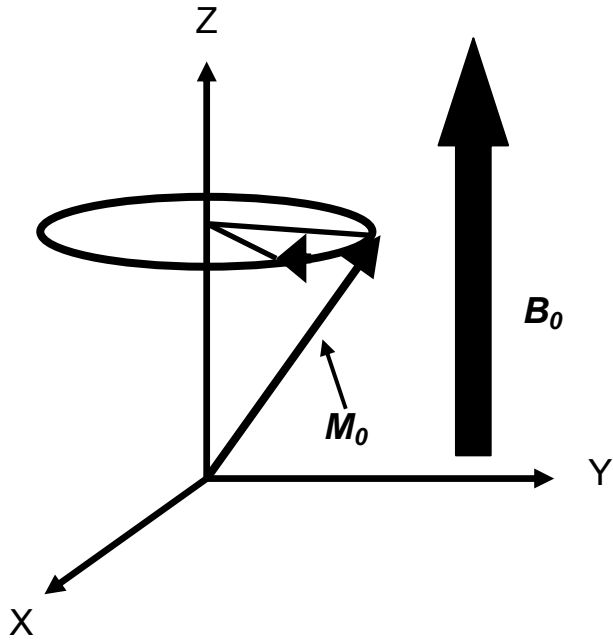


**Figure 2-6: Magnetization vector  $M_0$  precessing in a negative sense about the z-axis in the presence of a static magnetic field  $B_0$  applied along the z-direction.**

By placing an antenna adjacent to our excited sample, the rotating magnetization vector would induce a current in the conductor resulting in the detection of the signal.<sup>1</sup> The Fourier transform of the detected current is a peak at the resonance frequency  $\omega_0$  of the magnetization vector. (Fig. 2-7)

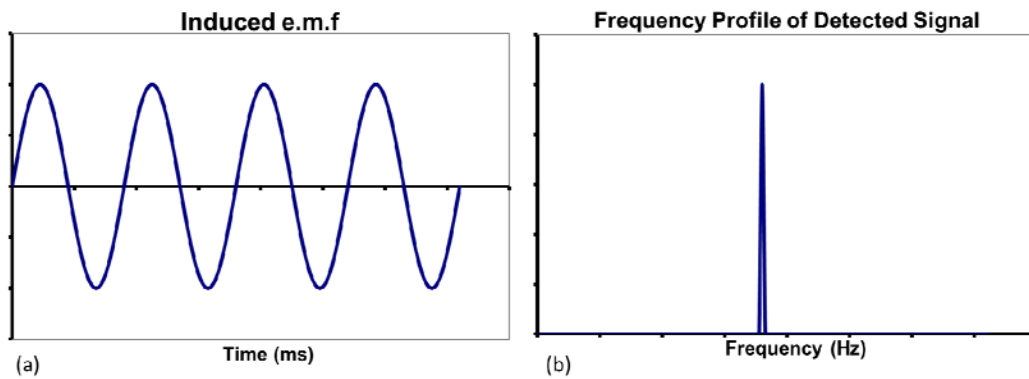


**Figure 2-7: (a) the time domain induced e.m.f in the coil and (b) frequency profile of the detected signal. (Ignoring relaxation)**

## 2.4 Relaxation mechanisms and the Bloch equations

The magnetic moments represented by the magnetization vector  $\mathbf{M}$  do not revolve indefinitely around the z-axis after excitation. Magnetic moments tend to relax to their equilibrium state along the z-axis resulting in a reduction in the measurable signal over time. The relaxation process is controlled by two related processes of longitudinal and transverse relaxation.

### 2.4.1 Longitudinal relaxation

Longitudinal relaxation describes the change of the  $M_z$  component of the magnetization vector  $\mathbf{M}$  from the excited state to its thermal equilibrium state  $M_0$ . Longitudinal relaxation is also known as  $T1$  relaxation where the longitudinal relaxation time is  $T1 = 1/\text{relaxation constant}$ . Longitudinal relaxation occurs through spin-lattice interactions where energy is exchanged between the resonant nuclei and the surrounding molecular lattice. Any one proton in a sample is closely surrounded by similar magnetic dipoles giving rise to inter-nuclear dipole fields of the same order of magnitude of  $B_1$  used in the excitation stage. Those microscopic magnetic fields are randomly changing due to the motion of the dipole lattice. Such change results in energy exchange between the spins and the lattice.

The energy exchange rates depend on the molecular lattice; accordingly, different materials exhibit different exchange rate. Bloch and Purcell, in independent accounts, showed that the longitudinal relaxation rate was proportional to the degree by which the magnetic moments have been removed from the thermal equilibrium state.<sup>6, 7</sup> Thus, the change in longitudinal component of the magnetization vector is expressed as:

$$dM_z(t)/dt = \frac{1}{T1}(M_0 - M_z(t)) \quad (2-30)$$

where  $M_0$  is the thermal equilibrium state magnetization and  $T1$  is the longitudinal relaxation time, a constant that varies for different materials.

The first order differential equation gives:

$$M_z(t) = M_0 + (M_z(0) - M_0)e^{-t/T1} \quad (2-31)$$

For a  $90^\circ$  pulse,  $M_z(0) = 0$ , and  $M_z(t)$  becomes:

$$M_z(t) = M_0(1 - e^{-t/T1}) \quad (2-32)$$

and for an  $180^\circ$  pulse,  $M_z(0) = -M_0$ , and  $M_z(t)$  becomes:

$$M_z(t) = M_0(1 - 2e^{-t/T1}) \quad (2-33)$$

Table 2-1 shows different  $T1$  values for different tissue at both 1.5T and 3.0T.<sup>3, 5</sup> Contrast between tissues can be obtained through the choice of an appropriate timing as shown in Fig. 2-8 and Fig. 2-9.

**Table 2-1: T1 value of different tissue at 1.5T and 3T.**

Tissue	T1 (ms) @ 1.5 Tesla	T1 (ms) @ 3.0 Tesla
White Matter	790	850
Grey Matter	920	1300
Cerebrospinal Fluid (CSF)	> 4000	> 4000
Muscle	870	1073
Fat	250	419

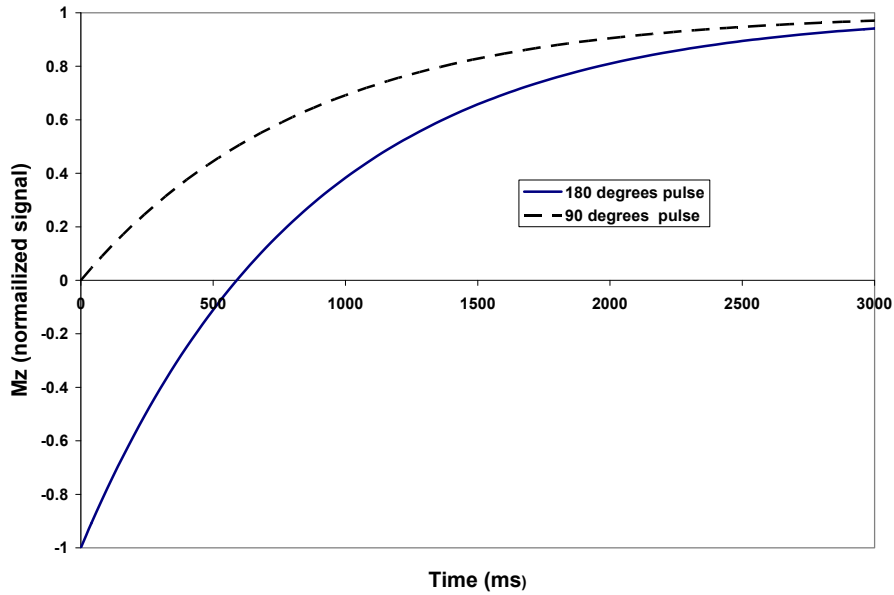


Figure 2-8: longitudinal relaxation of white matter at 3T following a 90° pulse and an 180° pulse.

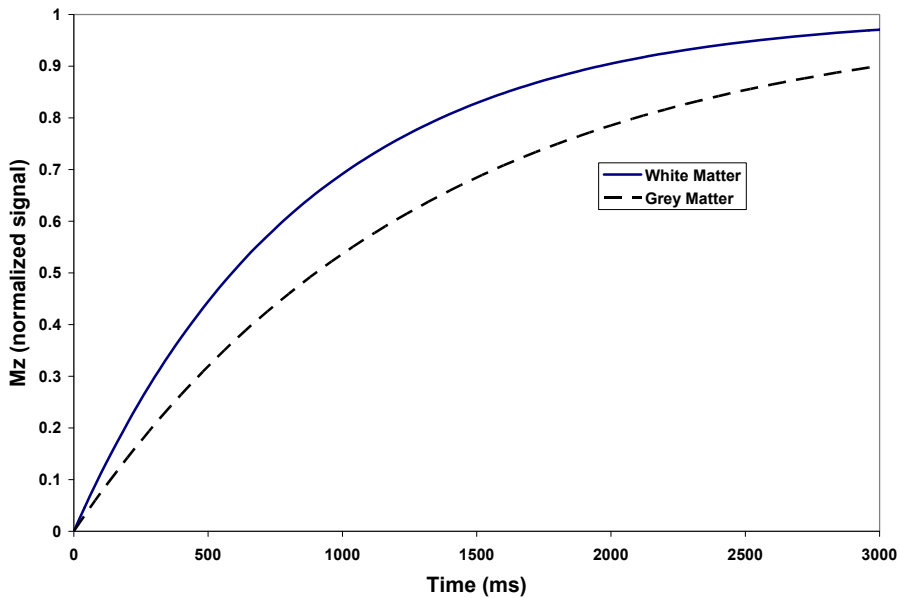


Figure 2-9: longitudinal relaxation of white matter and grey matter at 3T following a 90° pulse.

## 2.4.2 Transverse Relaxation

Transverse relaxation describes the decay of the  $M_{xy}$  component of the magnetization vector  $M$  from its excited state back to its thermal

equilibrium state. Transverse magnetization is more complicated than longitudinal relaxation as it is composed of two processes, a reversible time-independent process and an irreversible time-dependent process.

Similar to longitudinal relaxation, transverse relaxation is governed by a relaxation constant  $k'$ , where the transverse relaxation time  $T2^* = 1/k'$ . The reversible and irreversible components of  $T2^*$  relaxation are defined as <sup>2</sup>:

$$\frac{1}{T2^*} = \frac{1}{T2} + \frac{1}{T2'} \quad (2-34)$$

where  $T2$  and  $T2'$  are the irreversible and reversible components respectively.

Similar to Eq. 2-30, the rate of change of  $M_{xy}$  is expressed as:

$$dM_{xy}(t)/dt = \frac{1}{T2^*} (0 - M_{xy}(t)) \quad (2-35)$$

The first order differential equation gives:

$$M_{xy}(t) = M_{xy0} e^{-t/T2^*} \quad (2-36)$$

The reversible component  $T2'$  arises from the inhomogeneity in the main static magnetic field  $B_0$  as experienced by different protons in the sample. Due to manufacturing imperfections in the hardware and varying magnetic susceptibilities within the sample, not all protons experience the same magnetic field  $B_0$ . This causes the signal generating protons to have slightly different precession frequencies and a loss of coherence in transverse magnetization. However, since this decay component is constant in time, it can be reversed by using so called echoes, as we will show later.

The irreversible component  $T2$  results from several factors.<sup>8</sup> Among the various factors is the spin-spin interaction which is similar to the same mechanism in longitudinal relaxation. In spin-spin interactions, an excited

dipole produces a magnetic field similar in effect to  $B_1$  and excites the surrounding dipole moments. Moreover, fluctuation of the resonance frequency  $\omega_0$  due to molecular vibrations and rotations result in the loss of coherence in the detected signal and also contributes to  $T_2$ .(Fig. 2-10) These mechanisms result in permanent loss in the detectable signal and is hence called, irreversible decay. Table 2-2 shows typical  $T_2$  times at 1.5 T.

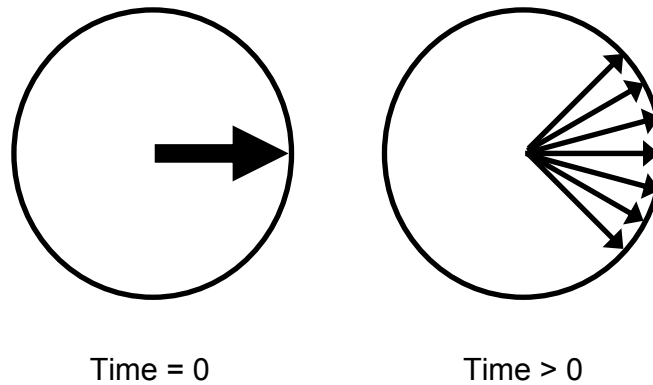


**Figure 2-10: Fluctuations in  $\omega_0$  resulting in phase spread and loss of coherent signal.**

**Table 2-2: T2 values for brain tissue at 1.5 T.**

Tissue	T2 (ms)
White Matter	92
Grey Matter	100
Muscle	470

## **2.5 Spatial Encoding**

Spatial encoding is the process by which the signal received in an NMR experiment is related to the location it corresponds to within the anatomy. Spatial encoding distinguishes MRI from any NMR experiment. The Imaging in Magnetic Resonance Imaging comes from the ability to correlate physical location with the signal received. To do this, a linearly varying magnetic field gradient with slope  $G_r$  is applied along the direction of the main field  $B_0$  resulting in a spatial varying  $B_{total}$  :

$$B_{total} = B_0 + \mathbf{G}_r \bullet \mathbf{r} \quad (2-37)$$

where  $\mathbf{r}$  is the displacement along the direction of the gradient  $\mathbf{G}_r$ . (Fig. 2-11)

The resonance frequency now becomes linearly varying as:

$$\omega_{total} = \gamma(B_0 + \mathbf{G}_r \bullet \mathbf{r}) \quad (2-38)$$

In the rotating frame Eq. 2-38 becomes:

$$\omega_p = \omega(r) = \gamma \mathbf{G}_r \bullet \mathbf{r} \quad (2-39)$$

Equation 2-39 is the basis for the spatial encoding used in three ways in MRI as described in the following sections.

Spatial encoding is achieved using primarily three methods; slice selection, frequency encoding, and phase encoding. Each of those methods makes use of the magnetic field gradients to either limit the excitation to a certain region of the object or to spatially encode the excited volume into smaller voxels.

### 2.5.1 Slice Selection

In slice selection, a gradient  $\mathbf{G}_z$  is applied simultaneously with the bandwidth limited RF pulse. As shown in Fig. 2-11 the gradient results in spreading the resonance frequencies of the spins along the slice direction (direction of the gradient). The pulse used to excite the spins is a shaped RF envelope with bandwidth  $BW_{rf}$  and therefore excites the spins whose resonance frequencies lie within the bandwidth of the pulse.<sup>9</sup> Hence:

$$\begin{aligned} BW_{rf} &= \gamma G_z \Delta z / 2\pi \\ \Delta z &= 2\pi BW_{rf} / \gamma G_z \end{aligned} \quad (2-40)$$

where  $\Delta z$  is the slice thickness.

The slice location can be changed by changing the center frequency of the RF pulse.

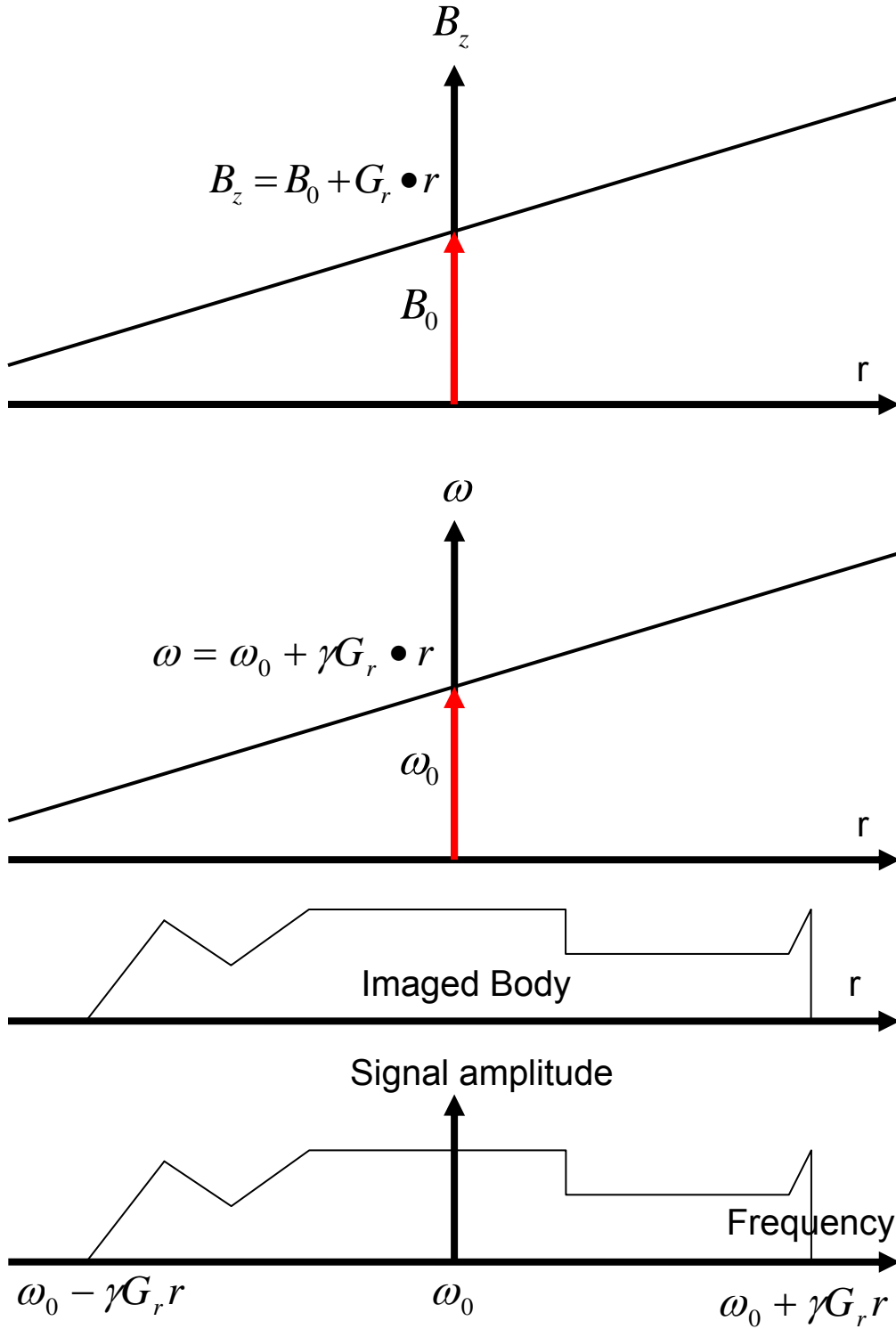
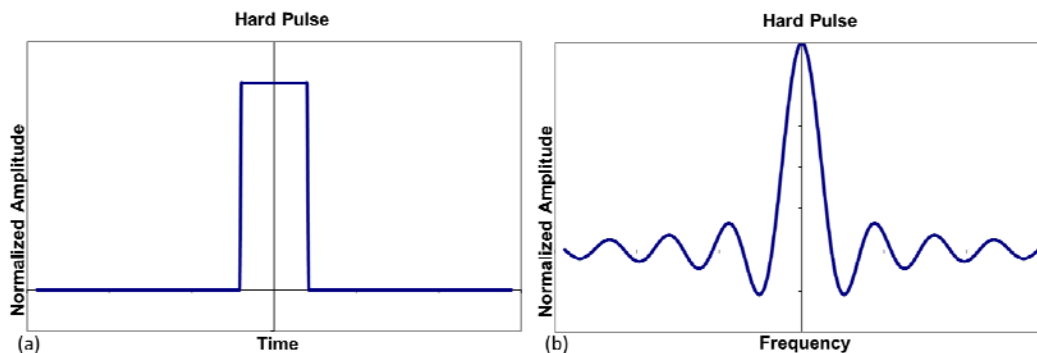


Figure 2-11: A description of the application of magnetic field gradients for spatial encoding.

### 2.5.1.1 Radio-Frequency excitation pulses

Equation 2-40 shows that as the slice selection gradient spreads the frequencies of the spins over a certain range, the bandwidth of the RF pulse is the limiting factor of the slice thickness. The frequency profile of an RF pulse is simply the Fourier transform of the time domain pulse signal. The bandwidth of the pulse ( $BW_{rf}$ ) is defined as the full width at half maximum of that frequency profile.

Two of the basic RF pulses used in MRI are hard and soft pulses. Hard pulses have a square envelope in the time domain and have a corresponding sinc function frequency profile. Hard pulses have the advantage of achieving large tip angles in a very short time. However, due to its frequency profile, it is considered a broadband pulse that results in poor slice definition. (Fig. 2-12) The side lobes in the frequency profile of the pulse lead to contamination of signal of the slice with signal from neighboring slices.



**Figure 2-12: An ideal hard pulse envelope as shown in a. time domain and b. frequency domain.**

Soft pulses on the other hand, have truncated sinc pulse envelopes in the time domain with a corresponding approximately square frequency profile.<sup>10</sup> Although soft pulses have a relatively long play time, the resulting frequency response get sharper and better defined with greater time lengths. It is a trait that is sought for in imaging since it provides sharply defined slices as shown in Fig. 2-13.

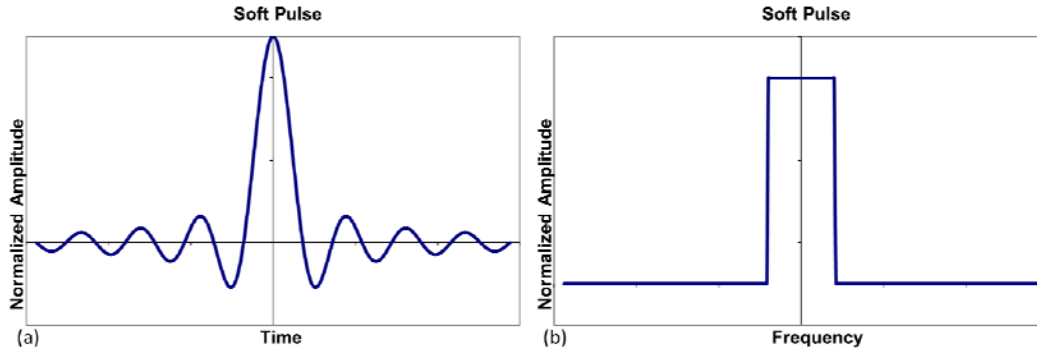


**Figure 2-13: An ideal soft pulse envelope as shown in a. time domain and b. frequency domain (assuming infinite time domain playtime).**

The latter observation is true for all pulses. As a general rule of thumb, the time domain play time and frequency domain bandwidth are inversely proportional. This means that the narrower the time domain profile of a pulse is, the wider its frequency profile and visa-versa.

## 2.5.2 Frequency Encoding

In frequency encoding, a gradient is applied during the acquisition of the signal along any arbitrary direction. For the purposes of this thesis we'll assume that the frequency encoding gradient is applied along the x-direction of the laboratory frame. In this case, the gradient will be referred to as  $\mathbf{G}_x$ . As in slice selection, the gradient has the effect of spreading the resonance frequencies of the spins along the direction of the gradient. This leads to a frequency spread in the acquired signal. The frequency spread can be detected by Fourier transforming the acquired time domain signal into its frequency components which are directly related to the spatial locations along  $\mathbf{G}_x$ . The range of frequencies in the acquired signal is related to the gradient strength and field-of-view by:

$$\Delta f_{\max} = \gamma \mathbf{G}_x (x_{\max} - x_{\min}) / 2\pi = \gamma \mathbf{G}_x \text{FOV}_x / 2\pi \quad (2-41)$$

where  $\text{FOV}_x$  is the field-of-view in the x-direction and is equal to  $(x_{\max} - x_{\min})$ .

Assuming  $\text{FOV}_x$  is centered around 0, the maximum frequency in the acquired signal is predictable and defined as:

$$f_{\max} = \gamma G_x FOV_x / 4\pi \quad (2-42)$$

Since the acquired signal is digitized into the MRI system, to avoid aliasing, the sampling frequency of the acquired signal must be greater than or equal to twice the maximum frequency of the signal as stated by Nyquist criteria. Hence, the sampling bandwidth of the signal acquired in the frequency encoding direction must be:

$$BW_{sam} \geq \gamma G_x FOV_x / 2\pi \quad (2-43)$$

Aliasing is usually eliminated in scanners by using a higher sampling bandwidth than required by the Nyquist criterion and using a band-pass filter that only allows the frequencies within the acquisition sampling bandwidth.

### 2.5.3 Phase Encoding

Phase encoding is similar to frequency encoding in that it uses gradients and accumulating phase to encode for the y-direction. A gradient  $G_y$  is switched on for a fixed time  $\tau$  before acquisition. This results in the accumulation of phase that is linear with the position along the phase encoding direction. Accordingly, at the start of the acquisition the all spins along a vector in the phase-encoding (y) direction will have the same resonance frequency but with phase spread linearly along the y-direction.

$$\phi(y) = \gamma \int_{\tau} G_y(t') \cdot y dt' \quad (2-44)$$

where  $\phi$  is the phase accumulated before acquisition.

To mimic frequency encoding, the gradient strength is incremented by discrete linear increments of  $\Delta G_y$  before each acquisition. The resulting distribution of phase along the phase encoding direction resembles pseudo-frequencies that are linearly related to the spins' y location. The maximum phase shift between two adjacent points is given by:

$$\Delta\phi_{\max} = 2\pi\Delta f_{\max}\tau = \gamma\tau\Delta G_y FOV_y / 2 \quad (2-45)$$

where  $FOV_y$  is the field-of-view in the phase encoding direction.

Similar to frequency encoding, to satisfy the Nyquist criteria the maximum phase shift between adjacent samples must be less than or equal to  $\pi$ . The gradient increments then have to be:

$$\begin{aligned} \gamma\tau\Delta G_y FOV_y / 2 &\leq \pi \\ \Delta G_y &\leq 2\pi / (\gamma FOV_y \tau) \end{aligned} \quad (2-46)$$

## 2.6 The Signal Equation

The focus of this section is to discuss the signal received after excitation and spatial encoding and how this signal is processed to give us the image we desire. For simplicity we will consider a basic two-dimensional sequence whose resulting signal is detected by a phase sensitive detector. We shall also ignore  $T_2$  relaxation for the time being.

In the selectively excited slice, the receiving coil detects the signal from all the precessing spins. The received signal is the sum of all transverse magnetization in the excited slice. The frequency and phase encode gradients result in a phase shift in the detected signal that is equal to the area under the gradient as experienced by each spin. The sum of the received signals from the magnetization vector  $\mathbf{M}_{xy}$  can be written as an integral:<sup>5</sup>

$$S(t) = \iint_{x,y} M(x,y) \exp[-i\gamma \int_0^t G_x(t') \bullet x dt' - i\gamma \int_0^t G_y(t') \bullet y dt'] dy dx \quad (2-47)$$

Consider defining a new variable  $k$  where:

$$\begin{aligned} k_x(t) &= \frac{\gamma}{2\pi} \int_0^t G_x(t') dt' \\ k_y(t) &= \frac{\gamma}{2\pi} \int_0^t G_y(t') dt' \end{aligned} \quad (2-48)$$

Substituting with Eq. 2-48 in Eq. 2-47:

$$S(k_x, k_y) = \int_x \int_y M(x, y) e^{-i2\pi(k_x(t)x + k_y(t)y)} dy dx \quad (2-49)$$

It is very important to notice the similarity between Eq. 2-49 and the definition of the Fourier transform.<sup>11</sup> Such similarity allows us to reconstruct the distribution of the signal  $M(\mathbf{x}, \mathbf{y})$  in the form of an image using the 2-D inverse Fourier transformation.

The introduction of the terms  $k_x$  and  $k_y$  in our discussion lead to questions about their significance.  $k_x$  and  $k_y$  are components in k-space in which spatial frequency space (k-space) replaces the normally understood displacement real space. For instance if an MRI image is Fourier transformed in 2 dimensions, the result would be an image with the same number of points but in k-space. Thus, in order to correctly acquire a complete high-resolution image, all k-space points of the image have to be correctly sampled. As it has been described before and through Eq. 2-49, this is achieved through the application of gradients in the frequency and phase encoding.

To illustrate how k-space is sampled in MRI, consider a 2D gradient echo sequence. As in Fig. 2-14 the sequence is divided into time  $t1$  and time  $t2$ . During  $t1$ , the phase encode gradient ( $G_y$ ) and negative half readout gradient ( $G_x$ ) are on. Both gradients result in a shift in accumulated phase to the k-space coordinates ( $k_x1, k_y1$ ). For a time  $t2$  the frequency encode (readout) gradient is turned on, phase is accumulated in the x-direction, and the signal is acquired leading to a precession of the coordinates through a row of  $k_x$  in k-space.<sup>5</sup> In the next acquisition, the same steps are repeated but with incrementing the phase encoding gradient  $G_y$  by  $\Delta G_y$ . This results in sampling another row of k-space. This process is repeated until all k-space is properly sampled. There are of course several ways in which k-space can be sampled each with its pros and cons and it is generally a process optimized for each application.<sup>2, 3, 12</sup>

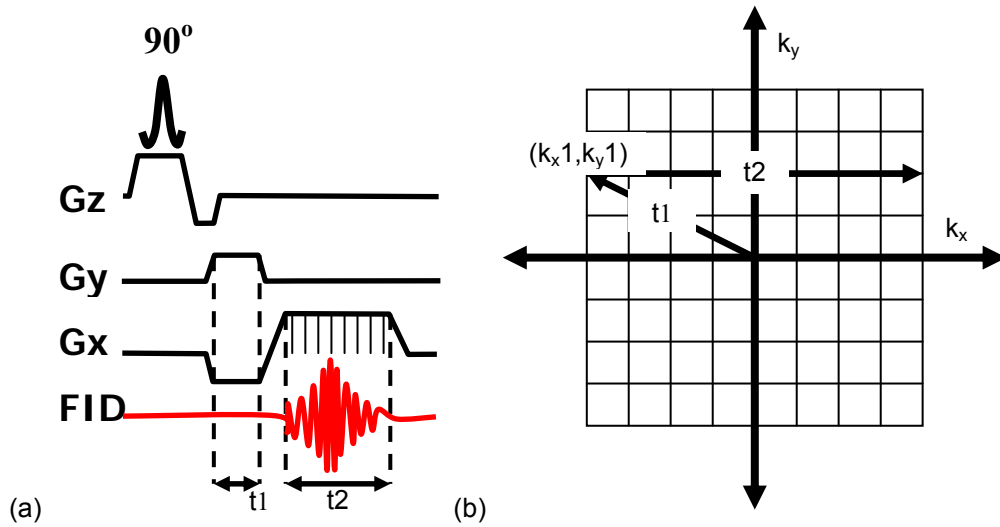


**Figure 2-14: a. Schematic of a gradient echo sequence. b. The k-space sampling trajectory caused by the application of the gradients in the sequence.**

According to the sampling theory, sampling in one domain corresponds to replication in the corresponding transform domain.<sup>5</sup> Since in MR sampling is done in k-space, the replication of the image must be considered. Replication occurs at intervals of  $1/\Delta k_x$  and  $1/\Delta k_y$  in the x and y directions respectively.<sup>5</sup> The field of view is therefore related to the k-space sampling rate through:

$$FOV_x = 1/\Delta k_x = \frac{2\pi}{\gamma G_x \Delta t} = \text{sampling rate in } k_x \quad (2-50)$$

$$FOV_y = 1/\Delta k_y = \frac{2\pi}{\gamma \Delta G_y \tau} = \text{sampling rate in } k_y \quad (2-51)$$

Similarly, the extent of sampled k-space is related to the spatial resolution through:

$$\begin{aligned} FOV_{k_x} &= \Delta k_x N_F = 1/\Delta x \\ FOV_{k_y} &= \Delta k_y N_P = 1/\Delta y \end{aligned} \quad (2-52)$$

$$\begin{aligned} \Delta x &= 1/\Delta k_x N_F = FOV_x / N_F \\ \Delta y &= 1/\Delta k_y N_P = FOV_y / N_P \end{aligned} \quad (2-53)$$

Therefore, the nominal in-plane voxel dimensions can be determined by dividing the field of view by its corresponding phase/frequency encoding steps.

## 2.7 MR spectroscopy

Magnetic resonance imaging is based on imaging primarily water protons, as it is the most abundant molecule in the human body, and relies heavily on differences in relaxation times as a source of contrast. As opposed to imaging which relies on all protons having the same resonance frequency, MR spectroscopy (MRS) exploits the chemical shift phenomenon to detect different chemical compositions within a sample.

Since atoms are the building blocks of molecules, nuclei within those atoms are affected by the distribution of electrons in the chemical bond in the molecule. That distribution of electrons affects the resonance frequency of the protons in the molecule. This dependence of the resonance frequency on the molecular structure compared to a water proton is known as the chemical shift.

Nuclei within the molecules are shielded from the static magnetic field  $B_0$  through the electron cloud surrounding them. According to Lenz's law, due to circulation induced by  $B_0$  in the electron cloud, a magnetic field  $B_i$  is induced by the electron cloud to oppose the circulation from  $B_0$ . The induced field  $B_i$  has a magnitude that is proportional to the original field  $B_0$  and a direction opposite to  $B_0$ , thus:

$$B_{local} = B_0 - B_i . \quad (2-54)$$

The induced field is directly proportional to the applied field with the constant of proportionality being  $\sigma$ , the shielding constant.  $\sigma$  is unique to the local environment of the nucleus.<sup>5</sup> Therefore Eq. 2-54 becomes:

$$B_{local} = B_0(1 - \sigma) \quad (2-55)$$

Therefore, the precession frequency  $\omega$  of those protons is:

$$\omega = \gamma B_0(1 - \sigma) \quad (2-56)$$

So,

$$\sigma = \frac{\Delta\omega}{\omega_0}$$

Accordingly, the frequency shift between the protons in different electronic environments is dependent on the applied magnetic field; the larger the field, the larger the shift. Therefore the use of high fields would improve peak separation and spectral resolution as well as the SNR as shown in the following sections.

Due to the dependence of the chemical shift frequency on the applied field, a the parts-per-million (ppm) ,  $\delta$ , scale is used as a normalized measure of chemical shift.<sup>5</sup>

$$\delta = \frac{\omega_{molecule} - \omega_{reference\ molecule}}{\omega_{reference\ molecule}} \times 10^6 \text{ ppm} \quad (2-57)$$

Most relevant metabolites of interest *in-vivo* are in the range of 1-4.7 ppm. Such range corresponds to a frequency spread of approximately 473 Hz and 236 Hz at 3T and 1.5T respectively.

## **2.8 Localization Techniques of MRS**

For single voxel spectroscopy, localization of the source of the signal is important. The most popular techniques for localization involve applying three RF pulses on the three orthogonal planes, where the intersection of the planes defines the voxel from which the signal is acquired. Stimulated Echo Acquisition Mode (STEAM) and Point Resolved Spectroscopy (PRESS) are the most popular spectroscopy of those pulse sequences that utilize this method of localization.

### 2.8.1 Stimulated Echo acquisition Mode (STEAM)

STEAM uses three  $90^\circ$  excitation pulses applied on the three orthogonal planes. The three excitation pulses generate a stimulated echo only at the intersection of the three planes therefore acquiring the signal from the defined cube.<sup>13</sup> Echo time (TE) is independent of the mixing time (TM) between the second and the third pulse. Accordingly, TM can be easily adjusted and the overall scan time can be reduced significantly compared to PRESS.

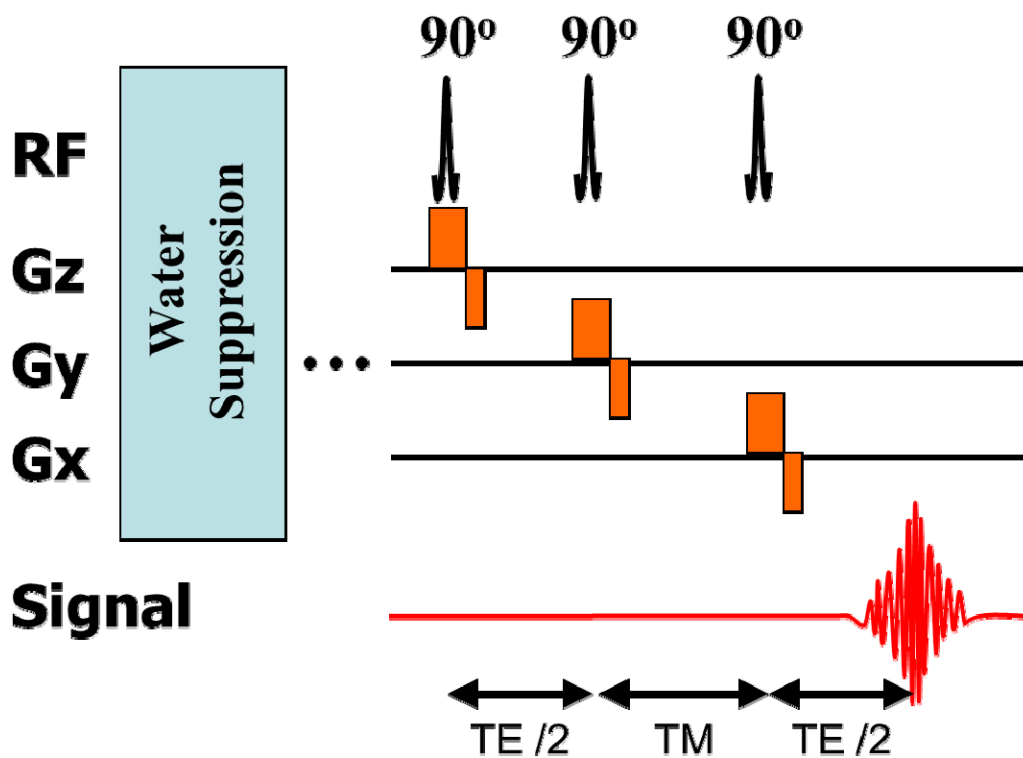


Figure 2-15: Schematic for a STEAM sequence. The three  $90^\circ$  excitation pulses applied on the three orthogonal planes define a volume of interest (voxel) from which the signal is acquired.

### 2.8.2 Point Resolved Spectroscopy (PRESS)

Similar to STEAM, PRESS relies on three RF pulses. However, in the case of PRESS, the first  $90^\circ$  excitation pulse is followed by two  $180^\circ$  pulses generating a spin echo at the intersection of the 3 planes on which they are applied.<sup>14-16</sup>

PRESS and STEAM each have different advantages and disadvantages. STEAM permits the detection of metabolites with shorter T2 relaxation due to its shorter TE compared to PRESS. However, PRESS inherently has a higher SNR due to the inherent loss of signal in the stimulated echoes.

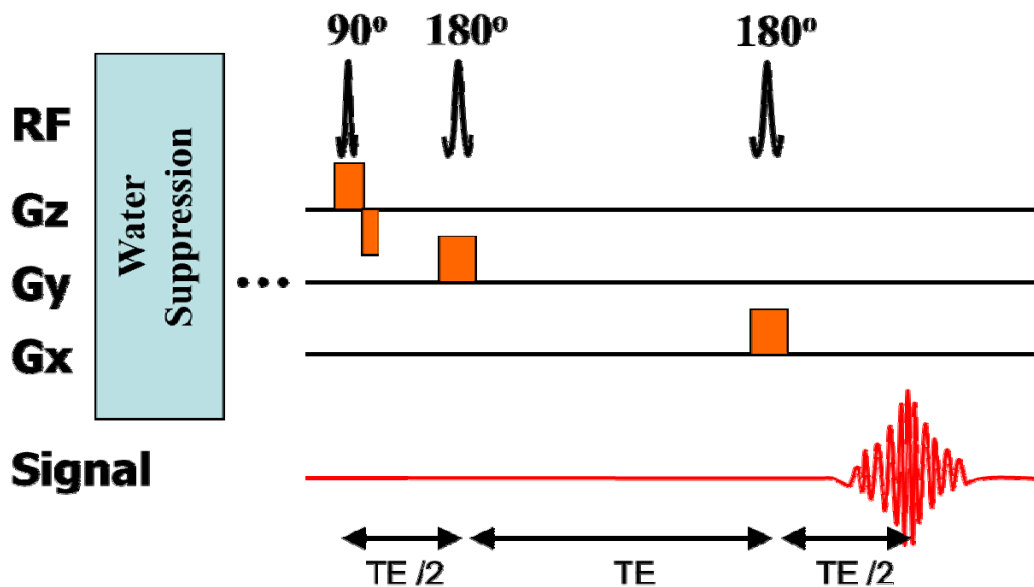


Figure 2-16: Schematic of a PRESS Sequence. Similar to STEAM, the 90° excitation pulse along with the two 180° refocusing pulses applied on the three orthogonal planes define a volume of interest (voxel) from which the signal is acquired.

The biggest disadvantage of MRS is that the entire signal within the defined volume of interest is summed and only one relatively large voxel is acquired leaving out any spatial information. Hence, prior knowledge of the location of the spectroscopy target is needed to decide the location of the single voxel.

### 2.8.3 Spectroscopic Imaging (SI) (Chemical Shift Imaging)

As in MRI, spatial encoding can be used to transform single-voxel MRS to multi-voxel MR spectroscopic imaging (MRSI).

Recall the signal equation ignoring chemical shift is shown in Eq. 2-50:

$$S(k_x, k_y) = \iint_{x, y} M(x, y) e^{-i2\pi(k_x x + k_y y)} dy dx \quad (2-50)$$

However, if the spins are allowed to precess under chemical shift, that results in an additional accumulated phase which has to be accounted for in the signal equation. Accordingly, Eq. 2-50 becomes <sup>5</sup>:

$$S(k_x, k_y, t) = \iiint_{\sigma \ x \ y} M(x, y, \sigma) e^{-i2\pi(k_x x + k_y y + \sigma f_0 t)} dy dx d\sigma \quad (2-58)$$

where  $t$  is the acquisition time, and  $\sigma$  is the relative chemical shift defined

$$\text{as } \sigma = \frac{\Delta\omega}{\omega_0} \text{ and } k_f \text{ can be defined as } k_f = \sigma f_0.$$

Hence, to fill the spatio-temporal frequency space (k-space) we need to fill  $k_x$ ,  $k_y$  and  $k_f$ . After acquisition, a 3-D inverse Fourier transform is performed to reconstruct the signal from k-t space to xy- $\sigma$  space.

In the most common spatial encoding methods, the nuclei are left to precess under their natural precession frequencies, i.e. chemical shift, and accordingly, no readout gradient is applied in the frequency encoding direction. Instead, both x and y directions are phase encoded.

The advantage of 2-D phase encoding is that it is a simple spatial encoding method which can be incorporated to any MRS sequence hence transforming the single voxel sequence to an SI one. The most popular sequence, 2-D PRESS, is shown in Fig. 2-17. The main shortcoming of 2-D phase encoding is very long scan time. For 32×32 voxel scans, we have to step through k-space one step per repetition time (TR), resulting in 1024 repetitions. Therefore, for a 1500 ms TR, a 32×32 voxel scan would take approximately 26 minutes. Furthermore, phase encoding can be applied in the z-direction to perform multi-slice MRSI.<sup>17</sup> In that case, an additional Fourier transform in the z-direction is needed to reconstruct the voxels.

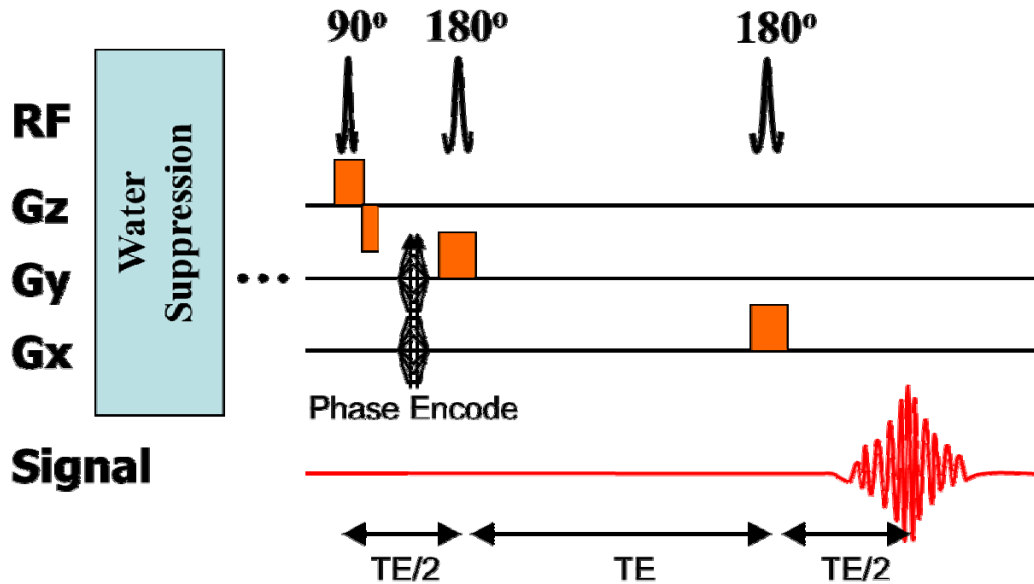


Figure 2-17: A schematic of a 2-D PRESS sequence.

## 2.9 Signal and Noise Considerations

In MRSI, the signal-to-noise ratio (SNR) is a very important factor that determines the quality of the spectra acquired in the scans. The need to maximize the SNR while maintaining achievable imaging parameters is crucial for *in-vivo* scans where noise levels are usually higher than *in-vitro* experiments. This section discusses the dependence of the signal and noise on the imaging parameters and hardware.

### 2.9.1 Signal

The magnitude of the signal is proportional to 4 parameters:

1. Larmour frequency of the protons in the main magnetic field. EMF induced in the receiving coil is proportional to the rate of change of the magnetic flux  $\Phi_B$  which in turn is proportional to the Larmour frequency  $\omega_0$ .
2. The available magnetization vector  $M_0$  which is dependent on:
  - a. The energy difference between the spin-down and spin-up eigenstates. Where the relative populations of the spins in the spin-down / spin-up eigenstates at thermal equilibrium is:

$$N_{\downarrow} / N_{\uparrow} = e^{-\mu B_0 / kT} \quad (2-8)$$

where  $N_{\downarrow}$  and  $N_{\uparrow}$  are the populations of the spins in the spin-down and spin-up eigenstates respectively.

- b. The density of the spins in the sample
3. The amount of transverse magnetic field  $B_T$  that could be generated by the receiving coil. By reciprocity, this corresponds to the reception quality (sensitivity) of the receive coil which defines the ability of the coil to convert the change in magnetic flux to electromagnetic force.
4. The spin response to the imaging sequence and parameters. For instance, repetition time (TR), echo time (TE), and flip angle.

Ignoring the fourth parameter and assuming constant spin density, the signal  $S$  is then:

$$S \propto \omega_0 M_0 V B_T \quad (2-59)$$

where  $V$  is the voxel volume.

$M_0$  and  $\omega_0$  are both proportional to  $B_0$ , accordingly <sup>2, 5</sup>:

$$S \propto B_0^2 V B_T \quad (2-60)$$

### 2.9.2 Noise

The main source of noise in magnetic resonance is thermal noise resulting from the Brownian motion of electrons which in turn generate random magnetic fields. Thermal noise arises mainly from the resistance in the receiving coil and the resistance of the imaged body as observed by the coil. For thermal noise, the variance of the noise within the signal can therefore be described as <sup>5</sup>:

$$\sigma_n^2 = 4k T R BW_{sam} \quad (2-61)$$

where  $k$  is Boltzman's constant,  $T$  is the temperature in Kelvin, and  $R$  is the total resistance of the coil ( $R_c$ ) and the imaged body ( $R_b$ ).  $BW$  is the bandwidth of the signal which is equal to sampling bandwidth.

Thermal noise is Gaussian distributed, white, and additive; hence, noise is the square root the variance. From Eq. 2-61:

$$Noise = \sqrt{\sigma_n^2} \propto \sqrt{R} \quad (2-62)$$

and,

$$R = R_c + R_b \quad (2-63)$$

From Eq. 2-62 and Eq. 2-63:

$$Noise \propto \sqrt{R_c + R_b} \quad (2-64)$$

where  $R_c$  and  $R_b$  are proportional to  $\omega_0^{1/2}$  and  $\omega_0^2$  respectively.<sup>5</sup>

However, resistance in MRI is generally dominated by the resistance of the imaged body rather than the coil, hence Eq. 2-64 becomes<sup>5</sup>:

$$Noise \propto \sqrt{R_b} \propto \omega_0 \propto B_0 \quad (2-65)$$

Another factor affecting noise is the number of phase encodes. Due to the Fourier transforms applied to reconstruct the images, noise is averaged out. If k-space consists of  $N$  points in one direction, after the Fourier transform the noise is proportional to  $(1/N)^{1/2}$ .<sup>2, 5</sup> Accordingly, for phase encoding steps equal to  $N_P$ <sup>2, 5</sup>:

$$Noise \propto \frac{1}{(N_P)^{1/2}} \quad (2-66)$$

For MRSI, where phase is used to encode both the x and y directions:

$$Noise \propto \frac{1}{(N_{P_x} N_{P_y})^{1/2}} \quad (2-67)$$

Overall noise is then:

$$Noise \propto B_0 \left( \frac{1}{N_{P_x} N_{P_y}} \right)^{1/2} \quad (2-68)$$

### 2.9.3 Signal-to-Noise Ratio (SNR)

Recall Eq. 2-61 <sup>5</sup>:

$$\sigma_n^2 \propto BW_{sam} \quad (2-69)$$

where  $BW_{sam}$  is the readout sampling bandwidth and is defined as:

$$BW_{sam} = \text{Number of samples} / \text{readout time } (T_{readout}) \quad (2-70)$$

While the signal is independent of  $BW_{sam}$ , doubling the readout time ( $T_{readout}$ ) halves  $BW_{sam}$  which in turn decreases the noise by  $\sqrt{2}$  as shown in Eq. 2-71:

$$\text{Noise} = \sqrt{\sigma_n^2} \propto \sqrt{\frac{BW_{sam}}{2}} \quad (2-71)$$

Comparing  $SNR_1$  to  $SNR_2$  with readout times equal to  $T_{readout}$  and  $2 \times T_{readout}$  respectively:

$$SNR_2 / SNR_1 \propto \frac{S}{\sqrt{\frac{BW_{sam}}{2}}} \times \frac{\sqrt{BW_{sam}}}{S} = \sqrt{2} \quad (2-72)$$

Generally, the SNR is related to the readout time ( $T_{readout}$ ) such that <sup>5</sup>:

$$SNR \propto \sqrt{T_{readout}} \quad (2-73)$$

Therefore from Eq. (2-60), Eq. (2-68) and Eq. (2-73):

$$SNR \propto \frac{S \sqrt{T_{readout}}}{\text{Noise}} \propto \frac{B_0^2 V B_T \sqrt{T_{readout}}}{B_0 \left( \frac{1}{N_{P_x} N_{P_y}} \right)^{1/2}} \propto B_0 V B_T (N_{P_x} N_{P_y} T_{readout})^{1/2} \quad (2-74)$$

Therefore, in MRSI it is desirable to use high  $B_0$  field strengths and long readout times. Also, in high-resolution MRSI, high  $B_0$  field strengths help offset the decrease in SNR that occurs to the decrease in voxel size.

## References:

1. M. J. Bronskill, presented at the AAPM summer school proceeding, 1992
2. E. M. Haacke, R. W. Brown, M. R. Thompson and R. Venkatesan, *Magnetic Resonance Imaging: Physics principles and sequence design*. (John Willey & Sons, 1999).
3. S. D. Thomas, University of Alberta, 2001.
4. W. S. Hinshaw, presented at the Proceeding of the IEEE, 1983.
5. D. G. Nishimura, *Principles of Magnetic Resonance Imaging*. (Stanford University, 1996).
6. F. Block, "Nuclear induction," *Physical Review* **70**, 460-474 (1946).
7. E. M. Purcell, H. C. Torrey and R. B. Pound, "Resonance absorption by nuclear magnetic moments in a solid," *Physical Review* **69**, 37-38 (1946).
8. B. M.A. and R. C. Semelka, *MRI Basic Principles and Applications*. (John Wiley & Sons, 1995).
9. D. W. McRobbie, " Investigation of the slice characteristics in NMR imaging," *Phys. Med. Biol.* **31** (6), 613-626 (1986).
10. R. Freeman, "Shaped frequency pulses in high resolution NMR," *J. of Progress in NMR Spectroscopy* **32**, 59-106 (1998).
11. R. N. Bracewell, *The Fourier Transform and its Applications*. (McGraw-Hill, 1978).
12. J. Bishop and D. Plewes, presented at the 10th Annual Mtg. Soc. Magn. Reson. In Med., San Francisco, 1991.
13. J. Frahm, H. Bruhn, M. L. Gyngell, K. D. Merboldt, W. Hanicke and R. Sauter, "Localized proton NMR spectroscopy in different regions of the human brain in vivo. Relaxation times and concentrations of cerebral metabolites," *Magn. Reson. Med.* **11** (1), 47-63 (1989).
14. P. A. Bottomly, US Patent No. 4,480,228 (1984).
15. R. E. Gordon and R. J. Ordidge, presented at the Abstracts of the Society of Magnetic Resonance in Medicine 3rd Annual Meeting, New York, 1984.
16. R. J. Ordidge, M. R. Bendall, R. E. Gordon and A. Connelly, *Magnetic Resonance in Biology and Medicine*. (McGraw-Hill, New Delhi, 1985).
17. X. Li, H. Jin, Y. Lu, J. Oh, S. Chang and S. J. Nelson, "Identification of MRI and 1H MRSI parameters that may predict survival for patients with malignant gliomas " *NMR Biomed.* **17** (1), 10-20 (2004).

## Chapter Three

### 3 An updated method for automatic tumor delineation using MRSI

---

#### 3.1 Introduction

Quantifying the relative levels of choline to N-acetyl aspartate (NAA) has been the method of choice by many groups as a means to identify tumors in the brain.<sup>1-5</sup> Studies have shown that tumors exhibit a sharp increase in Choline coupled with a sharp decrease in NAA levels compared to normal brain tissue.<sup>6-11</sup> These opposing trends result in the Choline-to-NAA ratio providing a dramatic response to tumor presence. However, a barrier to the wide clinical application of this ratio in treatment planning has been the lack of a standardized method of tumor delineation. Differentiation between normal tissue and tumor has often been accomplished using visual assessment of magnetic resonance spectroscopic imaging (MRSI) spectra. Both the inherent inter-operator subjectivity of this visual method as well as the inter-patient variability in apparent metabolite concentrations has resulted in compromised differentiation between normal and tumor tissue.<sup>12</sup> Moreover, variations in scanning sequences between different scanning sites render cross-sectional inter-patient comparisons very complicated. As a means to address some of these concerns McKnight et al. introduced a statistical approach for assessing tumors based on biological data collected using MRSI.<sup>12</sup> This statistical model automatically separates voxels into normal tissue and tumor populations based on their relative concentrations of choline and NAA. Rather than relying on a strict metabolite ratio, the data are assigned a new metric, the Choline-to-NAA Index (CNI), which identifies the number of standard deviations a voxel is removed from the ratio of normal tissue. By relying on a statistical user-independent model,

this method circumvents the drawbacks of the visual assessment method. The statistical model also aides in identifying a normal tissue population of voxels that can be used as control for serial studies of the same patient. Further, the CNI method inherently accounts for inter-patient variability in metabolite concentrations, effectively normalizing the tumor delineation criterion to each patient.

In the CNI model it is assumed that the variation in the relative levels of choline to NAA in normal brain tissue is not significantly affected by partial volume effects of cerebrospinal fluid. The model also assumes that the tissue-type related variations in the relative levels of choline to NAA in normal brain tissue (i.e. white versus grey matter) are small compared to the difference between normal and diseased brain. Developments in MRSI sequences have facilitated the acquisition of high-resolution MRSI data in clinically acceptable scan times, a change that may call the aforementioned assumptions into question. The move to higher resolution has enabled the detectability of more variations within the relative levels of choline to NAA in normal tissue. For example, at a nominal voxel size of  $0.34 \text{ cm}^3$  detectable variations in metabolite concentrations between grey matter and white matter were reported.<sup>13</sup> With the variation in the choline to NAA levels of normal tissue increasing, it is essential to consider the implications with regard to the CNI method, and any possible modifications to the approach to improve its specificity in the high resolution regime.

In this work we are introducing a modification to the CNI model that would address the uncertainty in tumor delineation resulting from normal tissue variation. The original CNI method segregates voxels into tumor and normal tissue based solely on their CNI score to define tumor boundaries. In this work we argue that due to the nature of the distribution, the increased detectable variability of choline and NAA levels in normal tissue, and the statistical model itself, that there will always be a region of mixed population of normal tissue and tumor where simple thresholding is

insufficient to separate the tumor and normal tissue populations. Hence, our proposed modification would divide the voxels into three regions: 1. a high certainty normal tissue region, 2. a high certainty tumor region, and 3. an uncertainty region of mixed population.

## **3.2 *Materials and Methods***

### **3.2.1 MRSI sequence**

Scans were performed on a Philips Intera 3 T MRI (Philips Healthcare, Bothell, WA) unit together with a transmit/receive birdcage head coil. In total, twelve glioblastoma multiforme (GBM) clinical subjects and three healthy volunteer were scanned between April 2005 and February 2010. Two different scanning sequences were used to acquire the MRSI spectra. Six clinical subjects were scanned using a multi-slice 2-echo Spin Echo Spectroscopic Imaging (SESI) sequence. SESI offers the choice of acquiring more than one echo per repetition, hence decreasing the overall scan time while maximizing the coverage of the brain.<sup>14</sup> The TR was set to 3800 ms, the TE to 100 ms, and inter-echo spacing was set to 200 ms. In-plane nominal resolutions were set between 0.58 cm and 0.75 cm, while slice thickness was set between 1 cm, and 1.5 cm in order to maximize tumor coverage. The resulting nominal voxel sizes ranged between 0.39 cm<sup>3</sup> and 0.73 cm<sup>3</sup>. Another six clinical subjects were scanned using a multi-echo 3-D Point Resolved Spectroscopy sequence (3-D PRESS) which also acquired two echoes per repetition. The nominal voxel size for those studies ranged between 0.625×0.625×0.7 (0.274) cm<sup>3</sup> and 0.7×0.7×0.7 (0.343) cm<sup>3</sup>. Prior to running the MRSI scans, second order shimming was established over the volume-of-interest (VOI). Water suppression was achieved by a mix of chemical shift selective (CHESS) suppression and inversion recovery.

### **3.2.2 Processing**

The raw data acquired from the MRSI scans were processed on the scanner console using MR Systems Intera (release 2.5.3) (Philips Healthcare, Bothell, WA) software package. The frequency domain data was exported to Matlab (The MathWorks, Natick, MA) where it was further analyzed using software to integrate metabolite peak areas.<sup>15</sup> The peak fitting algorithm used fits a sum of complex Lorentzian functions to the acquired spectra.<sup>16</sup> The resulting Lorentzian parameters were used to analytically calculate the area under the choline and NAA peaks from each voxel.

### **3.2.3 Choline-to-NAA Index calculation**

As discussed earlier, the CNI statistical model is based on key assumptions that result in the following: (a) normal tissue can be considered as a coherent tightly packed population in terms of the relative choline to NAA levels detectable by MRSI, while (b) tumors exhibit a statistically significant variation in the relative choline to NAA levels that can be used to delineate the tumor. To differentiate the two populations; normal tissue and tumor, the choline levels are plotted against those of NAA, for every voxel, yielding a scatter plot. The data is fitted using linear regression, and the z-score (the perpendicular residual/standard deviation) is calculated for all voxels.<sup>12</sup> The criterion for normality is a z-score (CNI) of less than 1.95, corresponding to a 97.5% probability that the voxel belongs to the fitted Gaussian distributed population. Voxels with z-scores higher than 1.95 were excluded and the process then repeated until no points are excluded, i.e. all the remaining voxels met the criteria of normal tissue. The final best fit line and standard deviation are used to calculate the CNI for all the voxels in the scan. In addition to the clinical cases, this process was also performed on MRSI scans of healthy volunteers to illustrate the difference between CNI values in healthy brains and clinical GBM cases.

The distribution of the CNI scores for the healthy volunteers appears to be roughly symmetric about a CNI score of zero (Figure 3-1). The three volunteers' CNI histograms agree to within a reasonable extent. The histogram of the CNI scores for the clinical volunteers show some similarity to that of those of healthy volunteers in the central region of the histogram, while they also exhibit an extended tail towards higher CNI score which corresponds to the tumor population (Figure 3-2).

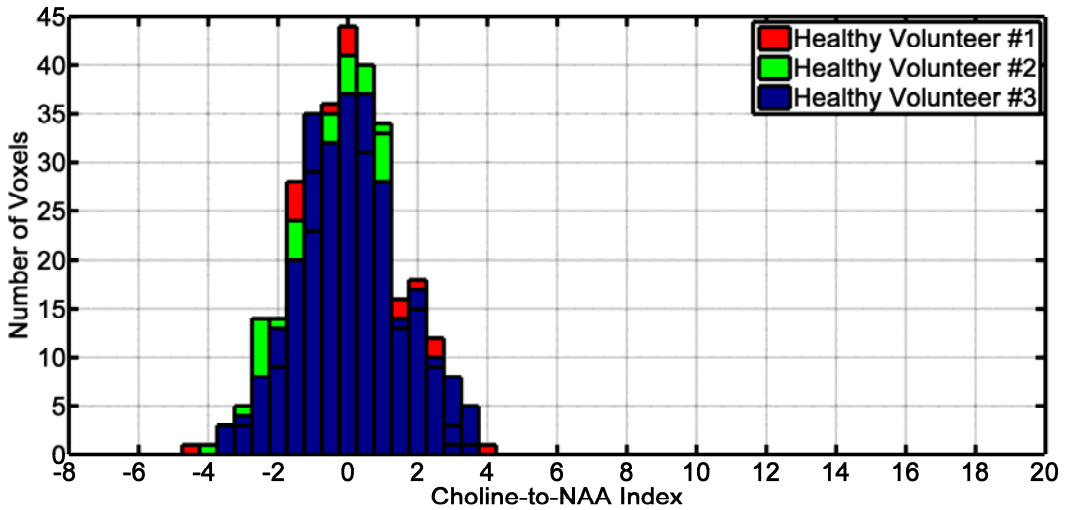


Figure 3-1: Histograms of CNI values for healthy volunteers.

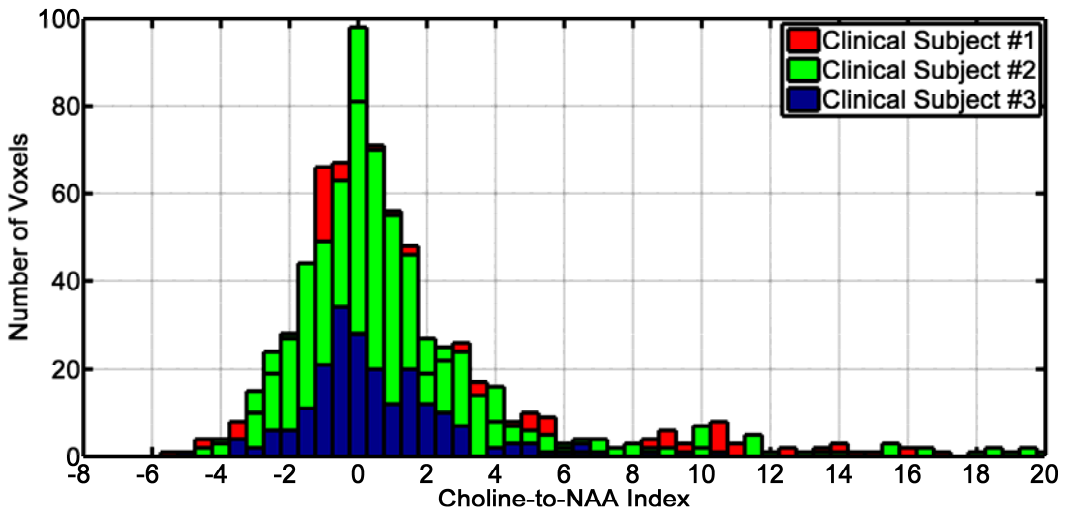


Figure 3-2: Histograms of CNI values for three GBM patients.

### 3.2.4 Tumor delineation

In the original CNI method, all points above the CNI = 2 line would lie outside the normal region and, since those points have a high choline/NAA ratio, would be associated with tumor. All points lying below the -2 CNI line have a low choline/NAA ratio and hence do not meet the tumor criterion. Those voxels are considered normal deviations from the normal distribution.

McKnight et al. (2001)<sup>12</sup> reported that during their studies of normal brain 5% of the all voxels scored higher than CNI = 2; i.e. incorrectly failed to pass the criteria of normal tissue.<sup>12</sup> Since delineation is based on the 2 standard deviation line, it would be expected that ~ 5% of the normal tissue distribution to lie outside the CNI  $\pm 2$  range. However, the 5% were reported from one side of the distribution (CNI  $\geq 2$ ), indicating that the iterative process, while necessary to segregate tumors from normal tissue, results in an abnormally small standard deviation for the distribution of normal tissue. This seems to increase the probability of false positives two-fold (from ~2.5 % to ~5%).

Moreover, it was reported that the CNI scores of healthy volunteer voxels excluded as abnormal by the algorithm ranged between 2.2 and 5.3 while for patients with histologically proven Gliomas, the CNI of excluded voxels ranged between 2.6 and 15.0 indicating an overlapping region between the tails of the normal and diseased brain distributions lying between CNI scores of 2.6 and 5.3. This is reinforced by a simple visual inspection of a typical scatter plot as displayed in Figure 3-3, which lacks a clear distinction between normal brain population and that of disease. Although the specificity and sensitivity of the CNI delineation method could be changed by simply shifting the delineation criterion up or down, this cannot compensate for the overlapping nature of the two distributions.

To compensate for the increased probability of false positives caused by iterative linear regression and the overlap between the tumor and normal tissue populations, we suggest a modification of the tumor

delineation criteria to include a region of uncertainty covering the overlap between the two distributions. Our scatter plot would now consist of 3 regions, a normal tissue region below CNI = 2, a confirmed tumor region above a pre-determined CNI score, and an uncertainty region in between. The method we propose to define an uncertainty region that exploits the symmetry that we expect to exist in the normal population as shown in the histogram of the healthy volunteers (Figure 3-1). For example, in the GBM volunteer data shown (Figure 3-2), it was calculated that 97.5% of the points lying below the best-fit line are within a CNI scores of 0 and -4. If it is assumed that such a deviation is symmetric about the best fit line, a similar region between the CNI = 2 and the CNI = 4 lines can be considered an uncertainty region where voxels could be expected to belong to either normal tissue or tumors. This is consistent with McKnight et al. who found an overlap region between CNI scores of 2.6 and 5.3 stated earlier.<sup>12</sup> This region is shown in Figure 3-3 between the dashed and dotted lines.

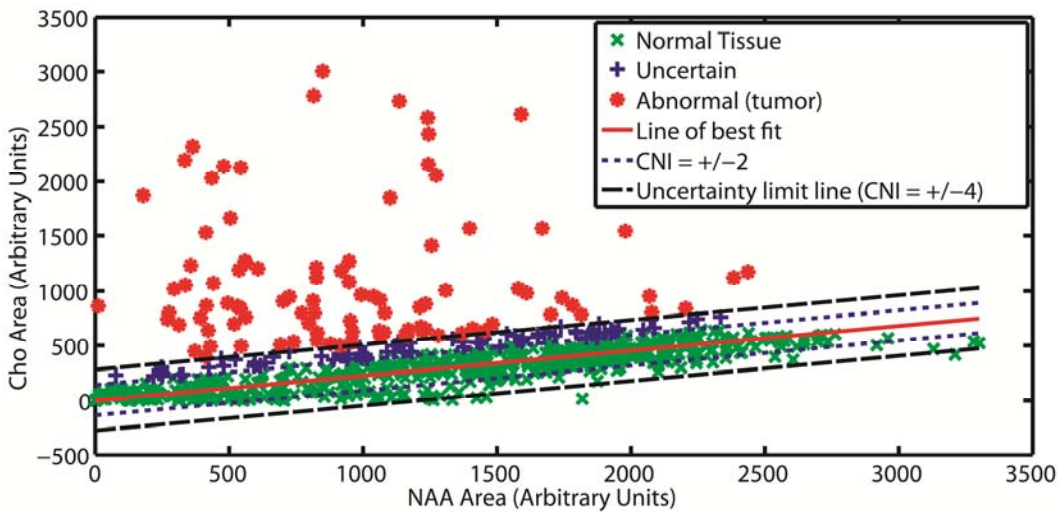


**Figure 3-3: Scatter plot of choline levels vs. NAA levels for a typical clinical GBM subject.**

In the proposed method, all voxels with CNI score  $\geq 4$  (dashed line in Fig. 3-3) would be considered tumor, while all with CNI score  $< 2$  (dotted line) have a high probability ( $>97.5\%$ ) of being normal tissue and

would be considered to be so. All voxels with  $2 \leq \text{CNI} < 4$  are of mixed probability and would be subject to further investigation.

### 3.3 Results

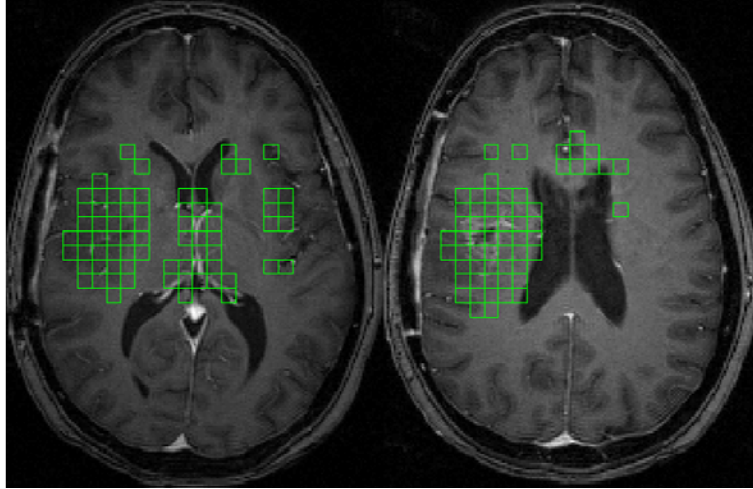


Figure 3-4: T1 weighted contrast enhanced images of adjacent MRSI slices showing voxels with  $\text{CNI} \geq 2$ .

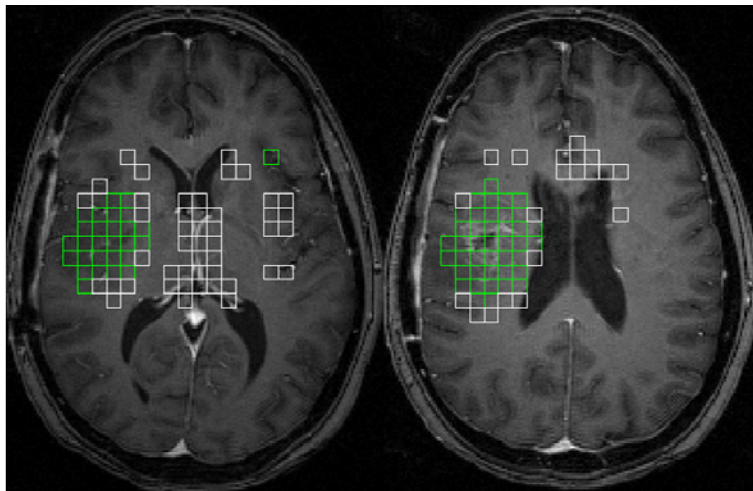


Figure 3-5: T1 weighted contrast enhanced images of adjacent MRSI slices showing voxels classified using the modified CNI method. Green voxels represent tumor, while white voxels represent voxels with mixed probability (uncertain).

Figure 3-4 and Figure 3-5 show a T1-weighted contrast enhanced image of a GBM patient's brain coupled with the abnormal MRSI voxel as delineated using the original and the modified CNI methods, respectively.

There appears to be good agreement between the two methods at the right side of the brain (image left). That region coincides with the contrast enhancement region in the T1-weighted post contrast image. The original CNI method however shows regions of metabolic abnormality at the centre of the image (ventricle region) and in the contra lateral hemisphere (patient left) whereas the modified method shows voxels at those regions belonging to the uncertainty region.

Figure 3-6 displays a selection of spectra overlapping the ventricles and surrounding voxels in this same clinical subject. Examination of this figure reveals that the metabolites in the four spectra at the top left quadrant of the highlighted voxels appear to be affected by their proximity to the ventricles. The relative level of NAA in this region appears to be less than that of neighboring normal tissue suggesting that proximity to CSF preferentially affects the detected levels of NAA. While an explanation for this result is beyond the scope of this work, it seems to contradict the conceptual expectation that CSF would not affect the relative levels of choline and NAA. Figure 3-7 shows the same effect of CSF on the relative levels of choline and NAA in a healthy volunteer (middle two columns).

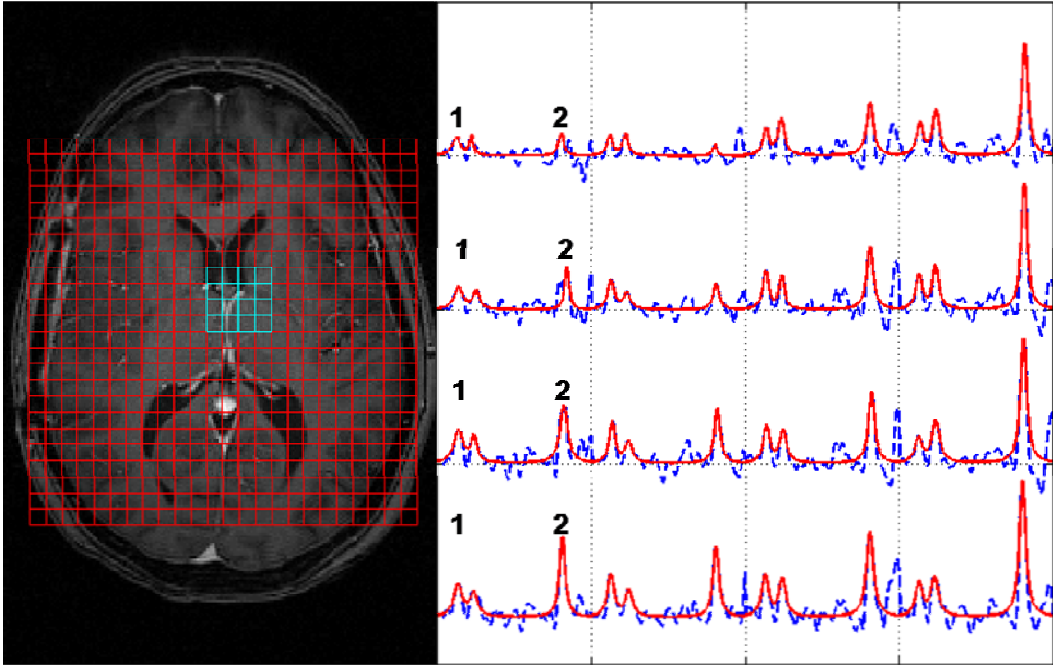


Figure 3-6: T1 weighted contrast enhanced image of a GBM patient showing spectra at different voxel locations. Peaks 1 and 2 correspond to choline and NAA, respectively.

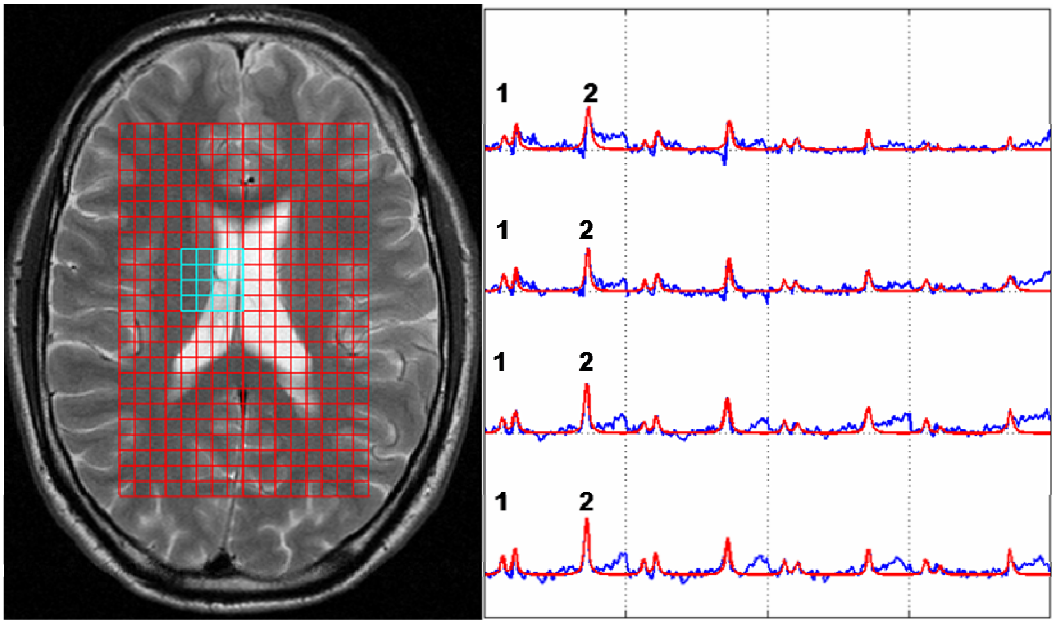


Figure 3-7: T2 weighted contrast enhanced image of a healthy volunteer showing spectra at different voxel locations. Peaks 1 and 2 correspond to choline and NAA, respectively. The middle two columns show the preferential effect of CSF on the NAA peak.

Furthermore, voxels delineated as tumor at centre of the image (Figure 3-4 and Figure 3-5) in close proximity to the ventricles were found to have a relatively low CNI score (2.8 – 4.8) compared to the tumor volume on the image left. Altogether, these voxels' relatively low CNI score, their remoteness from any voxels with large CNI score, and their proximity to the ventricles, make the classification of these voxels as tumor by the original CNI method highly suspect.

**Table 3-1: Comparison between voxels designated as abnormal (CNI  $\geq$  2) and voxels designated as uncertain (uncertainty limit > CNI  $\geq$  2) over twelve clinical subjects and three healthy volunteers.**

	<b>Clinical Subjects (n=12)</b>		<b>Healthy Volunteers (n=3)</b>	
	<b>CNI <math>\geq</math> 2</b>	<b>Uncertainty limit &gt; CNI <math>\geq</math> 2</b>	<b>CNI <math>\geq</math> 2</b>	<b>Uncertainty limit &gt; CNI <math>\geq</math> 2</b>
<b># of voxels</b>	92.8 $\pm$ 66.4	37.3 $\pm$ 27.9	54.3 $\pm$ 21.9	50.3 $\pm$ 21.7
<b>% of VOI</b>	13.5 $\pm$ 7.4	5.4 $\pm$ 3.1	7.6 $\pm$ 3.0	7.0 $\pm$ 3.0

To obtain a feel for the magnitude of abnormalities demarcated by our modified technique as uncertain, the absolute number of voxels considered uncertain and the % of the VOI they represent was compared to the total abnormalities defined by the CNI  $\geq$  2 criterion assessed over the twelve clinical volunteers and tabulated in Table 3-1. While the sample size is not large (n=12), these early results indicate that on average 5.4% of the VOI can be expected to be uncertain in clinical subjects. This number is consistent with the findings of McKnight et al.<sup>12</sup> for healthy volunteers as well as our own findings for the small healthy volunteer population shown in Table 3-1 and Figure 3-8. Moreover, the mean CNI limit for the uncertainty zone was found to be 3.7  $\pm$ 1.1 for the clinical volunteers, which is also consistent with the value found for healthy volunteers (3.4  $\pm$ 0.6). While a portion of voxels identified as uncertain in these clinical subjects was expectedly found at the outer reaches of the tumor, voxels in the uncertain region were also found at more distant

locations in close proximity to the ventricles, which reflect the trends that were discussed earlier.

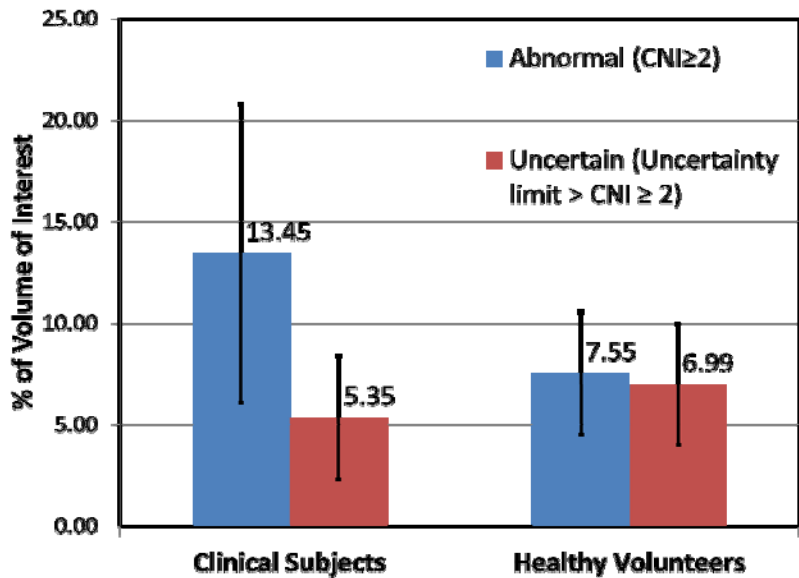


Figure 3-8: Percentage of VOI designated as abnormal and as uncertain for clinical subjects (n=12) and healthy volunteers (n=3).

### 3.4 Discussion

The original CNI method is based on two key assumptions for the statistical model: 1. that the relative levels of choline to NAA in normal brain tissue are not affected by cerebrospinal fluid present in sulci or ventricles and 2. that the variance of the choline to NAA ratio in normal brain is small compared with the difference between normal and diseased brain.<sup>12</sup> The above assumptions are generally valid in most MRSI scans. Large voxel sizes ( $\sim 1\text{cm}^3$ ) dilute differences in choline and NAA concentrations of different tissues and limit the effects of CSF on the resulting spectra. However, in this study, variations in choline and NAA concentrations due to differing tissue types and anatomical features are more readily detected due to the small voxel size ( $\sim 0.4\text{ cm}^3$ ).<sup>13</sup> Moreover, the iterative thresholding method necessary to differentiate normal tissue from tumor only serves to exaggerate the apparent homogeneity of the

normal tissue population by artificially decreasing the final standard deviations.

Furthermore, in our scans, CSF seems to cause enough effects to noticeably influence the relative levels of choline and NAA. In addition, Mcknight et al. used a relatively small volume of interest (~200 – 300 cm<sup>3</sup>) in their MRSI scans which limits the variety of normal tissue present in the sample. In studies similar to ours where greater coverage of the brain is desired, a large volume of interest (~400 cm<sup>3</sup>) widens the variety of normal tissue samples and may lead to a broadened normal tissue population. These factors combined, support the argument for the existence of mixed population region on the scatter plots and accordingly, necessitate a modification if not a revision of the original CNI model.

### **3.4.1 Correlation with Histology**

It is worth noting that the original CNI model has been validated via correlations with histology. Stereotactic biopsies were used to collect tissue samples from patients with glioma and have yielded good correlation with the CNI model.<sup>17</sup> However, it should be understood that stereotactic biopsies provide at best a histological profile of a few points in space, when only fully resection and dissection of tumor and surrounding normal tissue would provide the necessary spatio-histological profiling for correlation with a tumor delineation method like CNI.

The argument in our work should not be mistaken as a disagreement with the histological confirmation of the original CNI model. Our method relies on the statistical model and the argument that the original CNI model is quite conservative in estimating the statistical spread of CNI values of normal tissue. We suspect that even with full resection and a 2-D spatio-histological evaluation of tumor and normal tissue, and comparison with CNI values, a region of uncertainty would still exist due to underlying statistics of the population.

### **3.5 Conclusion**

The increased interest in incorporating MRSI into treatment planning has increased the need for a reliable method of delineating a biological target volume. While McKnight et al<sup>12</sup> introduced a promising user independent method for achieving such a goal; it seems that with constant improvements in MRSI sequences some of the assumptions upon which the model is built need to be revised. It is therefore necessary to introduce adjustments to the existing CNI method of tumor delineation to account for the increased detectable variation in the relative choline and NAA levels within normal tissue.

The original CNI method relied on MRSI scans with a nominal spatial resolution of 1 cm<sup>3</sup>.<sup>12</sup> At such a resolution the assumptions upon which the model was formulated were more valid; the influence of CSF on relative metabolite levels of surrounding voxels is minimal, and variations within those metabolites in normal tissue are hardly detectable. At higher resolutions, similar to the one used in our study; we have shown that those assumptions need to be reconsidered. In addition, we have noticed from the scatter plots (Figure 3-3) and McKnight et al.'s results that there exists a region of mixed population consisting of normal and tumor tissues that is not accounted for in the original CNI model. While increasing the delineation CNI threshold of tumors from the suggested 2 to 2.5 or 3, would correct for the increased variability in the normal tissue CNI scores, the mixed populations would only result in decreasing the rate of false positives and increasing the rate of false negatives.

We have therefore proposed a modification to the CNI method that would address those shortfalls. Instead of segregating the voxels into two discrete populations of normal tissue and tumor, we propose that we introduce a third region of mixed population of normal tissue and tumor. We used the normal tissue population below the best-fit line to evaluate the size of that uncertainty region. The interpretation of the voxels in the uncertainty region is at present not straightforward. Future work utilizing

additional information may hopefully lead to an educated classification of this region, which, it can be argued at present is statistically indeterminate. However, it is the assertion of this work that in order to use the choline-to-NAA ratio to its full potential in the present day radiotherapy environment, the person preparing the RT plan should be made aware of both statistical zones. In this manner, all the benefits of the statistical approach are preserved (namely lack of operator bias, and consistency between patients, scanners, centres, etc.) while clearly identifying those voxels having high tumor probability, and those voxels for which there is inherent ambiguity. This uncertainty region will indicate that a voxel is suspect, but at present its designation as an area to be treated will ultimately rely on the planner's experience and information gleaned from other sequences and/or modalities. The authors see that the real strength of the CNI methods thus lies in its statistical user-independent approach to analyzing MRSI scans, while technological limitations prevent it from becoming a reliable tumor delineation technique for the time being.

## References

1. A. Pirzkall, X. Li, J. Oh, S. Chang, M. S. Berger, D. A. Larson, L. J. Verhey, W. P. Dillon and S. J. Nelson, "3D MRSI for resected high-grade gliomas before RT: tumor extent according to metabolic activity in relation to MRI," *Int. J. Radiat. Oncol. Biol. Phys.* **59** (1), 126-137 (2004).
2. M. Law, S. Yang, H. Wang, J. S. Babb, G. Johnson, S. Cha, E. A. Knopp and D. Zagzag, "Glioma grading: sensitivity, specificity, and predictive values of perfusion MR imaging and proton MR spectroscopic imaging compared with conventional MR imaging," *AJNR. American journal of neuroradiology* **24** (10), 1989-1998 (2003).
3. F. A. Howe, S. J. Barton, S. A. Cudlip, M. Stubbs, D. E. Saunders, M. Murphy, P. Wilkins, K. S. Opstad, V. L. Doyle, M. A. McLean, B. A. Bell and J. R. Griffiths, "Metabolite profiles of human brain tumors using quantitative in vivo <sup>1</sup>H magnetic resonance spectroscopy," *Magn. Res. Med.* **49**, 223-232 (2003).
4. A. Magalhaes, W. Godfrey, Y. Shen, J. Hu and W. Smith, "Proton magnetic resonance spectroscopy of brain tumors correlated with pathology," *Acad. Radiol.* **12**, 51-57 (2005).
5. P. B. Barker, D. O. Hearshen and M. D. Boska, "Single-voxel proton MRS of the human brain at 1.5T and 3.0T," *Magn. Reson. Med.* **45** (5), 765-769 (2001).
6. P. R. Luyten, A. J. Marien, W. Heindel, P. H. van Gerwen, K. Herholz, J. A. den Hollander, G. Friedmann and W. D. Heiss, "Metabolic imaging of patients with intracranial tumors: H-1 MR spectroscopic imaging and PET," *Radiology* **176** (3), 791-799 (1990).
7. S. J. Nelson, E. Graves, A. Pirzkall, X. Li, A. A. Chan, D. B. Vigneron and T. R. McKnight, "In Vivo molecular imaging for planning radiation therapy of gliomas: an application of <sup>1</sup>H MRSI," *J. Magn. Reson. Imaging* **16** (4), 464-476 (2002).
8. M. J. Fulham, A. Bizzi, M. J. Dietz, H. H. Shih, R. Raman, G. S. Sobering, J. A. Frank, A. J. Dwyer, J. R. Alger and G. D. Chiro, "Mapping of brain tumor metabolites with proton MR spectroscopic imaging: clinical relevance," *Radiology* **185** (3), 675-686 (1992).
9. H. Shimizu, T. Kumabe, T. Tominaga, T. Kayama, K. Hara, Y. Ono, K. Sato, N. Arai, S. Fujiwara and T. Yoshimoto, "Noninvasive evaluation of malignancy of brain tumors with proton MR spectroscopy," *Am. J. Neuroradiol.* **17** (4), 737-747 (1996).
10. C. M. Segebarth, D. F. Baleriaux, P. R. Luyten and J. A. den Hollander, "Detection of metabolic heterogeneity of human intracranial tumors in vivo by <sup>1</sup>H NMR spectroscopic imaging," *Magn. Reson. Med.* **13** (1), 62-76 (1990).
11. M. C. Preul, Z. Caramanos, D. L. Collins, J. G. Villemure, R. Leblanc, A. Olivier, R. Pokrupa and D. L. Arnold, "Accurate, noninvasive diagnosis of human brain tumors by using proton magnetic resonance spectroscopy," *Nat. Med.* **2** (3), 323-325 (1996).

12. T. R. McKnight, S. M. Noworolski, D. B. Vigneron and S. J. Nelson, "An automated technique for the quantitative assessment of 3D-MRSI data from patients with glioma," *Journal of magnetic resonance imaging : JMRI* **13** (2), 167-177 (2001).
13. D. Xu, A. P. Chen, C. Cunningham, J. A. Osorio, S. J. Nelson and D. B. Vigneron, "Spectroscopic imaging of the brain with phased-array coils at 3.0T," *J. Magn. Reson. Imaging* **24** (1), 69-74 (2006).
14. D. G. Nishimura, *Principles of Magnetic Resonance Imaging*. (Stanford University, 1996).
15. A. A. Heikal, K. Wachowicz, S. D. Thomas and B. G. Fallone, "A phantom to assess the accuracy of tumor delineation using MRSI," *Radiology and Oncology* **42** (4), 232-239 (2008).
16. S. Mierisova and M. Ala-Korpela, "MR spectroscopy quantitation: a review of frequency domain methods," *NMR Biomed* **14** (4), 247-259 (2001).
17. T. R. McKnight, M. H. von dem Bussche, D. B. Vigneron, Y. Lu, M. S. Berger, M. W. McDermott, W. P. Dillon, E. E. Graves, A. Pirzkall and S. J. Nelson, "Histopathological validation of a three-dimensional magnetic resonance spectroscopy index as a predictor of tumor presence," *J Neurosurg* **97**, 794-802 (2002).

## Chapter Four

### 4 MTF behaviour of compressed sensing MR spectroscopic imaging<sup>†</sup>

---

#### 4.1 Introduction

Magnetic resonance spectroscopic imaging (MRSI) is a technique that exploits the chemical shift phenomenon with spatial encoding to produce a distribution of spatially dependent spectra that can yield information regarding the biochemistry of the underlying tissue. As discussed in Chapter Three, the bio-chemical information provided by MRSI has often been used to assess tumor activity, particularly in the brain and the prostate, and to enhance targeting and assessment of conventional radiation-therapy and stereotactic radio-surgery.<sup>1-5</sup> Commonly used MRSI techniques generally do not employ read-out frequency encoding and instead rely entirely on phase encoding for spatial encoding. As a result, MRSI is known to suffer from long scan times. For example, a typical clinical 3-D brain Point Resolved Spectroscopy (PRESS) sequence takes about 14 minutes ( $12 \times 12 \times 4$  voxels, FOV  $12 \times 12 \times 4$  cm<sup>3</sup>, TR = 1500 ms) to complete while achieving only 1 cm<sup>3</sup> voxels. This limits the maximum resolution and field-of-view achievable in a clinically reasonable time frame. Reduction in scan time can clearly be achieved by acquiring fewer k-space samples, but if acquired in the traditional regularly-sampled Cartesian manner this implies either sacrifice in terms of lower resolution, or a risk of coherent aliasing artifacts (fold-over). Two prominent techniques used to circumvent these effects are parallel imaging and more recently Compressed Sensing (CS). While there is much interest in both techniques for implementation in MRSI, they

---

<sup>†</sup> A. A. Heikal, K. Wachowicz and B. G. Fallone, "MTF behavior of compressed sensing MR spectroscopic imaging," *Med Phys* **40** (5), 052302 (2013).

are essentially independent processes.<sup>6-8</sup> This work focuses on CS as applied to MRSI and the potential costs and benefits of such a technique.

Compressed sensing has been a topic of interest in MRI circles and conferences in recent years. Compressed Sensing MRI (CS-MRI) offers the ability to accelerate MRI sequences while suffering minimal artifacts compared to conventional fast MRI techniques.<sup>9</sup> CS-MRI exploits the inherent sparsity of MRI images and incoherent artifacts of pseudo-random sub-Nyquist sampling of k-space combined with nonlinear reconstruction to produce MRI images. It can be used to either increase the resolution with no penalty in scan time, or reducing the scan time while suffering minimum aliasing (coherent) artifacts.<sup>9</sup> Consequently, compressed sensing is potentially an invaluable tool to overcome some of the shortcomings of conventional MRSI. In this work we adopt the compressed sensing technique to accelerate a clinically relevant 2-D Point RESolved Spectroscopy (PRESS) sequence. While compressed sensing has been applied to hyper-polarized <sup>13</sup>C MRSI sequences,<sup>10, 11</sup> little has been reported in its application to <sup>1</sup>H spectroscopic imaging potentially due to the relatively high signal-to-noise ratio requirements of compressed sensing.<sup>6, 7, 10</sup> CS-MRSI can be used as an acceleration tool to decrease scan times while maintaining acceptable spatial definition or to enable the acquisition of higher resolution scans while minimizing the associated time penalty.<sup>9</sup>

The modulation transfer function (MTF) is valuable image quality metric that is closely related to the point spread function and quantitatively defines the system's spatial frequency response and spatial resolution. The MTF quantifies how sharp transitions such as brain matter/cerebrospinal fluid boundaries, and healthy brain/tumor boundaries are represented in in-vivo MRSI scans. While there have been extensive efforts to quantify image quality, namely spatial resolution and MTF, of MR imaging,<sup>12-14</sup> such efforts have not been mirrored in MRSI community. With typical spatial resolution an order of magnitude lower than their MRI

counterparts and the need for spectral processing and peak-fitting to yield metabolite images, there arises the need for an MTF measurement method specifically designed for MRSI purposes. Furthermore, there has not been any quantitative assessment of the MTF of CS-MRSI compared to conventional Nyquist sampled MRSI. Since most fast-imaging techniques are associated with a loss in image quality in one way or another, the user usually has to weigh costs and benefits to decide whether or not to use such a technique. That process is further complicated due to the unique nonlinear nature of compressed-sensing reconstruction. Weights for different sparsifying transforms are required for reconstruction, and the quantitative impact of these weighting choices on image quality have not yet been addressed in the literature. As a result, that cost vs. benefit analysis has largely relied on qualitative assessments.

In this work we set out to investigate the MTF behaviour of CS-MRSI with regard to CS reconstruction weights and the acquired peak signal-to-noise ratio (SNR). We developed a phantom and a method to calculate the MTF of spectroscopic imaging sequences. We used simulations to test the dependence of that function on peak SNR and reconstruction weights. Furthermore, our results were used to derive an optimized set of reconstruction parameters based on the modulation transfer function to reconstruct an experimental, clinically relevant CS-MRSI dataset.

## ***4.2 Theory***

### **4.2.1 Modulation Transfer Function**

System transfer characteristic functions are a set of functions that treat an imaging system as a black box and describe the relationship between the output of the system to the input. They rely on the system satisfying two properties: The first of these is linearity, where the output of a linear system corresponding to the sum of inputs is equal to the sum of outputs corresponding to the separate inputs, and that the multiplication of

the input by a constant multiplies the output by the same constant. The second of these is invariance, where the image of a point retains its shape as the object point is moved in the object plane. By treating a linear, shift invariant imaging system as a black box, the output corresponding to any conceivable input can be determined knowing the system transfer function.

The modulation transfer function quantifies the amount of modulation at a specific frequency that is encoded in the output image, relative to input modulation at the same frequency. In this way, not only the limiting resolution can be quantified, but the ability of an imaging protocol to represent a complete range of spatial frequencies can be quantitatively recorded. The modulation transfer function is defined as the ratio of the output modulation to the input modulation of a sinusoidal distribution of a specific spatial frequency through an imaging system. It can be defined as the ratio between output and input sinusoidal amplitudes of the same frequency, normalized to the DC scaling factor of the system (see below). In this way the zero-frequency, or DC response of the system is always normalized to unity. Although the CS algorithm can reconstruct the sub-Nyquist under-sampled k-space data with greatly reduced artifact, it is unlikely that the MTF does not suffer to some degree, especially at k-space frequencies with severe under-sampling.

$$\text{Modulation} = \frac{\text{Amplitude of sinusoid}(k)}{\text{Mean of sinusoid}} \quad (4-1)$$

and

$$\text{MTF} = \frac{\text{Output Modulation}(k)}{\text{Input Modulation}(k)} = \frac{\text{Output Sinusoidal Amplitude}(k)}{\text{Input Sinusoidal Amplitude}(k)} \times \frac{1}{\text{System DC Scaling}}$$

#### 4.2.2 Compressed Sensing

CS-MRI relies on two principles: (1) sub-Nyquist under-sampling of k-space in a manner that promotes incoherent interference rather than coherent aliasing, and (2) reconstruction of the image via a nonlinear method that exploits the sparsity of the data and promotes consistency

with the acquired under-sampled k-space points.<sup>9, 15-18</sup> Random sampling of k-space produces incoherent interference as opposed to the aliasing produced as a result of periodic under-sampling. A Monte-Carlo based algorithm can be used to assess the interference resulting from different k-space under-sampling patterns and choose the pattern that most effectively minimizes aliasing. The patterns can be generated randomly or pseudo-randomly according to a desired distribution function.<sup>9</sup>

A nonlinear method is required to reconstruct the data and is achieved by solving the following:

$$\operatorname{argmin}_m \|F_u m - y\|_2^2 + \lambda \|\Psi m\|_1 \quad (4-2)$$

where  $m$  is the desired image,  $\Psi$  is a sparsifying wavelet transform,  $\lambda$  is the reconstruction weight used for the wavelet,  $F_u$  is the under-sampled Fourier transform, and  $y$  is the acquired under-sampled k-space. The first half minimizes the  $\ell_2$  norm and hence promotes consistency between the acquired under-sampled k-space data and the corresponding points of the Fourier transform of the reconstructed image. Conversely, the second half minimizes the  $\ell_1$  norm of the sparsifying transform domain data, and hence promotes sparsity. An array of methods including iterative soft thresholding,<sup>19-21</sup> iterative reweighted least squares,<sup>22, 23</sup> interior point methods<sup>24, 25</sup> and projections onto convex sets<sup>26</sup> have been proposed to solve the above problem.

## **4.3 Materials and Methods**

### **4.3.1 Phantom**

A phantom was required to assess the spatial accuracy and resolution resulting from different MRSI sequences and reconstructions. Optimum phantom design would produce high contrast images with varying degrees of spatial detail and include a uniform normalization area. Also, it was designed such that the phantom's physical dimensions fit in a head coil. The phantom consists of an insert made up of nine  $10^\circ$  wedges

arranged in a fan-shaped semicircle separated by nine  $10^\circ$  voids. Zero-frequency is represented by a uniform region positioned below the wedges as shown in Figure 4-1. The insert is immersed in a 21 cm cylinder filled with a solution of choline (6 mM), creatine (20 mM) and acetate (25 mM). Upon taking arc profiles of the resulting axial images of the phantom, a square wave pattern can be reproduced at varying radii from the centre of the semi-circle, effectively producing a series of square waves of varying spatial frequency. The analysis region of interest shown in Figure 4-1 was defined by the limitations of clinically relevant fields-of-view for the sequence used. The dimensions of the wedges along with the need for a uniform region for normalization of the profiles at zero-frequency, limit the measurable spatial frequency range to  $\sim 0.4$  lp/cm – 6.0 lp/cm.

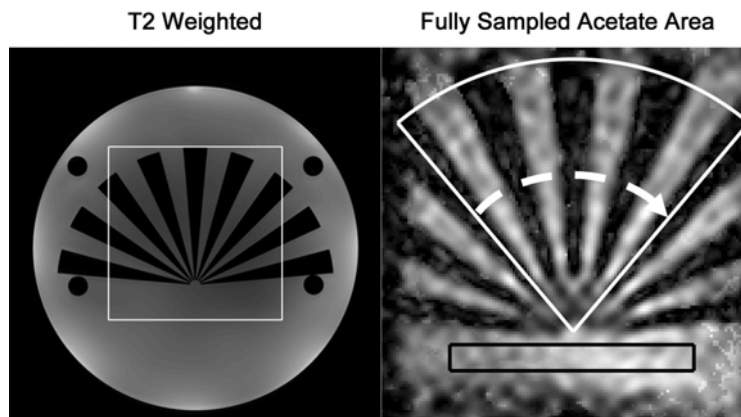


**Figure 4-1: Left: T2-weighted image of the phantom with the white box showing the MRSI field-of-view. Right: Fully sampled acetate area map. The high-lighted pie-shaped region is the region of interest used for MTF calculation. The dashed arrow signifies the location of the arc profile shown in Figure 2. The black box region is the uniform region used to normalize the arc profiles.**

### 4.3.2 MTF calculation method

As outlined earlier, arc profiles of the phantom represent a series of square waves whose frequencies are inversely proportional to the radius. These square waves were used to generate the input modulation that was used in calculating the MTF (Fig. 4-2). As the MTF will be affected by the spatial non-uniformity of the imaging coil and the asymmetry of the

randomization of the under-sampling pattern used for compressed sensing, special care was needed to account for those effects. The analysis region was limited by the clinically relevant FOV used (Fig. 4-1) which limited the span of analysis to 4 line pairs instead of the 8 available. The angular variation of k-space content (arising from both the randomization of the CS sampling as well as the variable k-space span from a lateral direction to the diagonal) would require at least two phantom orientations 90 degrees apart to obtain an average MTF response. A further two orientations were acquired in this work for every sampling pattern in order to better account for spatial coil and  $B_0$  non-uniformities. While the coil response would not have changed, by rotating the phantom we ensured that all regions of the phantom experience a variety of non-uniformity in coil response and  $B_0$ . This ensures that such effects are averaged out in our measurements. The MTF was independently calculated for each of the four angular orientations of the phantom and the resulting MTFs were then averaged to give the final MTF.

For each scan, a mathematically generated square wave response at each arc profile was calculated and transformed to Fourier space (Fig. 4-3). The MTF calculation was performed on acetate images reconstructed to a  $128 \times 128$  grid (discussed in the processing section below) and as such, the arc profiles were sampled densely enough to minimize any aliasing effects from higher order peaks onto the fundamental frequency. Given the sampling density used herein of 32 samples per line pair and the worst case scenario of a perfect square wave, comparisons of our measured response to a Fourier-series decomposition found the largest aliasing contribution to be 0.16 percent of the fundamental amplitude. The arc profiles generated from the acetate-area images were normalised to the uniform-zero-frequency region of the phantom shown in Figure 4-1 before the corresponding Fourier transforms were calculated. The ratio of the magnitude between the fundamental frequency component of the acetate-area arc profile (Fig. 4-3) to that of

the mathematically generated input square-wave was calculated resulting in the MTF at that spatial frequency and was repeated at 0.05 lp/cm increments. The procedure was repeated for 12 experimental scans (3 scans  $\times$  4 orientations) and the resulting MTFs were averaged to give the final measured modulation transfer function.

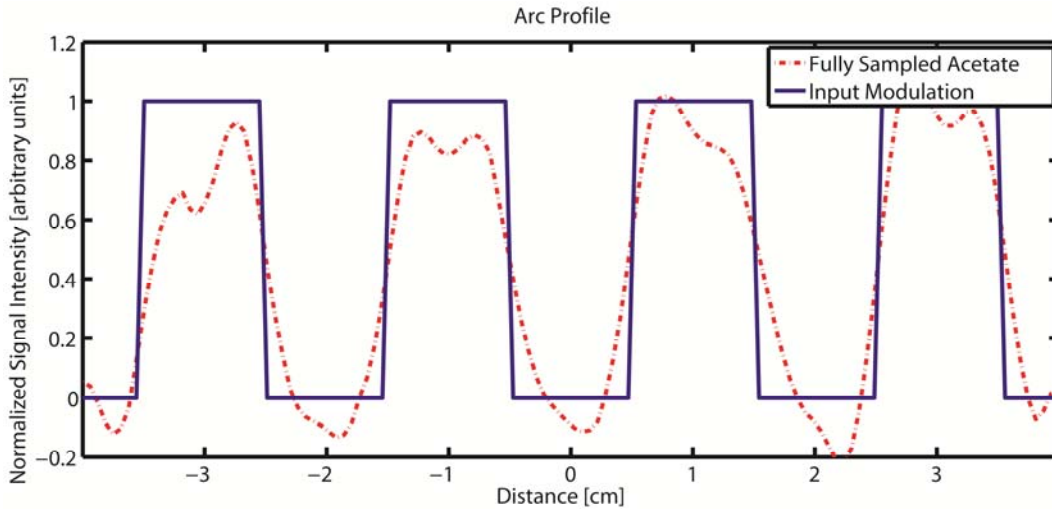


**Figure 4-2: Arc profile of the acetate-area images along with the mathematically generated input modulation square wave**

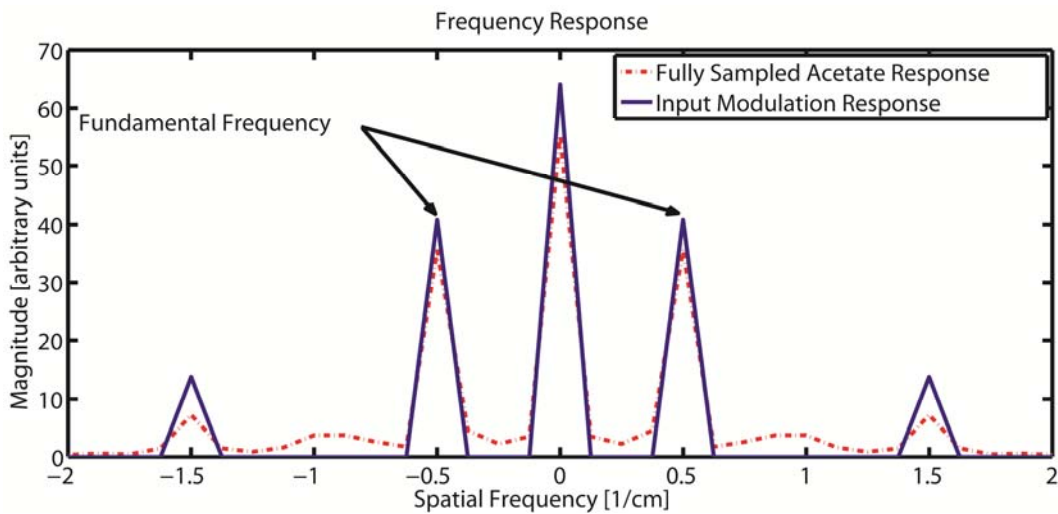


**Figure 4-3: Frequency response of the arc profile of the acetate-area image**

### 4.3.3 Sub-Nyquist Sampling

Sub-Nyquist k-space sampling patterns were generated using a Monte-Carlo based pseudo-random method in which a distribution function

forces full sampling of the centre of k-space (Fig. 4-4). This method was found to be superior to randomly sampled k-space patterns based on a uniform distribution function.<sup>9, 10</sup> The resulting optimized under-sampling pattern was generated for an acceleration factor of 4 (Fig. 4-4) where the total number of k-space samples acquired is  $\frac{1}{4}$  of that of the fully sampled  $32 \times 32$  k-space grid.

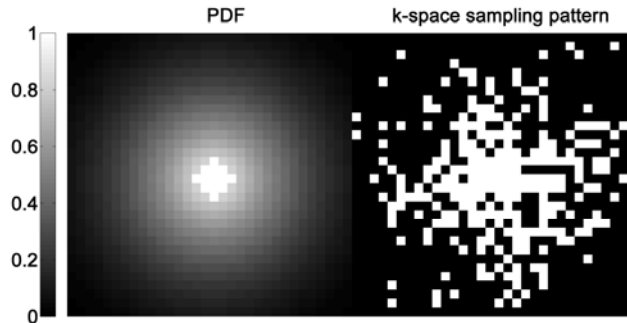


**Figure 4-4: Left: The probability distribution function used for generating the k-space sampling pattern. Right: k-space sampling pattern used for 4-fold acceleration**

#### 4.3.4 Imaging sequence

The scans were performed on a Philips Achieva 3 T MRI (Philips Healthcare, Bothell, WA) unit together with an 8 element head coil. To avoid added effects of signal combination the acquisition was performed with the coil operating in quadrature mode. A 2-D Point RESolved Spectroscopy (2-D PRESS) sequence was used to scan the phantom. A  $32 \times 32$  k-space grid was used to sample k-space covering a field of view of  $11.2 \times 11.2$  cm<sup>2</sup> and a resulting in-plane nominal spatial resolution of  $0.35 \times 0.35$  cm<sup>2</sup>. It is important to note that in the case of k-space acquisition in a square field-of-view, the limit in resolution is defined by the diagonal extent of k-space. Accordingly, while the nominal resolution for the scan described above is 0.35 cm, the limit in resolution is 0.25 cm due to a diagonal k-space extent that is 40% larger than the lateral k-space extent. The slice thickness was set to 0.7 cm. Half-echo acquisition was performed over 512 ms where 1024 time points were sampled at a rate of

2000 Hz. The repetition and echo times were set to 1400 ms and 32 ms, respectively.

Three scans were acquired with the phantom oriented in each of four angular orientations with respect to the centre wedge; at  $0^\circ$ ,  $90^\circ$ ,  $180^\circ$  and  $270^\circ$ . The raw data was arranged in a 3 dimensional matrix corresponding to  $k_y$ - $k_x$ - $t$ , where  $k_y$  and  $k_x$  are the k-space coordinates in the y and x directions, respectively, and  $t$  is the acquisition time. This data was later subsampled using the optimized undersampling pattern to generate the compressed sensing datasets.

#### **4.3.5 Simulated data**

A two-dimensional model of the phantom was created in Matlab (The MathWorks, Natick, MA) based on the geometry and the spectral quality acquired from the 2D-PRESS scan of the phantom above ( $32 \times 32$  pixels with nominal resolution of  $3.5 \times 3.5 \text{ mm}^2$ ). The simulated peak height was chosen together with the addition of noise to achieve a similar peak SNR to that of the acquired data. Peak SNR is the ratio of the magnitude of the acetate peak to the standard deviation of the noise in a spectrum acquired from the uniform region of the phantom. In other simulations, spectral noise was varied to simulate different peak SNR's while maintaining the same peak heights. Simulations were repeated five times for each mean peak SNR value. The simulated k-space data was arranged in a  $k_y$ - $k_x$ - $t$  matrix similar to that of the experimental phantom scans. As the simulations do not suffer any spatial non-uniformity from an imaging system, MTF calculations for the simulations only considered 2 orientations of the phantom; at  $0^\circ$  and  $90^\circ$ .

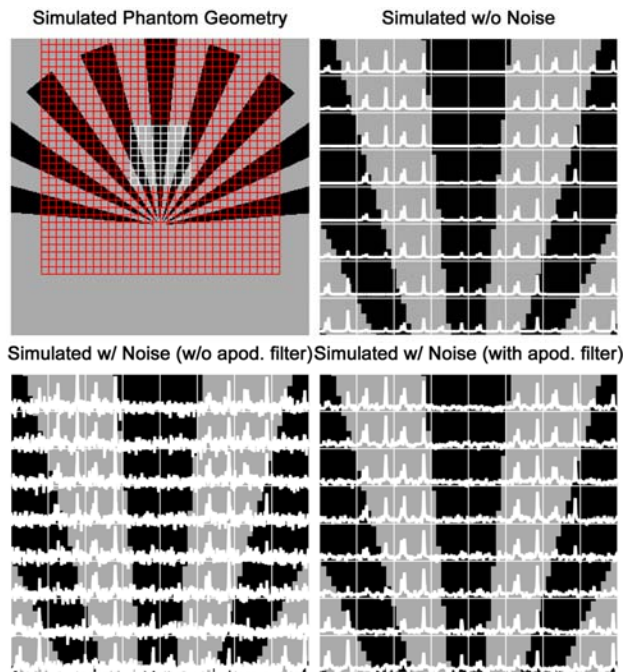


Figure 4-5: Simulated phantom geometry along with the simulated MRSI grid showing metabolite peaks with and without noise

#### 4.3.6 Reconstruction

It was found empirically that applying a wavelet transform to a spectrum in the frequency domain produces a sparser representation than applying the transform to the time domain FID signal. A 3-D wavelet transform was applied on a sample dataset and reconstructed using only the highest 25% of the 3-D wavelet coefficients. A root mean square error (rmse) of 0.29% was observed between the original and the reconstructed datasets when applying the wavelet transform to the spectrum in the frequency domain versus an rmse of 0.44% when applying the transform to the time domain FID signal. Accordingly, a 1-D Fourier transform is applied to the CS-MRSI data in the t-direction to transform it to  $k_x$ - $k_y$ -f. Subsequently, a 3-D wavelet transform in the x-y-f dimensions serves as the sparsifying transform for the reconstruction.

The CS reconstruction algorithm is based on an iterative nonlinear conjugate gradient method with a line search function is used in the Matlab code provided by M. Lustig

(<http://www.msrl.stanford.edu/~mlustig/software>).<sup>9</sup> The code was modified in-house to work with MR spectroscopic imaging data. The nature of the CS reconstruction requires optimization of the weights for the sparsifying transforms to balance the data fidelity and sparsity constraints. Previously, this was achieved empirically and is thought to have little impact on reconstruction accuracy.<sup>9-11</sup> Using the simulated datasets, we tested the effect of different reconstruction weights on the MTF of the resulting acetate images.

Also, due to the nonlinearity of the CS reconstruction process, peak SNR may have an impact on the MTF of the reconstructed metabolite images, as opposed to linear systems where the two are fundamentally independent. Accordingly, we repeated the same experiment for datasets with different peak SNRs to investigate the combined effect of reconstruction weights and peak SNR on MTF.

For every experimental CS-MRSI dataset, two Nyquist sampled datasets were reconstructed using the traditional 2D inverse Fourier transform: a fully sampled 32x32 dataset and a Nyquist-sampled low-resolution dataset consisting of the same number of k-space samples as the sub-Nyquist-sampled compressed sensing dataset. All datasets were reconstructed to a 128x128 grid using zero-padding in k-space prior to spectral processing and peak-fitting.

#### **4.3.7 Processing**

The x-y-f data resulting from the CS nonlinear reconstruction was inverse-Fourier transformed back to x-y-t domain to undergo the same processing steps as the Nyquist sampled data. Post reconstruction, all datasets were subjected to the same spectral processing and peak fitting steps as follows:

Firstly, in the x-y-t domain, additional water suppression was achieved by convolving the time domain FID with a 7.5 ms Gaussian and subtracting the result of the convolution from the FID. This is equivalent to

applying a high-pass filter that selectively suppresses the remaining water signal. Furthermore, a half-gaussian apodizing filter was applied to the water-suppressed FID to reduce spectral noise.

Secondly, the apodized x-y-t data was then forward Fourier transformed to x-y-f where it was phase corrected and further analyzed using software that calculates the area under different metabolite peaks.<sup>27</sup> The peak fitting algorithm fits a sum of complex Lorentzian functions to the acquired spectra.<sup>28</sup> The resulting Lorentzian parameters were used to analytically calculate the area under the choline, creatine and acetate peaks from each voxel. The acetate-area map was used to calculate the MTF of its respective scan. Normalized root-mean-square error (nrmse) was calculated for CS reconstructions in comparison to the fully sampled acetate images. The nrmse is defined as the ratio of the root-mean-square error between the CS reconstruction and the fully sampled acetate image, to the root-mean-square of the fully sampled acetate image.

#### **4.4 Results and Discussion**

Like MRI, resolution in MRSI is dependent on the extent (width) of sampled k-space. In the case of k-space acquisition in a square field-of-view, the limit in resolution is defined by the diagonal extent of k-space. For example, in the case of the fully sampled 32 k-space points wide dataset described above, the lateral voxel size is 0.35 cm (corresponding to a measurable resolution of  $\sim 1.4$  lp/cm), however the diagonal extent of k-space is  $\sim 40\%$  larger, resulting in a limit resolution of 0.25 cm ( $\sim 2.0$  lp/cm). Because k-space is not amplitude modulated by filtering or from signal decay (as would occur with multi-echo approaches) during an unaccelerated 2-D PRESS acquisition, the MTF is expected to be relatively constant from 0 lp/cm to the lateral frequency cutoff (1.4 lp/cm). Due to the square field-of-view acquisition, not all orientations of k-space are sampled between the circular and the diagonal cut-off frequencies (1.4 and 2.0 lp/cm, respectively). Accordingly, the MTF gradually declines to

zero between 1.4 lp/cm and 2.0 lp/cm. Similarly, for the low-resolution scans (shown in Figure 8), the cutoff frequency is expected to be 1.0 lp/cm rather than 0.7 lp/cm as a four-fold reduction in scan time corresponds to a two-fold reduction in sampled k-space in each direction. Figure 4-6 shows that our fully-sampled MTFs agree in general form with the theoretically expected Nyquist-sampled MTF shapes explained above.

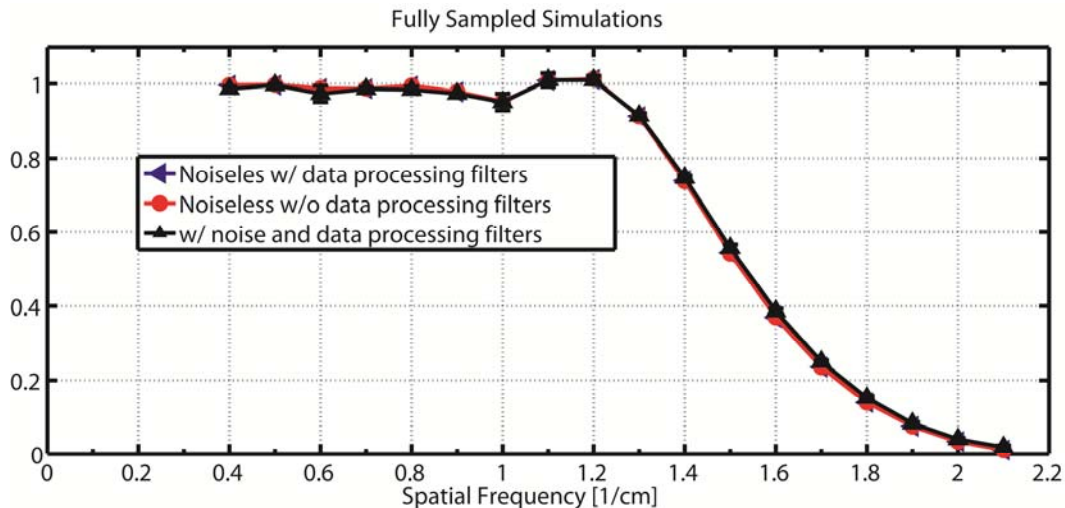


**Figure 4-6: MTF of fully sampled simulations and showing the effect of processing filters and noise on the MTF.**

Figure 4-6 shows that on noiseless simulations, the data processing filters used had no effect on the MTF. This is expected as no filters were applied in the k-space domain. Moreover, when noise was added to simulations, the average response is seen to converge to the noiseless case. The lack of a k-space apodizing filter leads to Gibbs ringing artifacts in the spatial domain caused by the discontinuity in k-space when zero-padding from 32×32 to 128×128. These artifacts lead to an unexpected dip in the MTF at 1.0 lp/cm and peaks at 1.1 lp/cm and 1.2 lp/cm due to destructive and constructive interference, respectively. A k-space apodizing filter (e.g Butterworth filter) would decrease the Gibbs ringing but it would also greatly influence the shape of the MTF especially at the cutoff frequencies. We chose to tolerate the ringing to preserve the cutoff frequencies.

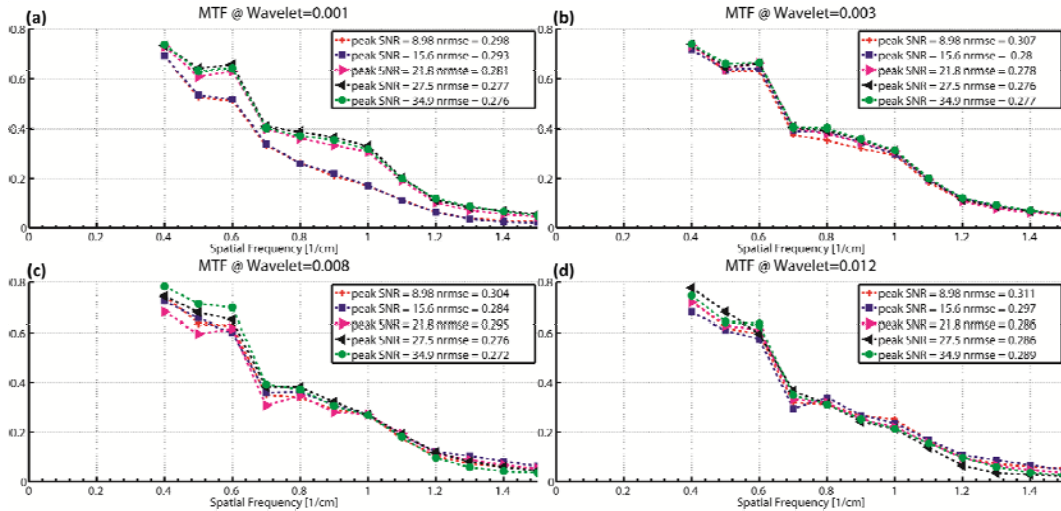


**Figure 4-7: Calculated MTFs for CS reconstructions from simulation using varying weights for different peak SNRs**

For the MTF to be treated as a system characteristic function, an assumption of system linearity is required for the function to fully describe the frequency response of the system. However, the nonlinearity of CS reconstruction might lead to differences in system response based on peak SNR inputs. Figure 4-7 shows the mean MTFs for CS reconstruction of the simulated phantom spectra using different reconstruction weights for simulations with different peak SNRs. These MTFs calculations were repeated with a number of different noise sets to average out noise perturbations on the shape of the MTF.

The frequency response of the system was very robust across a wide range of SNRs when a reconstruction weighting of 0.003 was utilized (Fig. 4-7b). The robustness of the frequency responses with differing noise levels suggest that for this particular reconstruction weight, the system can be considered linear, and the frequency response curves can be considered as the characteristic MTF of the system. However, the implementation of other reconstruction weights was seen to generate sub-optimal response curves at some of the SNR levels tested. This implies that when selecting reconstruction weights, it is important to consider the response over a range of SNRs that one expects to encounter. An ideal

weighting will generate both an optimal and consistent response over this range. If this step is not taken, a satisfactory response curve obtained at a high signal level may not be applicable for a lower one, and visa-versa (Fig. 4-7a).

Furthermore, while using different reconstruction weights at times led to varying MTFs, this was not necessarily reflected in the nrmse of the reconstructions. This suggests that using nrmse as the sole reconstruction-goodness parameter can lead to reconstructions with a sub-optimal and potentially nonlinear response..

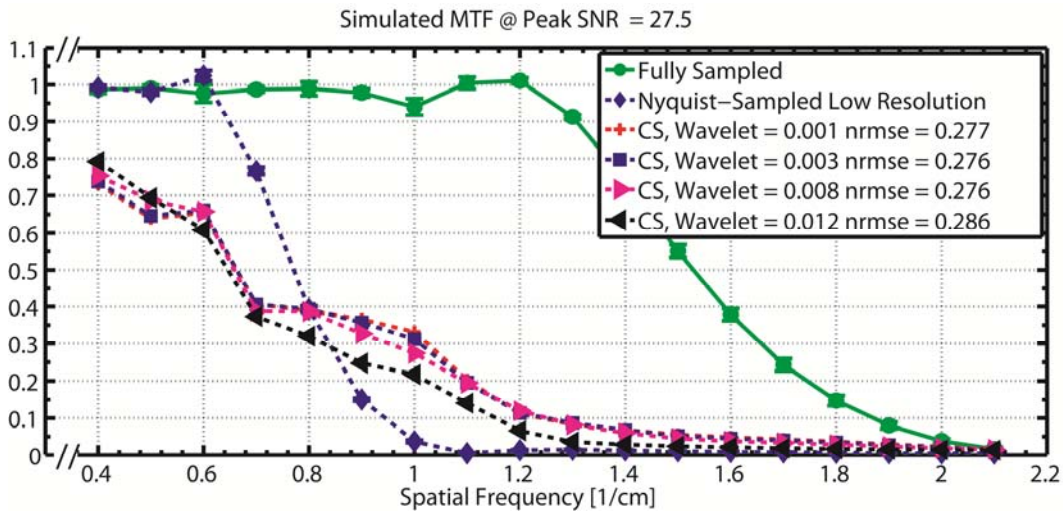


**Figure 4-8: Calculated MTFs for simulated CS reconstructions using varying weights for a peak SNR value similar to that of the physical phantom**

The average peak SNR of the spectra acquired from the 2-D experimental scan of the phantom was found to be 24.9. Figure 4-8 shows the varying MTFs for a set of simulated data with peak SNR of 27.5 similar to that of the experimental data. From the figure it is clear that at that peak SNR the best MTFs are produced when the reconstruction weights used are 0.001, 0.003 and 0.008.

It is most likely that in the case of disease that the peak SNR for a specific scan would be unknown, hence, it is important that the chosen reconstruction weight is robust across a wide peak SNR range. Accordingly, due to the robustness of the 0.003 weight across the peak

SNR range (Fig. 4-7b), it appears that this reconstruction weight is the optimum for reconstructing the experimental scans.

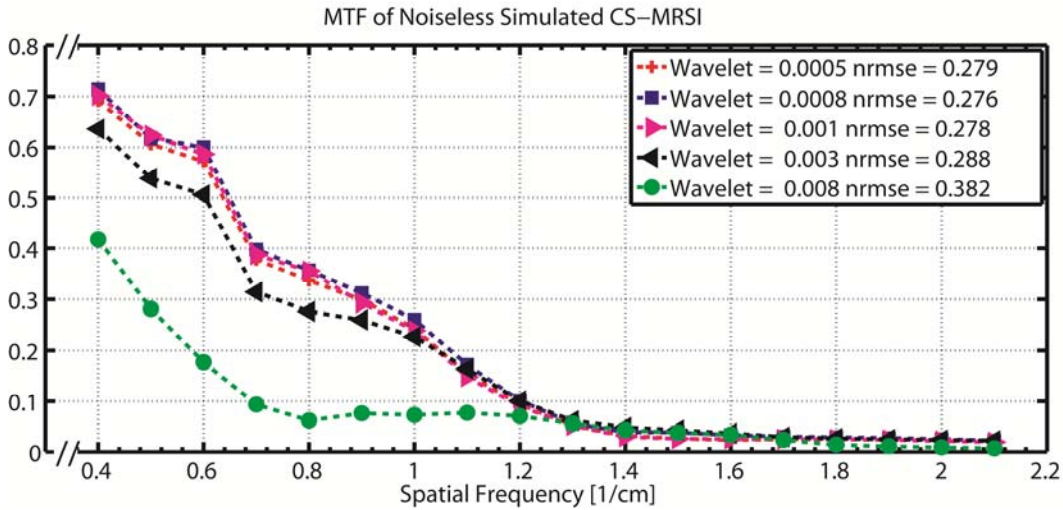


**Figure 4-9: MTF of noiseless simulations using different CS reconstruction weights**

Similar to Figure 4-8, it was found that the MTF of CS for noiseless simulated datasets also depended on the reconstruction weight used, as shown in Figure 4-9. It is important to note that although the resulting MTFs are very similar between the noiseless and noise-added scenarios (Fig. 4-9 and 4-8, respectively), the optimum reconstruction weights are different. This again suggests that peak SNR plays a major role in determining the optimum reconstruction weight.

MTFs corresponding to all reconstruction weights tested were plotted for each peak SNR (not shown). The reconstruction weight yielding the best MTF at each peak SNR was chosen and the corresponding MTF plotted in Figure 4-10. It is clear from Figure 4-10 that all the resulting MTFs agree within error. This suggests that although the reconstruction process is nonlinear with respect to reconstruction weights, the optimum reconstruction seems to yield an MTF that is independent of peak SNR.

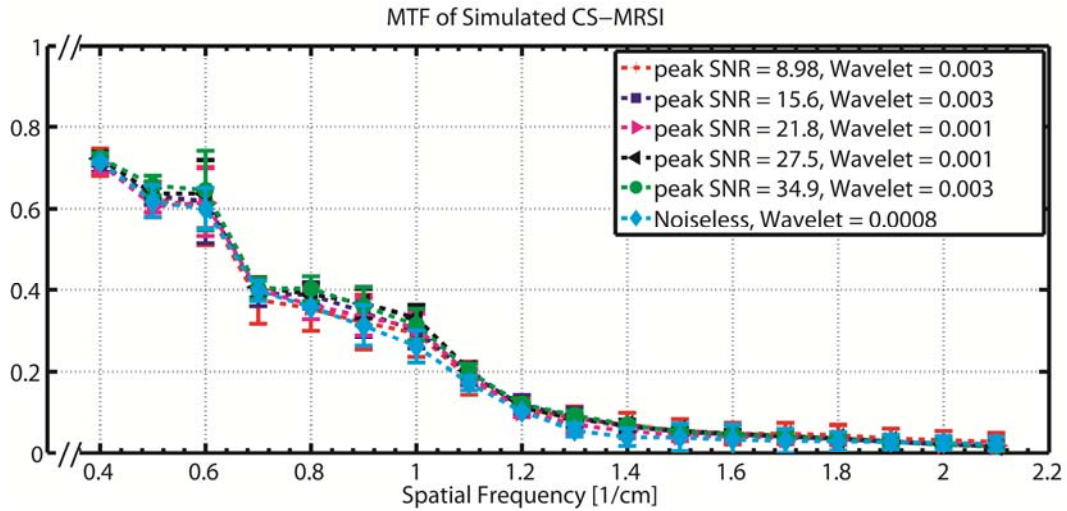


Figure 4-10: The best MTF achievable for CS-MRSI over a wide range of peak SNR

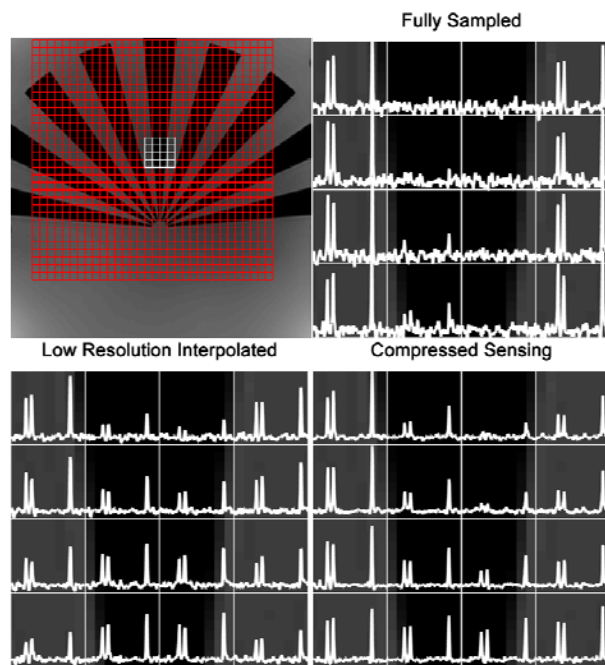
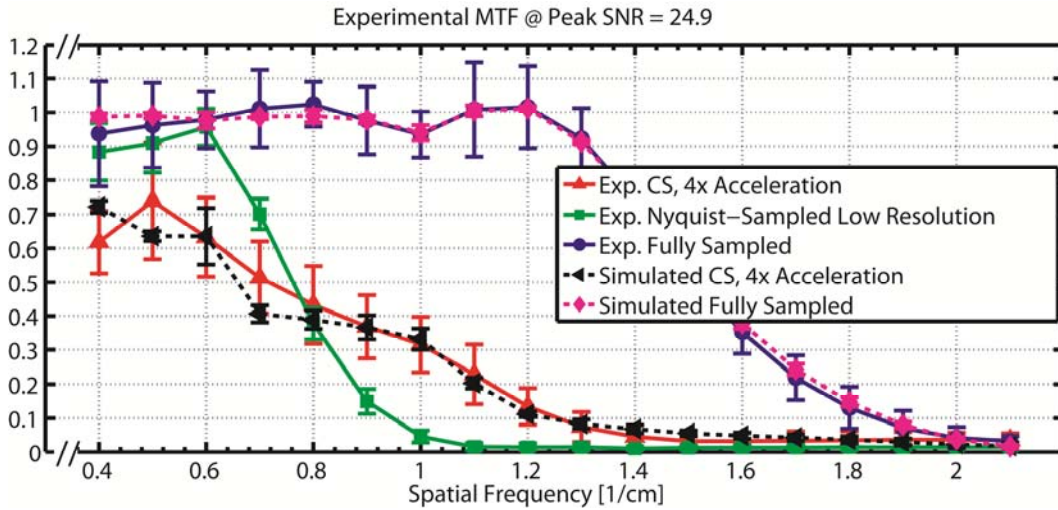


Figure 4-11: Reconstructed MRSI spectra overlaid on T2-weighted images of the phantom

The optimized reconstruction weight of 0.003 was used to reconstruct a four-fold accelerated compressed sensing MRSI scan of the phantom described earlier. Figure 4-11 shows the spectra resulting from compressed sensing MRSI scan compared to a fully-sampled scan and an equivalent Nyquist sampled low-resolution scan.

Compared to the fully-sampled scan, both the low-resolution and the CS spectra suffer from partial volume artifacts in the form of visible signal in dark regions of the phantom. However, there is a visible reduction of noise in the CS spectra due to the application of the wavelet transform in the reconstruction. Moreover, the top row shows better correlation with the geometry of the underlying phantom for the low-resolution spectra than the CS ones. Both CS and the low-resolution spectra appear to be very similar in the second row from the top. In the bottom two rows (corresponding to a higher resolution region), the CS spectra show better correlation to the phantom geometry than the low-resolution ones.



**Figure 4-12: MTF of the experimental CS dataset compared to equivalent Nyquist-sampled low-resolution and the fully-sampled Fourier reconstructions**

Figure 4-12 shows the calculated MTF for a four-fold accelerated CS-MRSI scan of the phantom. There is good agreement between the MTF calculated for simulations and that of the experimental datasets. The ringing artifacts evidenced in the MTF of the noiseless datasets discussed earlier (Fig. 4-6) are visible in the experimental measurements (Fig. 4-12). The magnitude of the artifact ( $<0.1$ ) is smaller than the error bars associated with the experimental measurements and significantly smaller than the drop in MTF associated with CS, indicating that the aforementioned ringing artifacts would have limited effect on the results below.

Expectedly, the resolution at 0.1 MTF decreases for both the CS (1.25 lp/cm) and the low-resolution (0.95 lp/cm) datasets compared to the fully sampled dataset (1.85 lp/cm), a decrease of 32.4% and 48.6%, respectively. CS-MRSI maintains a higher MTF between 0.8 lp/cm and 1.4 lp/cm leading to higher effective resolution than the equivalent low-resolution dataset. However, the increase in effective resolution comes at the cost of low-resolution response. Between 0.4 and 0.8 lp/cm, the CS scans have a visibly lower MTF compared to their Nyquist-sampled low-resolution counterparts which is also apparent in Figure 8. The lessened low-resolution performance is attributed to the pseudo-random under-sampling of k-space inherent to the CS method and the inability of CS to accurately fill in the missing k-space data as expected. In the case of the Nyquist-sampled low-resolution scans, 256 (16x16) points are used to periodically sample k-space, while in the case of CS-MRSI, the same number of points are used to sample a k-space area four times larger. That results in a reduction in sampling density of k-space at the aforementioned spatial frequencies, which by extension may translate to the observed reduction in signal response at those frequencies.

#### **4.5 Conclusions**

In this work we have investigated MTF behaviour of compressed-sensing MRSI reconstruction, including the specific effects of CS reconstruction weights and peak SNR on MTF. While CS reconstruction is nonlinear by definition, our results show that when proper care is taken in choosing the reconstruction weighting factor, the resulting MTFs were found to be robust with regards to peak SNR. Furthermore and importantly for practical application of this technique, the optimal weighting factor was found to be dependent on peak SNR. Accordingly, prior knowledge of the expected peak SNR range is important to yield optimum MTF response of the CS reconstruction.

The phantom-MTF technique proposed in this work provides an excellent quantitative measure of the performance of MRSI sequences that to the best of our knowledge is the first attempt to quantify the MTF of MRSI metabolite images. We have successfully used it to compare CS-MRSI to fully sampled conventional MRSI. Our quantitative method of evaluating the MTF for MRSI along with simulations and a purposefully designed phantom enabled us to optimize the reconstruction weight to produce the best possible MTFs across a range of peak SNRs (8.98 – 34.9). We used the optimized weight to successfully reconstruct an experimentally acquired CS dataset using a clinically relevant  $^1\text{H}$  MRSI sequence. Our method was able to quantify an average decrease of 32.4% in spatial resolution in the CS-MRSI scans at 0.1 MTF compared to a loss of 48.6% for the equivalent Nyquist-sampled low-resolution scans. Moreover, we were also able to quantify the cost of the increase in resolution, with CS-MRSI showing decreased low-resolution response compared to the equivalent low-resolution datasets.

## References

1. P. R. Luyten, A. J. Marien, W. Heindel, P. H. van Gerwen, K. Herholz, J. A. den Hollander, G. Friedmann and W. D. Heiss, "Metabolic imaging of patients with intracranial tumors: H-1 MR spectroscopic imaging and PET," *Radiology* **176** (3), 791-799 (1990).
2. M. Law, S. Yang, H. Wang, J. S. Babb, G. Johnson, S. Cha, E. A. Knopp and D. Zagzag, "Glioma grading: sensitivity, specificity, and predictive values of perfusion MR imaging and proton MR spectroscopic imaging compared with conventional MR imaging," *AJNR. American journal of neuroradiology* **24** (10), 1989-1998 (2003).
3. F. A. Howe, S. J. Barton, S. A. Cudlip, M. Stubbs, D. E. Saunders, M. Murphy, P. Wilkins, K. S. Opstad, V. L. Doyle, M. A. McLean, B. A. Bell and J. R. Griffiths, "Metabolite profiles of human brain tumors using quantitative in vivo 1H magnetic resonance spectroscopy," *Magn. Res. Med.* **49**, 223-232 (2003).
4. A. Magalhaes, W. Godfrey, Y. Shen, J. Hu and W. Smith, "Proton magnetic resonance spectroscopy of brain tumors correlated with pathology," *Acad. Radiol.* **12**, 51-57 (2005).
5. A. Pirzkall, X. Li, J. Oh, S. Chang, M. S. Berger, D. A. Larson, L. J. Verhey, W. P. Dillon and S. J. Nelson, "3D MRSI for resected high-grade gliomas before RT: tumor extent according to metabolic activity in relation to MRI," *Int. J. Radiat. Oncol. Biol. Phys.* **59** (1), 126-137 (2004).
6. J. K. Furuyama, N. E. Wilson, B. L. Burns, R. Nagarajan, D. J. Margolis and M. A. Thomas, "Application of compressed sensing to multidimensional spectroscopic imaging in human prostate," *Magn Res Med* **67**, 1499-1505 (2012).
7. S. Geethanath, H.-M. Baek, S. K. Ganji, Y. Ding, E. A. Maher, R. D. Sims, C. Choi, M. A. Lewis and V. D. Kodibagkar, "Compressive sensing could accelerate 1H MR metabolic imaging in the clinic," *Radiology* **262** (3) (2012).
8. J. Sánchez-González, J. Tsao, U. Dydak, M. Desco, P. Boesiger and K. P. Pruessmann, "Minimum-norm reconstruction for sensitivity-encoded magnetic resonance spectroscopic imaging," *Magn Reson Med* **55** (2), 287-295 (2006).
9. M. Lustig, D. Donoho and J. M. Pauly, "Sparse MRI: The application of compressed sensing for rapid MR imaging," *Magn Reson Med* **58** (6), 1182-1195 (2007).
10. S. Hu, M. Lustig, A. Balakrishnan, P. E. Larson, R. Bok, J. Kurhanewicz, S. J. Nelson, A. Goga, J. M. Pauly and D. B. Vigneron, "3D compressed sensing for highly accelerated hyperpolarized (13)C MRSI with in vivo applications to transgenic mouse models of cancer," *Magn Reson Med* **63** (2), 312-321 (2010).
11. S. Hu, M. Lustig, A. P. Chen, J. Crane, A. Kerr, D. A. Kelley, R. Hurd, J. Kurhanewicz, S. J. Nelson, J. M. Pauly and D. B. Vigneron, "Compressed sensing for resolution enhancement of hyperpolarized 13C flyback 3D-MRSI," *J Magn Reson* **192** (2), 258-264 (2008).
12. S. M. Mohapatra, J. D. Turley, J. R. Prince, J. C. Blechinger and D. A. Wilson, "Transfer function measurement and analysis for a magnetic resonance imager," *Med Phys* **18** (6), 1141-1144 (1991).
13. M. D. Robson, J. C. Gore and R. T. Constable, "Measurement of the point spread function using constanttime imaging," *Magn. Reson. Med.* **38** (5), 733-740 (1997).

14. M. C. Steckner, D. J. Drost and F. S. Prato, "Computing the modulation transfer function of a magnetic resonance imager," *Med. Phys.* **21** (3), 483-489 (1994).
15. E. J. Candes, J. Romberg and T. Tao, "Robust uncertainty principles: Exact signal reconstruction from highly incomplete frequency information," *IEEE Trans Inform Theory* **52** (2), 489-509 (2006).
16. D. L. Donoho, "Compressed sensing," *IEEE Trans. Inform. Theory* **52**, 1289-1306 (2006).
17. A. S. Stern, D. L. Donoho and J. C. Hoch, "NMR data processing using iterative thresholding and minimum l1-norm reconstruction," *J Magn Reson* **188**, 295-300 (2007).
18. Y. Tsaig and D. L. Donoho, "Extensions of compressed sensing," *Signal Processing* **86** (3), 549-571 (2006).
19. I. Daubechies, M. Defrise and C. D. Mol, "An iterative thresholding algorithm for linear inverse problems with a sparsity constraint," *Commun. Pure. Appl. Math.* **57**, 1413-1457 (2004).
20. M. Elad, B. Matalon and M. Zibulevsky, "Coordinate and subspace optimization methods for linear least squares with non-quadratic regularization," *J. Appl. Comput. Harmonic. Anal.* **23**, 346-367 (2007).
21. J. L. Starck, M. Elad and D. Donoho, "Image decomposition via the combination of sparse representation and variational approach," *IEEE Trans. Image. Process.* **14**, 1570-1582 (2005).
22. D. Donoho, M. Elad and V. Temlyakov, "Stable recovery of sparse overcomplete representations in the presence of noise," *IEEE Trans Inform Theory* **52**, 6-18 (2006).
23. M. Lustig, J. M. Santos, D. L. Donoho and J. M. Pauly, "k-t SPARSE: High frame rate dynamic MRI exploiting spatio-temporal sparsity," *Proc. of 14th Annual Meeting of ISMRM*, 2420 (2006).
24. S. Chen, D. Donoho and M. Saunders, "Atomic decomposition by basis pursuit," *SIAM J. Sci. Comput.* **20** (1), 33-61 (1999).
25. S. J. Kim, K. Koh, M. Lustig and S. Boyd, presented at the *Proc. of IEEE International Conference on Image Processing (ICIP)*, San Antonio, 2007.
26. E. Candes and J. Romberg, "Signal recovery from random projections," *P Soc Photo-Opt Ins* **5674** (5674), 76-86 (2005).
27. A. A. Heikal, K. Wachowicz, S. D. Thomas and B. G. Fallone, "A phantom to assess the accuracy of tumor delineation using MRSI," *Radiology and Oncology* **42** (4), 232-239 (2008).
28. S. Mierisova and M. Ala-Korpela, "MR spectroscopy quantitation: a review of frequency domain methods," *NMR Biomed* **14** (4), 247-259 (2001).

## Chapter Five

# 5 Effect of the k-space Sampling Pattern on the MTF of Compressed Sensing MRSI

---

### 5.1 Introduction

As introduced in Chapter Four, Compressed sensing (CS) is an acceleration technique that has appeared relatively recently in the field of MR, and more recently has been applied to MRS imaging.<sup>1-6</sup> When applied to MRI, CS exploits the incoherent nature of aliasing artifacts associated with randomized sub-Nyquist sampling of k-space rather than the coherent aliasing (fold-over) artifacts associated with periodic sub-Nyquist sampling. The recovery of the original image relies on the sparsity of the MRI images in a transform domain to suppress the incoherent aliasing artifacts and reconstruct the original image using a constrained nonlinear algorithm. Since little-to-no time efficiency can be gained from randomly sub-sampling a frequency-encoded trajectory, this sub-sampling is generally achieved by selectively omitting random phase-encoding steps.

Because of its typical reliance on nested phase-encoding loops for spatial definition, spectroscopic imaging is a prime candidate for acceleration through this technique. For example, a typical clinical 3-D brain Point RESolved Spectroscopy (PRESS) MRSI sequence (12×12×4 voxels, FOV 12×12×4 cm<sup>3</sup>, TR = 1500 ms) takes about 14 minutes to complete while achieving only 1 cm<sup>3</sup> voxels. This limits the maximum resolution and field-of-view achievable in a clinically reasonable time frame. Two-fold undersampling of each in-plane direction (four-fold overall) would therefore allow for either decreasing the scan time to ~ 3 minutes or increasing the in-plane nominal resolution to ~ 0.25 cm<sup>2</sup>. Consequently, CS-MRSI can be used as an acceleration tool to decrease the scan time while maintaining acceptable spatial definition or to enable

the acquisition of higher resolution scans while minimizing the associated time penalty.<sup>1-8</sup>

It is reasonable to expect that most acceleration schemes will have some undesired consequences on image quality. The nature of such sacrifices depends on the acceleration technique employed, and the degree of acceleration. The user usually weighs costs and benefits to decide whether or not to use such technique and the degree of acceleration. In the case of compressed sensing, the literature has usually relied on qualitative comparisons between compressed sensing reconstructions and their Nyquist sampled counterparts. While those comparisons show subtle differences in high-detail resolution between compressed sensing and Nyquist sampled images, the lack of a quantitative measure of those measurements may lead some to misjudge compressed sensing as a lossless acceleration technique.<sup>1-3</sup> One metric that has been repeatedly used in the literature is the normalized root mean square error (nRMSE) between a compressed sensed image and its full Nyquist sampled counterpart.<sup>2-4</sup> While the nRMSE score provides a measure of the fidelity of the compressed sensing reconstruction, it fails to provide any information about any possible losses in local resolution.

The MTF is a metric that quantifies the amount of modulation at a specific frequency that is encoded in the output image, relative to input modulation at the same frequency. The MTF is normalized to 1 at zero frequency (uniform signal). For example, if an MRI were to image an object with a sinusoidally varying intensity, and the output image was only able to replicate the signal with an amplitude 80% that of the input (relative to the transfer of uniform signal), the MTF would record a response of 0.8 at that frequency. In this way, not only the limiting resolution can be quantified, but the ability of an imaging protocol to represent a complete range of spatial frequencies can be quantitatively recorded. In that sense, quantifying the MTF would provide an accurate measure of the effect compressed sensing has on representing the spatial frequencies present

in the imaged object. Chapter Four introduced a method to quantify the MTF of MRSI scans and to provide a quantitative measure of the cost and benefit of CS-MRSI.<sup>6</sup>

With random sub-Nyquist sampling of k-space, aliasing artifacts become incoherent, and can be suppressed by a constrained optimization. However, this undersampling has been found to have an insidious consequence. As shown in Chapter Four, MTFs of the CS metabolite images were found to be distinctly different from their corresponding full Nyquist sampled counterparts.<sup>6</sup> It was also shown that the CS-MTF response was greatly reduced at high spatial frequencies which correspond to severely undersampled regions of k-space. Reduced high spatial frequency response corresponds to a widening of the point spread function, effectively reducing the spatial resolution of the CS reconstruction to a value far lower than the expected nominal value of the full Nyquist sampled images. This effect would be hard to detect on clinical subjects and phantoms not designed for MTF quantification.

Random sampling of k-space leads to variations in the density of the k-space sampling at various spatial frequencies compared to conventional Nyquist sampling which we suspect is the main factor affecting the MTF. In this work we set out to investigate the MTF behaviour of CS-MRSI with regard to different k-space sampling patterns. We suspect that there is a correlation between the manner in which k-space is being sampled (i.e. k-space sampling density of the CS sampling patterns) and the MTF of the resulting CS reconstruction. Comparing CS-MRSI and Nyquist sampled  $32 \times 32$  reconstructions with identical TR/TE times and the absence of amplitude modulation or filtering of k-space, one would expect the Nyquist sampled  $32 \times 32$  MTF to define the upper limit of the available response at each spatial frequency. Accordingly, CS-MTF can be considered a subset of the Nyquist sampled  $32 \times 32$  response. Given that the difference between the Nyquist sampled response and the compressed sensing response is mainly the sub-Nyquist sampling of k-

space, we are proposing the relationship between the Nyquist sampled 32×32 MTF and the CS-MTF to be explained as follows:

$$\frac{CS - MTF(k)}{NS - MTF(k)} = \frac{\# \text{ of } CS \text{ } k - \text{ space samples } (k)}{\# \text{ of } NS \text{ } k - \text{ space samples } (k)}$$

*or*

$$CS - MTF(k) = \textit{sampling ratio} (k) \times NS - MTF(k)$$
(5-1)

where *NS-MTF* corresponds to the Nyquist sampled 32×32 simulations and the *sampling ratio* is defined as the ratio of number the k-space samples acquired in the CS sampling pattern to those acquired in a full Nyquist sampled 32×32 grid, at each spatial-frequency (*k*).

If true, Eq. 5-1 would provide the ability to theoretically predict the CS-MTF (and by extension the point spread function) based on the manner of k-space sampling without having to measure the individual MTF response of each CS reconstruction. This would yield the benefit of knowing the likely cost of applying CS, at least in terms of resolution, before a scan is implemented. It would allow for the design of appropriate under-sampling schemes (tailored to the imaging requirements at hand) without the need for time-consuming trial and error.

In this work we relied on simulations of the detail phantom described in the literature to calculate the MTF of a spectroscopic imaging sequence and test the dependence of that function on the sampling ratio of the sub-Nyquist k-space sampling pattern used in compressed sensing.<sup>6</sup> Using the knowledge of the relationship between the sampling ratio and MTF, we explored means to improve the predictability and potential customization of the MTF of CS-MRSI by modifying the algorithm responsible for generating the k-space sampling patterns used in compressed sensing.

## **5.2 Materials and Methods**

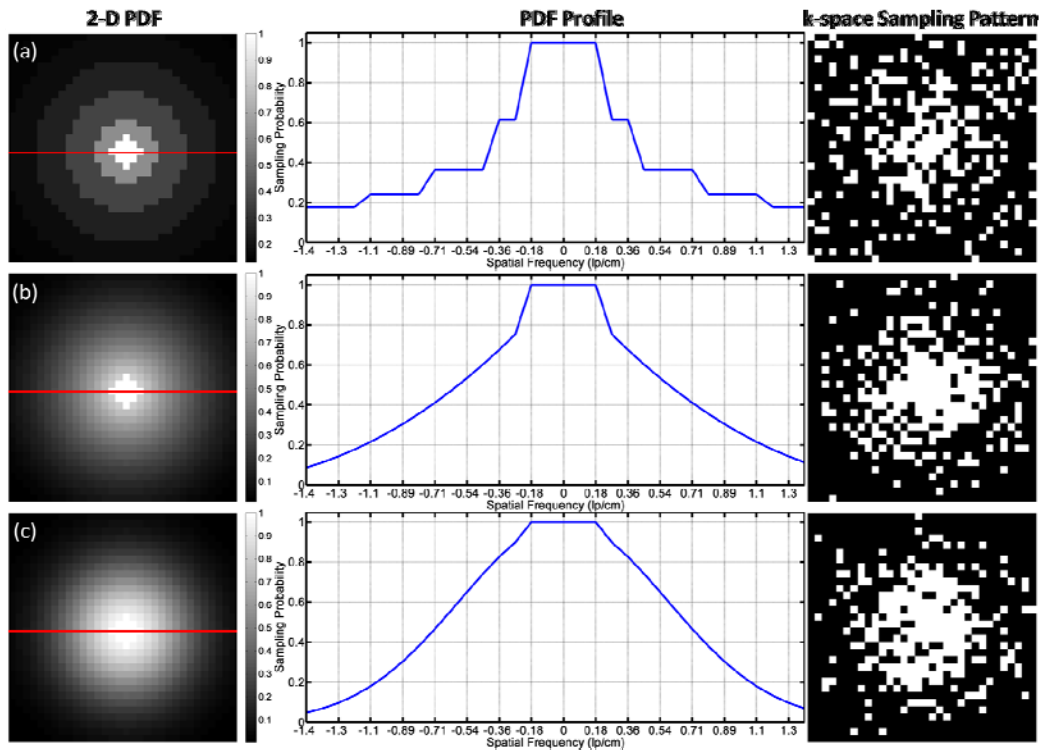
Compressed Sensing MRI relies on two principles: (1) sub-Nyquist under-sampling of k-space in a manner that promotes incoherent interference rather than coherent aliasing, and (2) reconstruction of the

image via a nonlinear method that exploits the sparsity of the data in the transform domain and promotes consistency with the acquired under-sampled k-space points.<sup>1, 7, 9-12</sup>

Sub-Nyquist k-space sampling patterns are generated using a Monte-Carlo based pseudo-random method in which a probability distribution function (PDF) guides the sampling probability of different regions in k-space.<sup>1, 3</sup> The algorithm assesses the interference in the transform domain resulting from different sub-Nyquist k-space sampling patterns (generated randomly based on the PDF) and chooses the pattern that most effectively minimizes aliasing over a predetermined number of iterations (10000). The acceptance criterion for the final selected sampling pattern is solely based on minimizing the interference caused by sub-Nyquist sampling. This can lead to cases where the resulting sampling pattern is very effective in reducing interference but whose sampling ratio is different from the desired PDF. We shall refer to patterns generated using this algorithm as density unconstrained patterns. For this work, k-space sampling patterns were generated where the total number of k-space samples acquired is  $\frac{1}{4}$  of that of the fully sampled  $32 \times 32$  k-space grid (Fig.5-1) achieving an acceleration factor of 4 in scan times. Three sets of ten k-space sampling patterns were generated using a step,  $1/r^2$ , and half-Gaussian PDFs, respectively. All PDFs fully sample an inner radius of 2 k-space points to improve SNR.<sup>1, 3</sup>

The afore-mentioned algorithm was then modified to produce k-space sampling patterns whose sampling ratios are constrained to adhere to the desired PDFs. As before, it is an iterative process where the final selection criterion for a sampling pattern is based on minimizing the interference caused by sub-Nyquist sampling. However, the resulting k-space sampling patterns are optimized for both reduction in interference and adherence to the PDF. For the purpose of this paper we shall refer to k-space sampling patterns produced by the modified algorithm as PDF-constrained patterns. Three sets of ten PDF-constrained patterns were

generated using a step,  $1/r^2$ , and half Gaussian PDFs, respectively, and a fully sampled radius of 2 k-space points.



**Figure 5-1: Examples of the probability distribution function (PDF) (left), a corresponding profile through the centre of k-space (middle) and an example of a corresponding k-space sampling pattern (right) for (a) a step, (b) a  $1/r^2$ , and (c) a half-Gaussian PDF.**

### 5.2.1 Phantom

A two-dimensional model of the phantom used in Chapter Four (Section 4.3.1) was created in Matlab (The MathWorks, Natick, MA) based on the geometry and the spectral quality acquired from a 2D-PRESS scan of the phantom (32×32 pixels with nominal resolution of 3.5×3.5 mm<sup>2</sup>, TR/TE of 1400/32 ms, half-echo acquisition over 512 ms, sampling rate of 2000 Hz). First, a T2-weighted 512×512 scan of the phantom was acquired over the same field-of-view as the MRSI scan. The T2-weighted image was segmented into a 2-D mask (0 for the wedges and 1 for signal). The mask was 2-D Fourier transformed to a 2-D k-space representation of the phantom geometry. Second, the central 32×32 pixels of the k-space

were multiplied by a sum of decaying exponentials representing the time-domain FID corresponding to the Choline, Creatine and Acetate signals, resulting in the three dimensional k-space  $(k_x, k_y, t)$  simulation of the phantom. The simulated peak heights were chosen together with the addition of noise to achieve a similar peak SNR to that of a previously acquired dataset. Peak SNR is the ratio of the magnitude of the acetate peak to the standard deviation of the noise in a spectrum acquired from the uniform region of the phantom. Three simulations (noise sets) were generated with mean peak-SNR of 27.8.

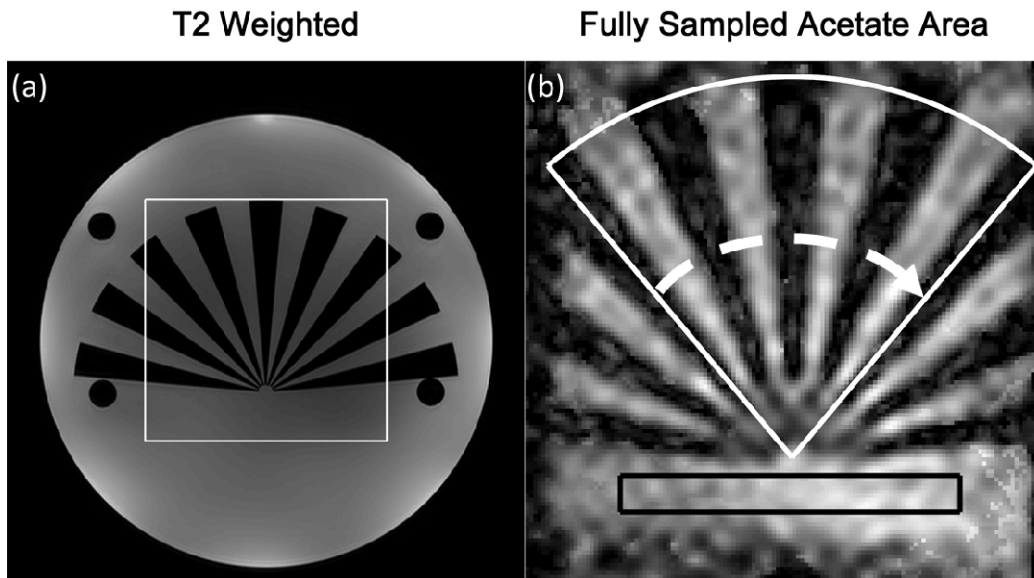


**Figure 5-2: (a) T2-weighted image of the phantom with the white box showing the MRSI field-of-view. (b) Fully sampled acetate area map. The high-lighted pie-shaped region the region of interest used for MTF calculation. The dashed arrow signifies the location of the arc profile shown in figure 2. The black box region is the uniform region used to normalize the arc profiles.**

### 5.2.2 Reconstruction

The CS reconstruction algorithm is based on an iterative nonlinear conjugate gradient method with a line search function used in the Matlab code provided by M. Lustig (<http://www.msrl.stanford.edu/~mlustig/software>). The code was modified in-house to work with MR spectroscopic imaging data. A

3-D wavelet transform in the x-y-f dimensions serves as the sparsifying transform for the 3-D reconstruction. The nature of the CS reconstruction requires optimization of the weights for the sparsifying transforms to balance the data fidelity and sparsity constraints. The optimum weight for CS reconstruction was empirically determined to be 0.001. Each phantom simulation was reconstructed using 10 k-space sampling patterns for each PDF, yielding a total of 30 (3 simulations  $\times$  10 sampling patterns/PDF) reconstructions per PDF. To account for asymmetries in the k-space sampling patterns, the CS reconstructions were repeated with the phantom orientation rotated 90° in-plane using the same un-rotated sampling patterns.<sup>6</sup> This yielded a total of 60 reconstructions for each probability distribution function.

For every CS-MRSI dataset, two Nyquist sampled datasets were reconstructed using the traditional 2D inverse Fourier transform: a fully sampled 32 $\times$ 32 dataset and a time-equivalent Nyquist-sampled low-resolution 16 $\times$ 16 dataset consisting of the same number of k-space samples as the sub-Nyquist-sampled compressed sensing dataset. All datasets were reconstructed to a 128 $\times$ 128 grid using zero-padding in k-space prior to spectral processing and peak-fitting.

### **5.2.3 Processing**

The x-y-f data resulting from the CS non-linear reconstruction was inverse-Fourier transformed back to x-y-t domain to undergo the same processing steps as the Nyquist sampled data. Post reconstruction, all datasets were subjected to the following spectral processing and peak fitting steps: First, in the x-y-t domain, additional water suppression was achieved by convolving the time domain FID with a 7.5 ms Gaussian and subtracting the result of the convolution from the FID. This is equivalent to applying a high-pass filter that selectively suppresses the remaining water

signal. Furthermore, a half-gaussian apodizing filter was applied to the water-suppressed FID to reduce spectral noise.

Second, the apodized x-y-t data was then forward Fourier transformed to x-y-f where it was phase corrected and further analyzed using software that calculates the area under different metabolite peaks.<sup>13</sup> The peak fitting algorithm fits a sum of complex Lorentzian functions to the acquired spectra.<sup>14</sup> The resulting Lorentzian parameters were used to analytically calculate the area under the choline, creatine and acetate peaks from each voxel. The acetate-area map was used to calculate the MTF of its respective simulation.

#### **5.2.4 MTF calculation method**

The MTF calculation method explained in Section 4.3.2 was used to calculate the MTFs used in this work.<sup>6</sup> MTF calculations were performed for 60 CS-MRSI reconstructions (2 orientations × 3 simulations × 10 sampling patterns/PDF) and the resulting MTFs were averaged to give the final measured modulation transfer function.

#### **5.2.5 Sampling ratio**

To calculate the sampling ratio, k-space was first binned into 0.09 lp/cm (1 pixel-wide) radial bins from the centre of k-space. Second, the sampling ratio was calculated by dividing the number of k-space samples defined in the sampling pattern by the number of samples available at each spatial-frequency bin. The product of the sampling ratio and the Nyquist sampled 32×32 MTF (RHS of Eq. 5-1) will henceforth be referred to as the sampling-modulated NS-MTF.

### **5.3 Results and Discussion**

As discussed in Section 4.4, the Nyquist sampled MTF is expected to be relatively constant from 0 lp/cm to the lateral frequency cut-off (1.4 lp/cm) and gradually declining to zero between 1.4 lp/cm and 2.0 lp/cm (the diagonal cut-off frequency). Similarly, for the low-resolution scans, the

cut-off frequency is expected to be 1.0 lp/cm rather than 0.7 lp/cm as a four-fold reduction in scan time corresponds to a two-fold reduction in sampled k-space in each direction. Often, to reduce scan times, the corners of k-space beyond the lateral cut-off frequencies are not acquired. In that case, no orientation of k-space is sampled between the lateral and diagonal cut-off frequencies; as a result, the MTF can be expected to drop suddenly after the lateral cut-off frequency due to the lack of spatial-frequency information beyond this threshold. In this work it was decided to investigate the full square cartesian k-space domain and its more complicated MTF. Theory established here will flow nicely to the radially-symmetric circular k-space domain.

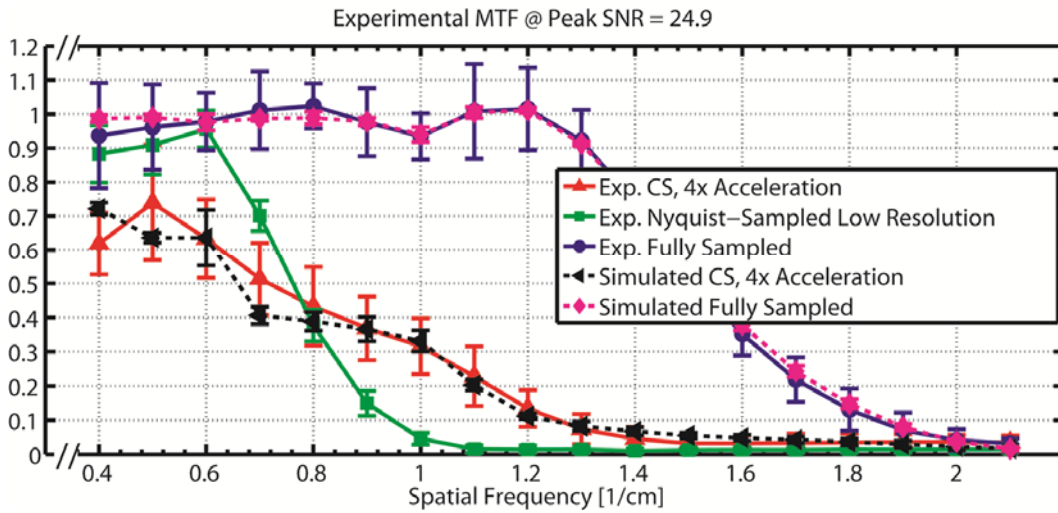


**Figure 5-3: MTFs of experimental CS dataset compared to the equivalent Nyquist-sampled low-resolution (16×16) and the fully-sampled (32×32) Fourier reconstructions. MTFs of simulations are shown for comparison.**

Figure 5-3, shows a comparison between high-resolution Nyquist sampled reconstructions, 4× compressed sensing reconstructions using the 1/2 sampling pattern, and the time equivalent Nyquist sampled low-resolution reconstructions. The figure shows that the MTFs of the Nyquist sampled datasets agree in general form with the theoretically expected MTF shapes explained above. Furthermore, there is good agreement between the MTFs calculated for simulations and those of the

experimental datasets. This is in agreement with what has been demonstrated in the literature.<sup>6</sup>

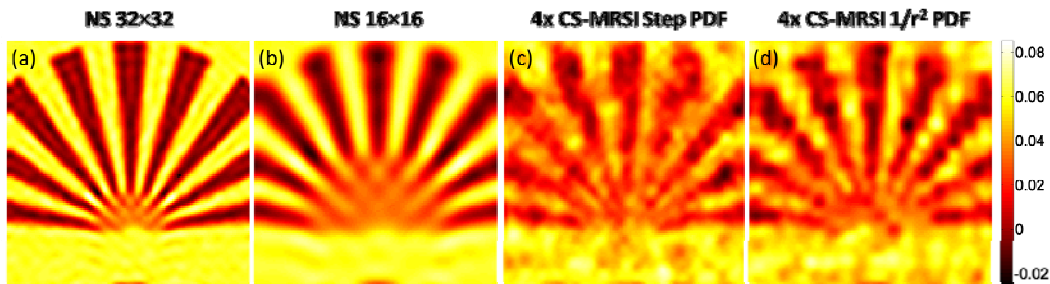


**Figure 5-4: Simulated acetate area reconstructions for (a) full Nyquist sampling (32×32), (b) CS equivalent low-resolution sampling (16×16), (c) 4× CS-MRSI using a step PDF, and (d) 4× CS-MRSI using a 1/r<sup>2</sup> PDF.**

Figure 5-4 shows compressed sensing acetate area reconstructions using the step PDF and the  $1/r^2$  PDF compared to the Nyquist sampled 32×32 simulations and the compressed sensing equivalent Nyquist sampled 16×16 simulations. The apparent negative peak areas are a result of the Gibbs ringing artifacts in the spatial domain. The Gibbs ringing is caused by the discontinuity in k-space when zero-padding from 32×32 to 128×128. These artifacts lead to destructive and constructive interference, and the apparent negative peaks. That effect could have been mitigated by applying a k-space apodizing filter (e.g Butterworth filter) to decrease the Gibbs ringing but it would have also greatly influenced the shape of the MTF especially at the cutoff frequencies. We chose to tolerate the ringing to preserve the cutoff frequencies.

From Fig. 5-4, the step PDF reconstruction shows a modest improvement in high-detail resolution (closer to the centre of the fan) but at the cost of compromised details at the low-detail region (outer parts of the fan). The  $1/r^2$  PDF reconstruction appears to recover low-detail response but the high-detail does not appear as well resolved as the step-function reconstruction.

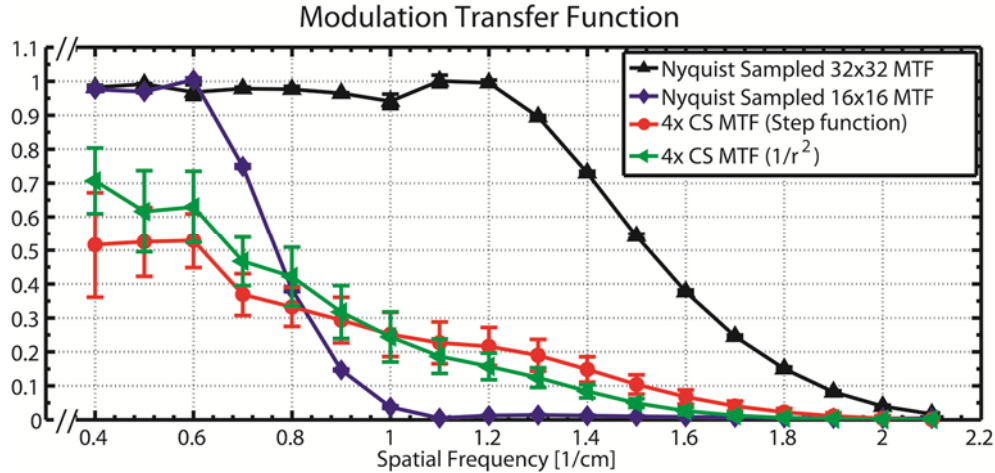


**Figure 5-5: MTFs of acetate area simulations of full Nyquist sampled (32×32) reconstructions, CS equivalent low-resolution (16×16) reconstructions, 4× CS-MRSI using a step PDF and a 1/r<sup>2</sup> PDF**

Figure 5-5 shows the MTFs resulting from the reconstruction shown in Fig. 5-4 averaged over ten sampling patterns per PDF compared to their corresponding Nyquist sampled simulations. Figure 5-5, also shows that the tested CS-MRSI maintains a higher MTF between 0.8 lp/cm and 1.4 lp/cm indicating a higher effective resolution than the time equivalent low-resolution dataset. However, the increase in effective resolution comes at the cost of low-frequency response. Between 0.4 and 0.8 lp/cm, the CS reconstructions have a visibly lower MTF compared to their Nyquist-sampled low-resolution counterparts as noticed in Fig 5-4. The diminished low-frequency performance is attributed to the weighted random under-sampling of k-space inherent to the CS method and the inability of CS to accurately fill in the missing k-space data as expected. In the case of the Nyquist-sampled low-resolution scans, 256 (16×16) points are used to periodically sample k-space, while in the case of CS-MRSI, the same number of points are used to sample a k-space area four times larger. This results in a reduction in sampling density of k-space at the aforementioned spatial frequencies, which by extension translates to the observed reduction in signal response at those frequencies.

While the general trends are similar between the CS-MTFs, there is a distinct difference between both sets of MTFs especially between 0.4 lp/cm – 0.8 lp/cm where the  $1/r^2$  PDF reconstructions exhibit higher response. Conversely, the step PDF reconstructions exhibit higher response between 1.0 – 1.8 lp/cm which is consistent with the observations in Figure 5-4. The discrepancy in response between the two CS dataset is most likely caused by the different PDF used to generate the k-space sampling patterns. Figure 5-1 shows the difference in k-space sampling patterns resulting from different PDFs. It is clear that the step functions result in sampling patterns that tend to sample the farther extents of k-space more densely than the  $1/r^2$  function. On the other hand  $1/r^2$  function results in denser sampling close to the centre of k-space. This reflects the same trends shown in the CS-MTFs above, where the step-function MTF shows slightly higher response at higher spatial frequencies (far k-space) while the  $1/r^2$  function shows superior response at low spatial frequencies (near k-space).

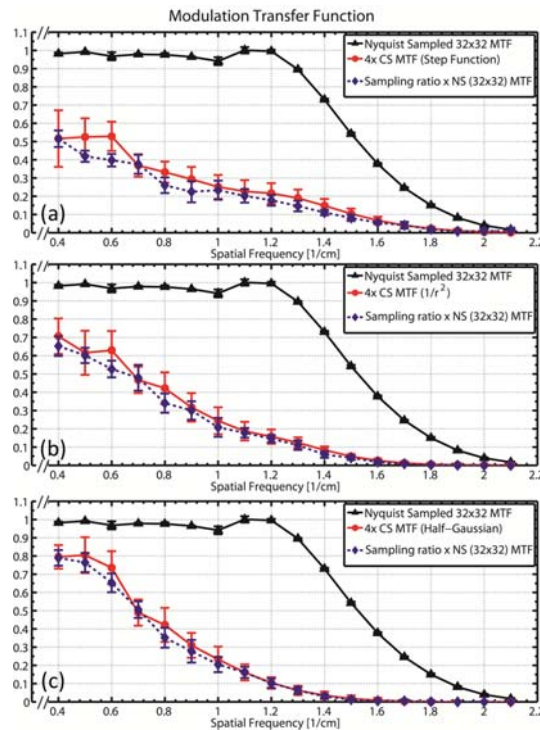


**Figure 5-6: Comparison between the CS-MTF and the sampling-modulated NS-MTF of (a) step PDF, (b)  $1/r^2$  PDF, and (c) half-Gaussian PDF**

Figure 5-6 shows the relationship between the CS-MTF (circles) and the sampling-modulated NS-MTF (diamonds) averaged over 10 k-space sampling patterns for each PDF. A strong correlation between the CS-MTF and the sampling-modulated NS-MTF ( $R^2$  of 0.964, 0.989, and 0.994) coupled with a low  $l_2$  norm of residuals (0.212, 0.152, 0.125) are noticed for the step,  $1/r^2$ , and half-Gaussian PDFs, respectively, strongly supporting our proposition in Eq. 5-1. Prediction of CS-MTF shape can hence be achieved by calculating the sampling ratio of the pattern used and the known Nyquist-sampled MTF.

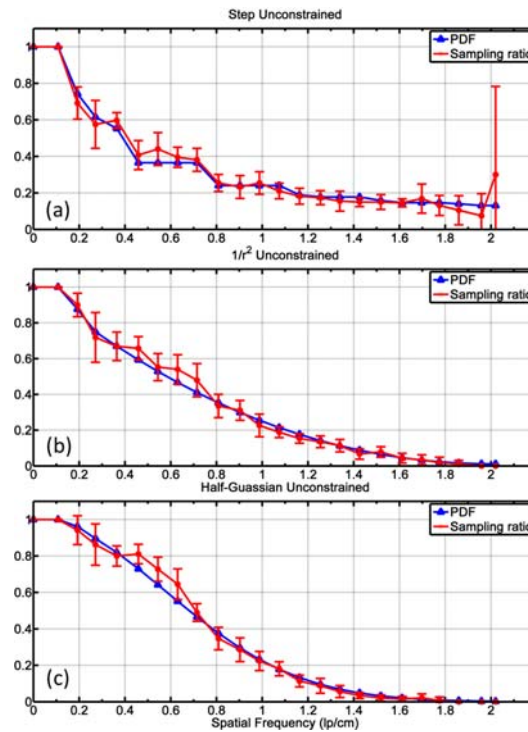


**Figure 5-7: Comparison between the prescribed PDF and the average sampling ratio for k-space sampling patterns generated using the original algorithm. (a) Step PDF. (b)  $1/r^2$  PDF. (c) Half-Gaussian PDF.**

As explained earlier, the unconstrained algorithm responsible for generating the k-space sampling pattern prioritises reducing the coherent interference caused by sub-Nyquist to produce the best sampling pattern over a number of iterations. This can lead to the cases where the resulting sampling pattern is very effective in reducing interference but whose sampling ratio is different from the prescribed PDF. This effect is illustrated

in Figure 5-7 where a consistent tendency to over sample k-space between 0.5 – 0.7 lp/cm compared to the PDF is clearly visible for all the investigated PDFs. The large error bars are indicative of the variation in sampling ratio between ten patterns produced using the same PDF. Accordingly, while the shape of the CS-MTF can be predicted knowing the sampling ratio of a sampling pattern, that response cannot be reliably predicted or influenced by knowing the PDF. Furthermore, that response is not robustly reproducible as evidenced by the relatively large error bars for CS-MTF shown in Figure 5-6.

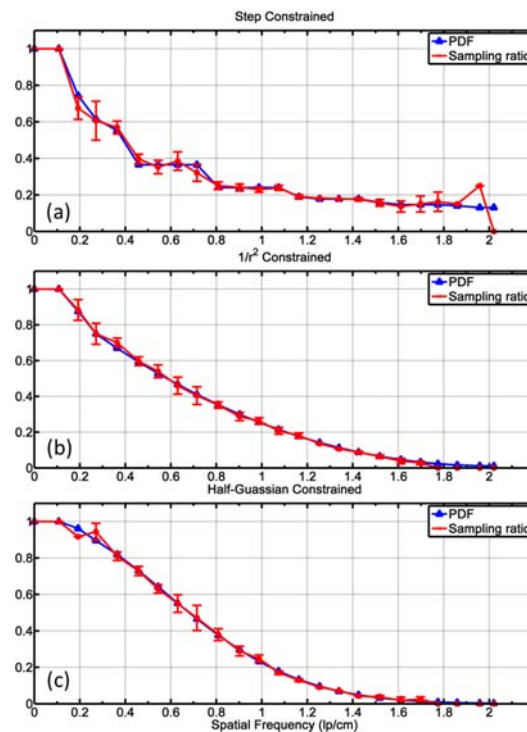


**Figure 5-8: Comparison between the prescribed PDF and the average sampling ratio for k-space sampling patterns generated using the density-constrained algorithm. (a) Step PDF. (b) 1/r<sup>2</sup> PDF. (c) Half-Gaussian PDF.**

On the other hand, the PDF-constrained k-space sampling algorithm generates patterns whose sampling ratios adhere to the prescribed PDF. Figure 5-8 shows the PDFs and sampling ratios of three sets of ten PDF-constrained patterns generated using the same PDFs used to generate the unconstrained sets shown earlier. It is clear how the sampling ratios adhere to the PDFs and the small error bars are indicative

of the small variation in sampling ratios between patterns of the same PDF.

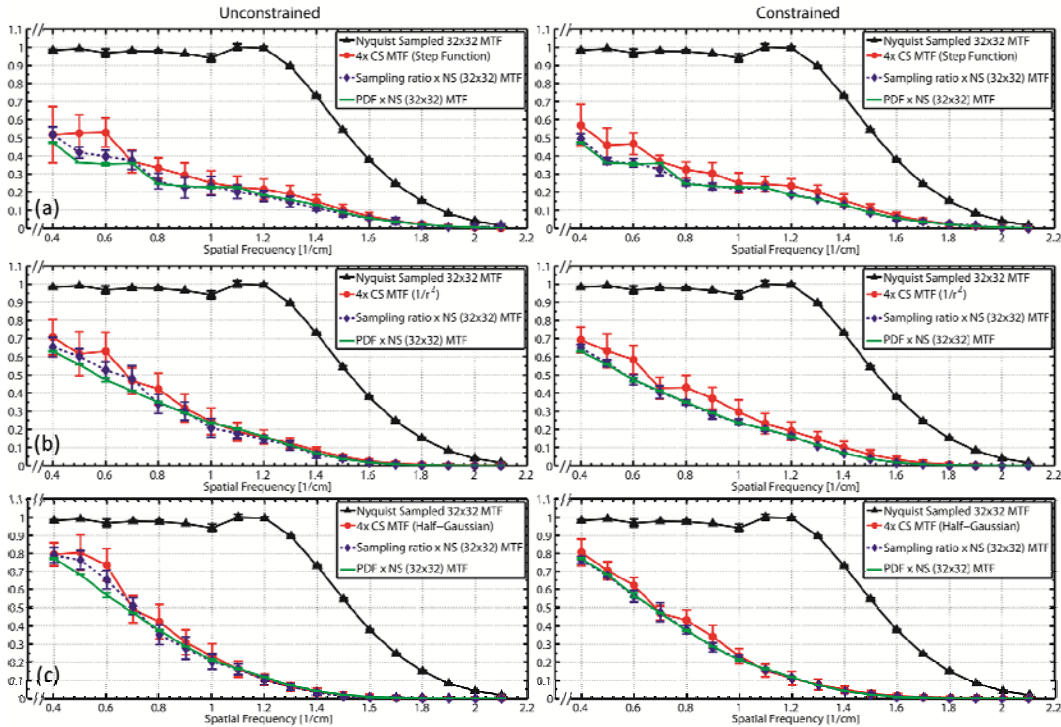


**Figure 5-9: Side-by-side comparison of the CS-MTF, the sampling-modulated NS-MTF and the PDF-modulated NS-MTF resulting from the unconstrained (left) and constrained (right) algorithms for (a) step PDF, (b) 1/r<sup>2</sup> PDF and (c) half-Gaussian PDF**

Figure 5-9 illustrates the improvement in agreement between the Nyquist sampled MTF modulated by the PDF (PDF-modulated NS-MTF) (solid line with no markers) and the CS-MTF (circles) for the constrained patterns compared to the unconstrained ones. The improvement is accompanied by a reduction in the error bars of both the CS-MTF and the sampling-modulated NS-MTF indicating a reduction in the variability of response between different sampling patterns of the same PDF and an improvement in the robustness of predicting the CS-MTF when using the PDF-constrained algorithm.

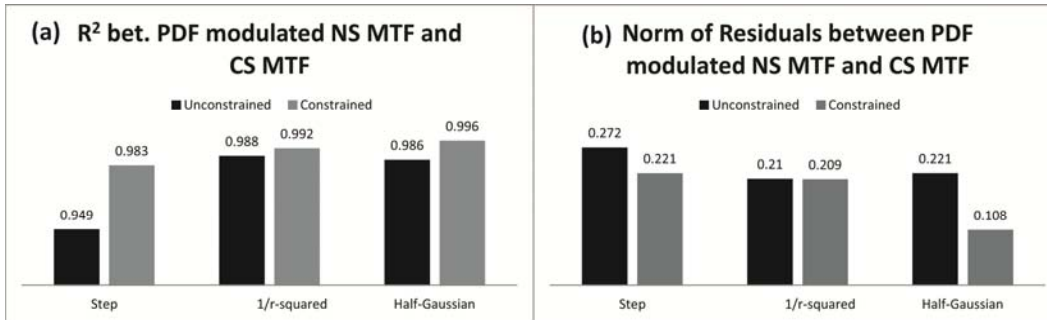


**Figure 5-10: (a) Coefficients of determination between the PDF-modulated NS-MTF and the CS-MTF for step,  $1/r^2$ , and half-Gaussian PDFs. (b) Norm of residuals between the PDF-modulated NS-MTF and the CS-MTF for step,  $1/r^2$ , and half-Gaussian PDFs.**

In addition to the visual agreement between the PDF-modulated NS-MTF and the CS-MTF to within 1 standard deviation, there is a consistent improvement in the coefficient of determination ( $R^2$ ) values with the use of density constrained sampling patterns, as detailed in Figure 5-10a. The  $l_2$  norm of residuals values shown in Figure 5-10b, show a similar improvement in agreement between the PDF-modulated NS-MTF and the CS-MTF with the use of the density constrained algorithm.

The robustness of the density constrained algorithm as evidenced in the agreement between the sampling ratio and the PDF in Fig. 5-8 and Fig. 5-9 as well as the high  $R^2$  (0.983 – 0.996) and low norms of residuals (0.108 – 0.221) between the PDF-modulated NS-MTF and CS-MTF supports the substitution of the sampling ratio with the PDF in Eq. 5-1. Therefore, the CS-MTF can be expressed as:

$$CS - MTF = PDF \times NS - MTF \quad (5-2)$$

where CS-MTF can be predicted directly by knowing the PDF of the density constrained pattern, negating the need to calculate the sampling ratio of the specific sampling pattern used. Moreover, since the PDF is a user defined function, the result is not limited to improved robustness in predicting the CS-MTF, but also provides an opportunity to

predefine/prescribe a desired CS-MTF response by means of customizing the PDF.

## **5.4 Conclusions**

In this work we have investigated the dependence of the MTF of the CS reconstructed acetate metabolite maps on the manner in which k-space is sampled in CS MRSI. As suspected initially, the sampling ratio of the patterns used for CS MRSI has a direct effect on MTF. Moreover, high  $R^2$  values are observed between the sampling-modulated NS-MTF and the CS-MTF. These  $R^2$  values and the good visual agreement between the CS-MTF and the sampling-modulated NS-MTF curves offer a means of predicting the MTF of CS MRSI. The relationship established in Eq. 5-1 provides the user with the ability to theoretically assess the MTF of CS MRSI and compare the effect of different k-space sampling patterns without the need to perform individual MTF measurements. For example, for applications where preserving low-resolution response is desired, sampling patterns generated using a half-Gaussian PDF would be more suitable than a PDF with a high probability of sampling far k-space (e.g. step function) which is more suitable for increasing the effective spatial resolution preserving response at high frequencies.

In addition, the improved agreement between the sampling ratios of patterns produced by the density constrained algorithm and the prescribing PDFs, along with improved  $R^2$  and norm of residuals values between the PDF-modulated NS-MTF and the CS-MTF support the substitution of the sampling ratio with the PDF in Eq. 5-1. This results in a solution for the MTF of CS MRSI that is not only predictable but also customizable to the user's needs. Here arises the potential for the user to prescribe a desired CS-MTF response based on the nature of the spatial frequency range of the imaged object.

Also as expected, the unconstrained algorithm used for generating the k-space sampling patterns produced sampling patterns that reduced

coherent aliasing artifacts at the cost of deviating from the prescribing PDF. The proposed density-constrained algorithm achieves the same goals while minimizing the deviation from PDF. This results in improved reproducibility, as evidenced by reduced error-bars, in sampling ratios between sampling patterns produced with the same PDF. It was also shown to improve the robustness of the CS-MTF and improve the agreement between the CS-MTF and the PDF-modulated NS-MTF.

## References

1. M. Lustig, D. Donoho and J. M. Pauly, "Sparse MRI: The application of compressed sensing for rapid MR imaging," *Magn Reson Med* **58** (6), 1182-1195 (2007).
2. S. Hu, M. Lustig, A. P. Chen, J. Crane, A. Kerr, D. A. Kelley, R. Hurd, J. Kurhanewicz, S. J. Nelson, J. M. Pauly and D. B. Vigneron, "Compressed sensing for resolution enhancement of hyperpolarized  $^{13}\text{C}$  flyback 3D-MRSI," *J Magn Reson* **192** (2), 258-264 (2008).
3. S. Hu, M. Lustig, A. Balakrishnan, P. E. Larson, R. Bok, J. Kurhanewicz, S. J. Nelson, A. Goga, J. M. Pauly and D. B. Vigneron, "3D compressed sensing for highly accelerated hyperpolarized ( $^{13}\text{C}$ ) MRSI with in vivo applications to transgenic mouse models of cancer," *Magn Reson Med* **63** (2), 312-321 (2010).
4. S. Geethanath, H. M. Baek, S. K. Ganji, Y. Ding, E. A. Maher, R. D. Sims, C. Choi, M. A. Lewis and V. D. Kodibagkar, "Compressive sensing could accelerate  $^1\text{H}$  MR metabolic imaging in the clinic," *Radiology* **262** (3), 985-994 (2012).
5. J. K. Furuyama, N. E. Wilson, B. L. Burns, R. Nagarajan, D. J. Margolis and M. A. Thomas, "Application of compressed sensing to multidimensional spectroscopic imaging in human prostate," *Magn Reson Med* **67** (6), 1499-1505 (2012).
6. A. A. Heikal, K. Wachowicz and B. G. Fallone, "MTF behavior of compressed sensing MR spectroscopic imaging," *Med Phys* **40** (5), 052302 (2013).
7. E. Candes and J. Romberg, "Signal recovery from random projections," *P Soc Photo-Opt Ins* **5674** (5674), 76-86 (2005).
8. M. J. Bostock, D. J. Holland and D. Nietlispach, "Compressed sensing reconstruction of undersampled 3D NOESY spectra: application to large membrane proteins," *Journal of biomolecular NMR* **54** (1), 15-32 (2012).
9. E. J. Candes, J. Romberg and T. Tao, "Robust uncertainty principles: Exact signal reconstruction from highly incomplete frequency information," *IEEE Trans Inform Theory* **52** (2), 489-509 (2006).
10. D. L. Donoho, "Compressed sensing," *IEEE Trans. Inform. Theory* **52**, 1289-1306 (2006).
11. A. S. Stern, D. L. Donoho and J. C. Hoch, "NMR data processing using iterative thresholding and minimum  $l_1$ -norm reconstruction," *J Magn Reson* **188**, 295-300 (2007).
12. Y. Tsaig and D. L. Donoho, "Extensions of compressed sensing," *Signal Processing* **86** (3), 549-571 (2006).
13. A. A. Heikal, K. Wachowicz, S. D. Thomas and B. G. Fallone, "A phantom to assess the accuracy of tumor delineation using MRSI," *Radiology and Oncology* **42** (4), 232-239 (2008).
14. S. Mierisova and M. Ala-Korpela, "MR spectroscopy quantitation: a review of frequency domain methods," *NMR Biomed* **14** (4), 247-259 (2001).

## Chapter Six

### 6 Conjugate mapped compressed sensing MRSI

---

#### 6.1 Introduction

As introduced in Chapters Four and Five, Compressed Sensing is a promising technique for the acceleration of acquisition especially when applied to MR spectroscopic imaging where nested phase encoding is the most common method of spatial encoding.<sup>1-6</sup> However, CS-MRSI is not a lossless technique, as has been demonstrated in the previous chapters. While CS-MRSI results in increased spatial resolution compared to its time-equivalent Nyquist sampled low-resolution counterpart (31.6% higher contrast at a threshold of 0.1 MTF for 4-times acceleration), CS-MTF has been shown to be directly dependent on the PDF used for generating the sub-Nyquist sampling pattern necessary for CS.<sup>6</sup> This results in a loss of response at spatial frequencies which are not fully sampled and ultimately leads to the loss in spatial resolution of up to 32.4% at 0.1 MTF compared to full Nyquist-sampled high-resolution reconstructions. Moreover, there is a visible decrease in response at lower frequencies even when compared to time-equivalent Nyquist sampled reconstructions. (see Fig. 4-12)

In this work we attempt to circumvent the reduced CS-MTF response caused by undersampling by exploiting the complex conjugate symmetry property of k-space. Utilizing techniques optimized in Chapter Five, we generated PDF-constrained k-space sampling patterns where redundant sampling of conjugate k-space points is avoided below a PDF of 0.5. With careful consideration to phase, unacquired points of k-space were mapped with their conjugate counterparts prior to reconstruction, boosting the apparent sampling ratio (i.e. density of k-space samples compared to Nyquist sampling). Similar to the work shown in Chapter Four, the boosted apparent sampling ratio is expected to improve the MTF

at the conjugate mapped frequencies. The reason behind this expectation is that similar to reducing the amount of undersampling, conjugate mapping is expected to reduce the number of degrees of freedom of the solution, encouraging convergence to a more accurate solution. Furthermore, the use of a PDF-constrained k-space sampling pattern should result in a relationship between the CS-MTF and the PDF-modulated NS-MTF similar to the one demonstrated in Chapter Five (Eq. 5-2).

$$CS - MTF = PDF \times NS - MTF \quad (6-1)$$

Since k-space conjugate mapping (pre-filling) up to doubles the apparent sampling ratio when combined with non-redundant sampling of conjugate points, one would expect the conjugate mapped compressed sensing (CMaCS) MTF to be up to double the corresponding CS-MTF as shown in Eq. 6-2.

$$CMaCS - MTF = \begin{cases} NS - MTF & \text{for } PDF \geq 0.5 \\ 2 \times PDF \times NS - MTF & \text{for } PDF < 0.5 \end{cases} \quad (6-2)$$

## 6.2 Theory

Recall the two dimensional MRSI signal equation (Eq. 2-49):

$$S(k_x, k_y) = \iint_{x \ y} M(x, y) e^{-i2\pi(k_x x + k_y y)} dy dx \quad (6-3)$$

where  $k_x$ , and  $k_y$  are the k-space components in the x, and y directions, respectively.

Consider the complex conjugate of Eq. 6-3<sup>7</sup>:

$$S^*(k_x, k_y) = \left( \iint_{x \ y} M(x, y) e^{-i2\pi(k_x x + k_y y)} dy dx \right)^* \quad (6-4)$$

$$S^*(k_x, k_y) = \iint_{x \ y} M(x, y)^* e^{i2\pi(k_x x + k_y y)} dy dx$$

if  $M(x, y)$  is a real function, then Eq. 6-4 becomes:

$$S^*(k_x, k_y) = \left( \int \int_{x, y} M(x, y) e^{-i2\pi(-k_x x - k_y y)} dy dx \right) \quad (6-5)$$

or <sup>7</sup>

$$S^*(k_x, k_y) = S(-k_x, -k_y) \quad (6-6)$$

which describes k-space conjugate symmetry.

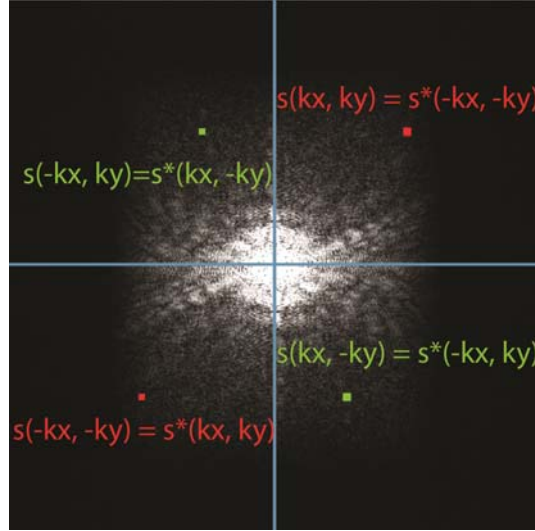


Figure 6-1: An illustration of 2-D complex conjugate symmetry in k-space

Reconstruction of the image  $m$  can now be achieved by solving the following:

$$\mathit{argmin}_m \left\| F_{u+CM} m - y_{u+CM} \right\|_2^2 + \lambda \left\| \Psi m \right\|_1 \quad (6-7)$$

where  $m$  is the desired image,  $\Psi$  is a sparsifying wavelet transform,  $\lambda$  is the reconstruction weight used for the wavelet, and  $F_{u+CM}$  is the Fourier transform at the undersampled ( $u$ ) and the conjugated mapped ( $CM$ ) locations, respectively. Similarly,  $y_{u+CM}$  is the complex conjugate augmented k-space. Similar to Eq. 4-2, the first half minimizes the  $\ell_2$  norm and hence promotes consistency between the conjugate augmented under-sampled k-space data and the corresponding points of the Fourier transform of the reconstructed image. Conversely, the second half minimizes the  $\ell_1$  norm of the sparsifying transform domain data, and hence promotes sparsity.

### 6.3 Materials and Methods

Sub-Nyquist k-space sampling patterns are generated using the PDF-constrained Monte-Carlo based pseudo-random method described in Chapter Five (Section 5.2.1).<sup>1, 3</sup> The algorithm was modified to ensure non-redundant sampling of conjugate k-space points at sampling probabilities less than or equal to 0.5. k-Space sampling patterns were generated where the total number of k-space samples acquired was 1/4, 1/5 and 1/6 of that of the fully sampled 32×32 k-space grid achieving acceleration factors of 4, 5 and 6 in scan times, respectively. Ten k-space sampling patterns were generated for each acceleration factor using a  $1/r^2$  PDF with a fully sampled radius of 2 k-space points.<sup>1, 3</sup>

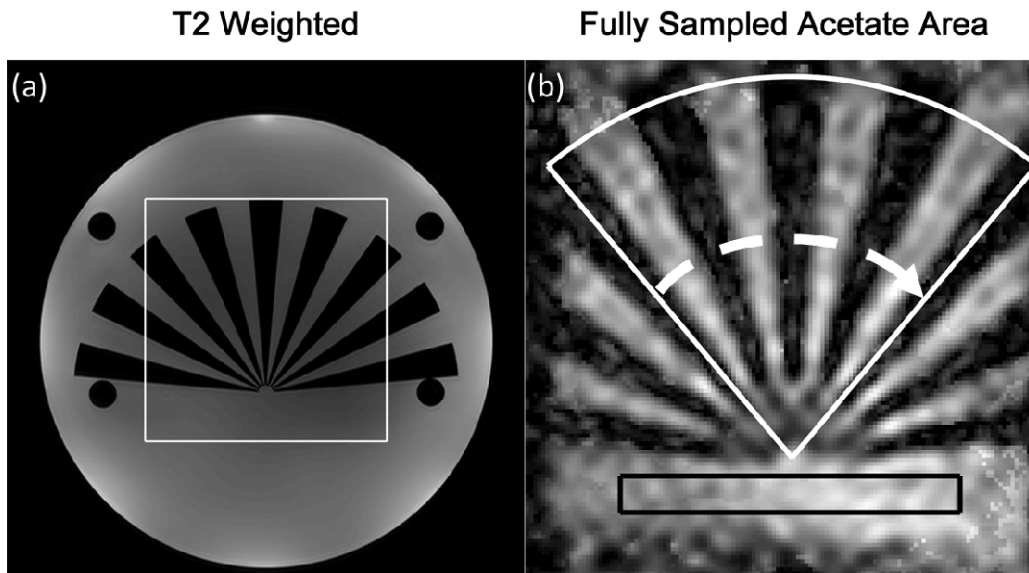


**Figure 6-2:** (a) T2-weighted image of the phantom with the white box showing the MRSI field-of-view. (b) Fully sampled acetate area map. The high-lighted pie-shaped region is the region of interest used for MTF calculation. The dashed arrow signifies the location of the arc profile shown in figure 2. The black box region is the uniform region used to normalize the arc profiles.

#### 6.3.1 Imaging sequence

Scans of the fan phantom used in Chapter Four (Section 4.3.1) (Fig. 6-2) were performed on a Philips Achieva 3 T MRI (Philips Healthcare, Bothell, WA) unit together with an 8 element head coil. To

avoid added effects of signal combination the acquisition was performed with the coil operating in quadrature mode. A 2-D Point RESolved Spectroscopy (2-D PRESS) sequence was used to scan the phantom (32×32 pixels with nominal resolution of 0.35×0.35 cm<sup>2</sup>, TR/TE of 1400/32 ms, half-echo acquisition over 512 ms, sampling rate of 2000 Hz). The slice thickness was set to 0.7 cm.

Three scans were acquired with the phantom oriented in each of four angular orientations with respect to the centre wedge; at 0°, 90°, 180° and 270° to account for asymmetries in the k-space sampling patterns and spatial non-uniformity of the imaging coil.<sup>6</sup> This data was subsampled using the optimized k-space sampling patterns to generate the compressed sensing datasets.

A two-dimensional mathematical model of the phantom was created in Matlab (The MathWorks, Natick, MA) based on the geometry and the spectral quality acquired from the 2D-PRESS scans. Three simulations with the simulated peak heights chosen together with the addition of three random noise sets to achieve a mean peak-SNR (27.8) similar to that of the acquired datasets (24.9).

### **6.3.2 Conjugate Mapped Compressed Sensing (CmaCS)**

As shown by Eq. 6-4 – Eq. 6-6, conjugate symmetry is only valid if the imaged object  $M(x,y,\sigma)$  is represented by a real function. Accordingly, proper phase estimation and adjustment is required prior to conjugate filling of the missing k-space samples. Zero-order (DC) phase estimation and adjustment was independently performed on the two-dimensional dataset at each spectral frequency. This allowed the filling of the paired k-space samples with their conjugate counterparts (Fig 6-3). This phase adjustment was subsequently reversed prior to reconstruction.

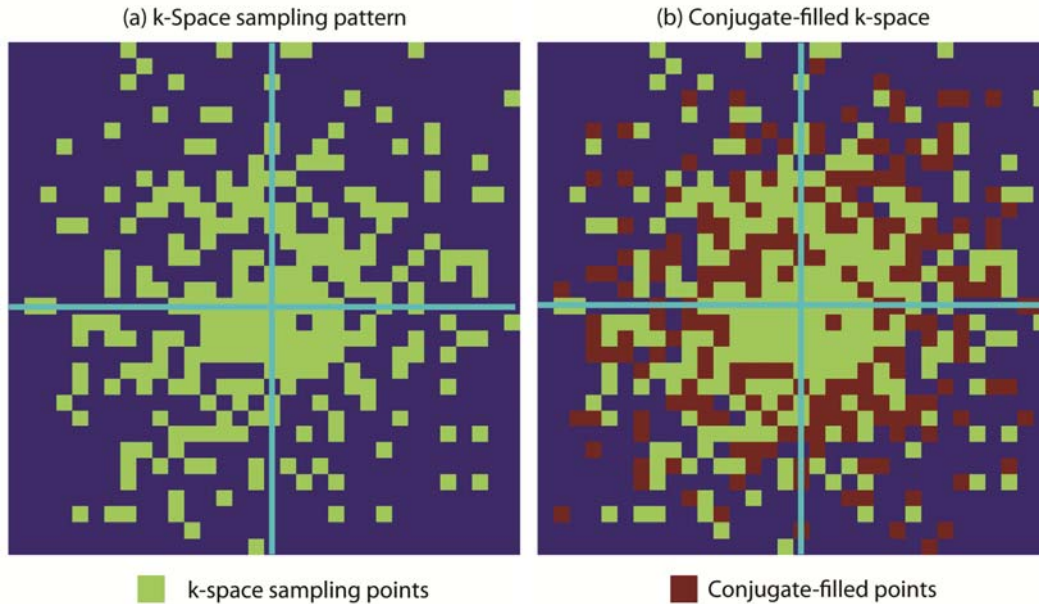


**Figure 6-3:** (a) an example of k-space sampling pattern. (b) Conjugate-filled k-space. The lines show the 4 quadrants of k-space.

### 6.3.3 Reconstruction

The CS reconstruction algorithm is based on an iterative non-linear conjugate gradient method with a line search function used in the Matlab code provided by M. Lustig (<http://www.msrl.stanford.edu/~mlustig/software>).<sup>1</sup> The code was modified in-house to work with MR spectroscopic imaging data.<sup>6</sup> A 3-D wavelet transform in the x-y-f dimensions serves as the sparsifying transform for the 3-D reconstruction.<sup>6</sup> The optimum weight for CS reconstruction was empirically determined to be 0.001. Simulations were reconstructed using the 10 k-space sampling patterns for each acceleration factor, yielding a total of 30 (3 noise sets  $\times$  10 sampling patterns/acceleration) reconstructions per acceleration factor. Similar to previous chapters, CS reconstructions were repeated with the phantom rotated 90° in-plane using the same un-rotated sampling patterns in order to account for asymmetries in the k-space sampling patterns.<sup>6</sup> This yielded a total of 60 reconstructions for each acceleration factor. For demonstration purposes, experimental scans were reconstructed using one 4-times accelerated k-

space sampling pattern yielding a total of 12 reconstruction (3 scans  $\times$  4 orientations).

For every CS-MRSI dataset, two Nyquist sampled datasets were reconstructed using the traditional 2D inverse Fourier transform: a fully sampled  $32 \times 32$  dataset and a 4-times CS-MRSI time-equivalent Nyquist-sampled low-resolution  $16 \times 16$  dataset. All datasets were reconstructed to a  $128 \times 128$  grid using zero-padding in k-space prior to spectral processing and peak-fitting.

#### **6.3.4 Processing**

The x-y-f data resulting from the CS non-linear reconstruction was inverse-Fourier transformed back to x-y-t domain to undergo the same processing steps as the Nyquist sampled data. Post reconstruction, all datasets were subjected to the same spectral processing and peak fitting steps described in Chapter Four. (Section 4.3.7)

#### **6.3.5 MTF calculation method**

The MTF calculation method explained in Section 4.3.2 was used to calculate the MTFs used in this work.<sup>6</sup> For simulations, MTF calculations were performed for 60 CS-MRSI reconstructions (2 orientations  $\times$  3 simulations  $\times$  10 sampling patterns/acceleration) and the resulting MTFs were averaged to give the final measured modulation transfer function. The same procedure was used for experimental measurements with the MTFs averaged over 12 reconstructions (4 orientations  $\times$  3 scans).

## 6.4 Results and Discussion

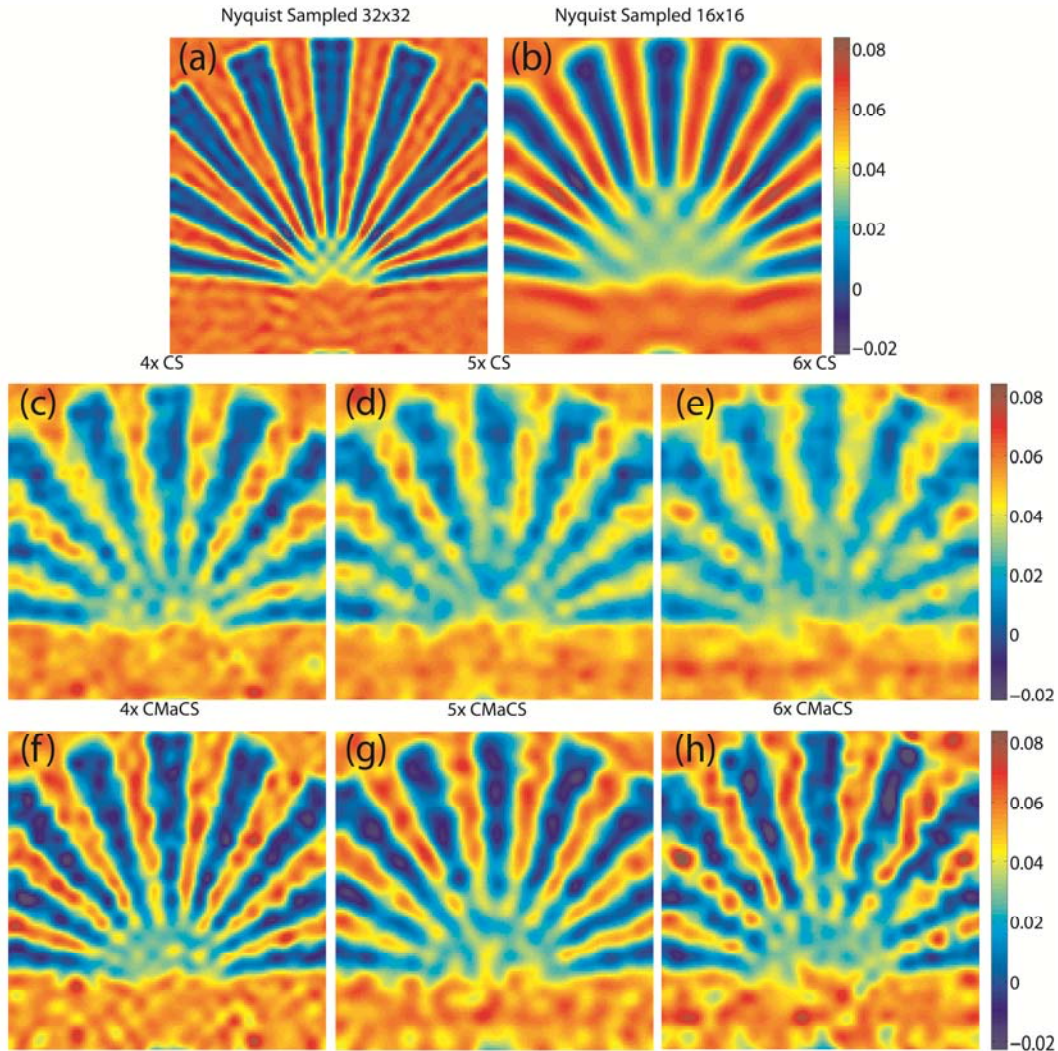


**Figure 6-4: Acetate area maps for (a) Nyquist sampled (32×32), (b) 4-times CS time-equivalent NS (16×16), (c) 4-times, (d) 5-times, (e) 6-times conventional CS, (f) 4-times, (g) 5-times, and (h) 6-times CMaCS reconstructions.**

Acetate maps reconstructed using the CMaCS technique are shown in Fig. 6-4 along with their CS counterparts. CMaCS reconstructions clearly show an overall increase in contrast particularly in the low-resolution regions of the phantom across the acceleration factors tested. There is also a small but noticeable increase in detail shown towards the centre of the fan, indicating a possible increase in spatial resolution.

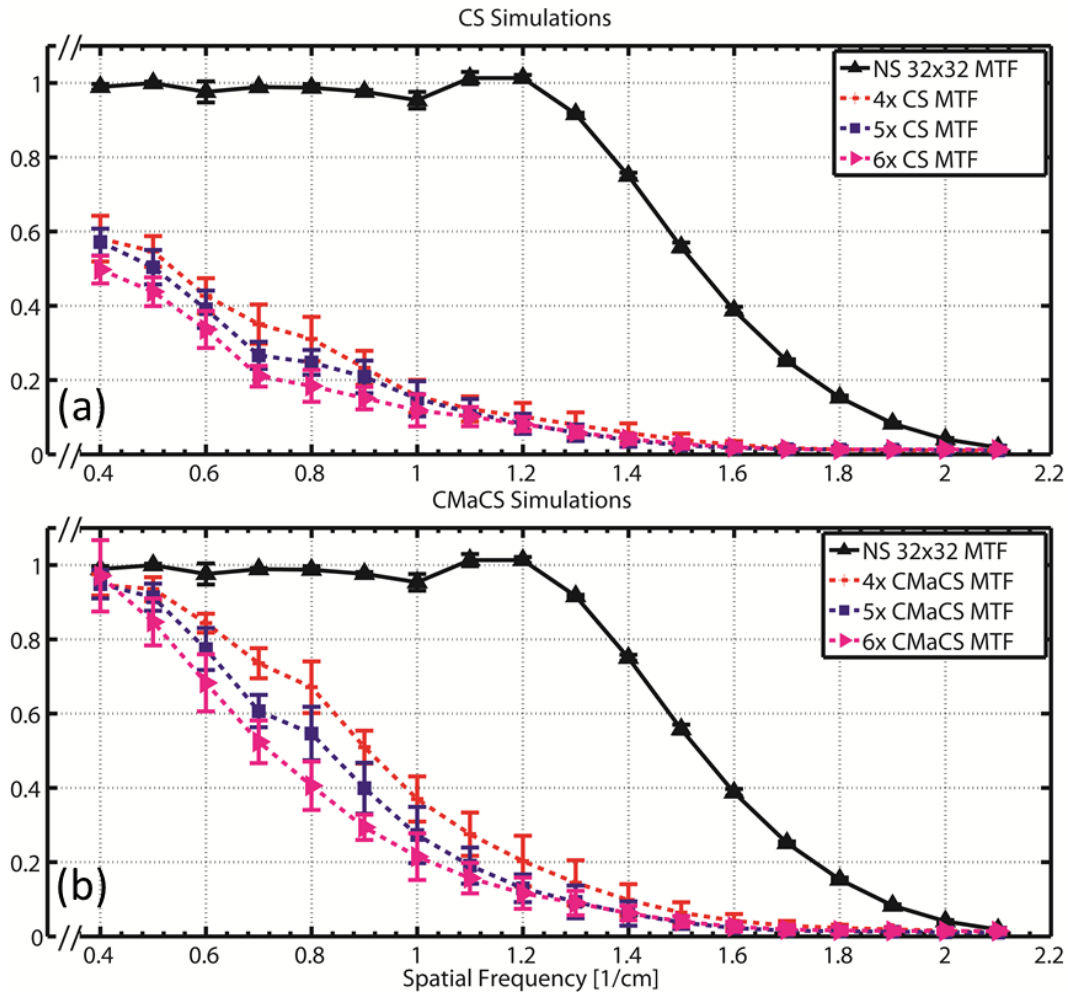


**Figure 6-5: MTFs of 4-, 5-, and 6-times accelerated reconstructions for simulated datasets using (a) conventional CS, and (b) CMaCS.**

MTFs of the reconstructions (Fig. 6-5) provide a more detailed insight into results. Fig. 6-5a is consistent with the reported and previously observed MTF for CS-MRSI.<sup>6</sup> The decreased response at low frequencies is consistent with the results of Chapter Five with a strong relation between the CS-MTF and the PDF-modulated NS-MTF ( $R^2$  of 0.993, 0.995, and 0.998 for 4-times, 5-times and 6-times acceleration, respectively). Hence, according to Eq. 5-2, CS-MTF is expected to decline steadily following the PDF (since the Nysquist sampled MTF is roughly unity at low frequencies).

On the other hand, Fig. 6-5b shows a consistent improvement in the MTF of CMaCS reconstructions by almost a factor of two. Most notably,

CMaCS-MTFs preserved a unity response up to 0.6 lp/cm for 4-times acceleration, 0.5 lp/cm for 5-times acceleration, and 0.4 lp/cm for 6-times acceleration. Moreover, spatial resolution at 0.1 MTF improved from 1.36, 1.2 and 1.1 lp/cm for 4-, 5-, and 6-times acceleration, respectively, for CS reconstructions, to 1.5, 1.35 and 1.35 lp/cm, respectively, for CmaCS reconstructions.

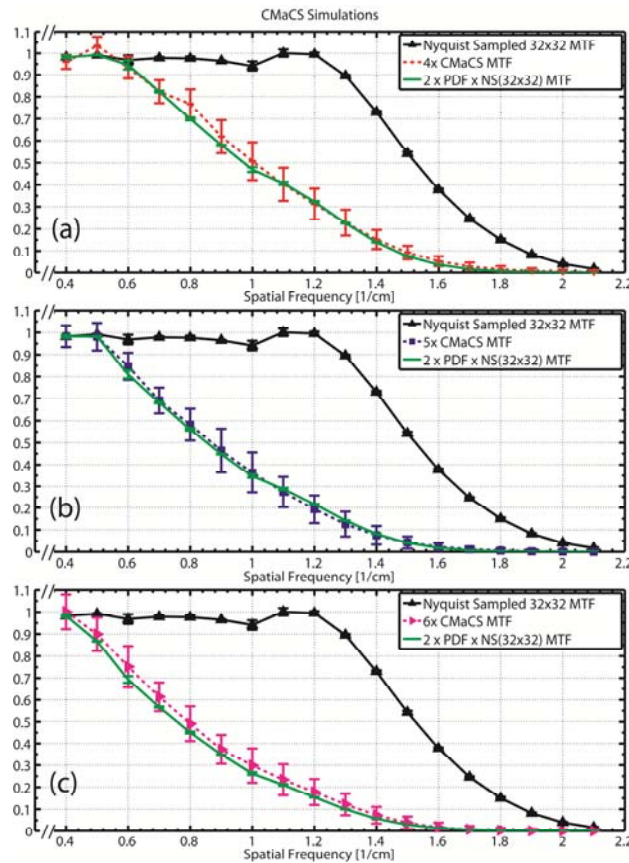


**Figure 6-6: Comparison between CMaCS-MTF and 2× PDF-modulated NS-MTF (capped at 1) for (a) 4-times, (b) 5-times, and (c) 6-times acceleration.**

Furthermore, Fig. 6-6 illustrates the strong correlation between the CMaCS-MTF and 2×PDF×NS(32×32) lines as expected by Eq. 6-2. As in the case of CS-MTF (see Chapter 5), the resulting CMaCS-MTF are highly predictably as evidenced by the high  $R^2$  scores (0.997, 0.999, and 0.999, respectively) coupled with low  $l_2$  norm of residuals (0.106, 0.060, and 0.111, respectively).

While the MTF gains of CMaCS are clearly very promising, it must not be forgotten that the above results are for simulations where it appears that Zeroth-order (DC) phase estimation was sufficient to approximate the phase adjustment needed for accurate conjugate mapping. It is very likely that real experimental data would suffer from more complicated phase shift patterns where zero-order estimation of the phase is insufficient for accurate conjugate mapping.

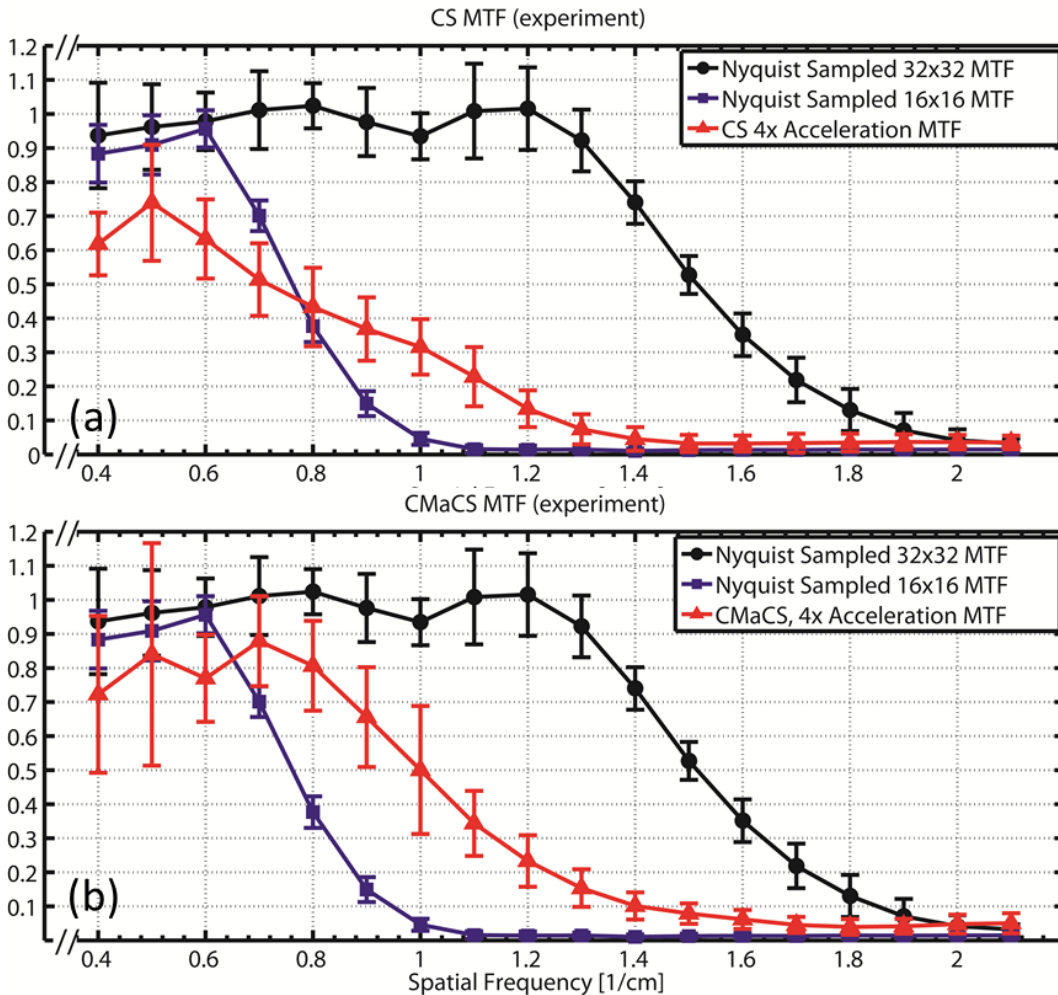


**Figure 6-7: MTFs of 4-, 5-, and 6-times accelerated reconstructions for experimentally acquired datasets using (a) conventional CS, and (b) CMaCS.**

Figure 6-7 shows the MTFs of 4-times accelerated CS and their corresponding CMaCS reconstructions for 12 experimentally acquired datasets (3 scans  $\times$  4 orientations). While there are clear gains in the case of CMaCS-MTF similar to those demonstrated in simulations, there appear

to be large error bars associated with the CMaCS-MTF at low spatial frequencies, an indication of instability in response for the 12 different experiments. That instability might be caused by phase discontinuities, or  $B_0$  field inhomogeneities causing inaccurate conjugate mapping due to inadequate phase estimation and adjustment.

### **6.5 Conclusion:**

With the cost of accelerated acquisition using Compressed Sensing evidenced as reduced response at low spatial frequencies, the aim of this work was to exploit the redundancy of k-space in the form of complex conjugate symmetry to provide prior information necessary to partially mitigate the shortcomings of CS-MRSI. Simulations have shown that with proper phase estimation and adjustment, k-space can be pre-filled (mapped) with complex conjugates of the acquired k-space samples, resulting in increasing the apparent sampling ratio by up to two-fold, and improving MTF response by the same magnitude post reconstruction (Eq. 6-2). More importantly, recovery of the MTF response to unity at low frequencies (up to 0.6 lp/cm for 4-times acceleration) was achieved with CMaCS accompanied by an overall increase in MTF response and limit-resolution at 0.1 MTF.

CMaCS reconstruction of experimentally acquired datasets showed similar improvements in MTF. A two-fold increase in MTF was noticed between CMaCS and CS reconstructions at spatial frequencies higher than 0.8 lp/cm. While improvements in MTF were also noticeable at lower frequencies, the improvements were not as pronounced as in the case of simulations.  $B_0$  inhomogeneities and sub-optimal phase adjustment, leading to inaccurate conjugate filling, are the likely causes of the discrepancies. Those issues can be addressed in the future by acquiring a low-resolution phase map or iterative higher-order phase estimation and adjustment.

Furthermore, due to the use of PDF-constrained sampling patterns, and non-redundant sampling of conjugate points, strong correlation was demonstrated between simulated CMaCS-MTF and the RHS of Eq. 6-2. Similar to the findings of Chapter Five, this indicates that CMaCS-MTF is not only predictable, but also customizable by the user, thus increasing the potential utility of the CMaCS technique.

## References

1. M. Lustig, D. Donoho and J. M. Pauly, "Sparse MRI: The application of compressed sensing for rapid MR imaging," *Magn Reson Med* **58** (6), 1182-1195 (2007).
2. S. Hu, M. Lustig, A. P. Chen, J. Crane, A. Kerr, D. A. Kelley, R. Hurd, J. Kurhanewicz, S. J. Nelson, J. M. Pauly and D. B. Vigneron, "Compressed sensing for resolution enhancement of hyperpolarized  $^{13}\text{C}$  flyback 3D-MRSI," *J Magn Reson* **192** (2), 258-264 (2008).
3. S. Hu, M. Lustig, A. Balakrishnan, P. E. Larson, R. Bok, J. Kurhanewicz, S. J. Nelson, A. Goga, J. M. Pauly and D. B. Vigneron, "3D compressed sensing for highly accelerated hyperpolarized ( $^{13}\text{C}$ ) MRSI with in vivo applications to transgenic mouse models of cancer," *Magn Reson Med* **63** (2), 312-321 (2010).
4. S. Geethanath, H. M. Baek, S. K. Ganji, Y. Ding, E. A. Maher, R. D. Sims, C. Choi, M. A. Lewis and V. D. Kodibagkar, "Compressive sensing could accelerate  $^1\text{H}$  MR metabolic imaging in the clinic," *Radiology* **262** (3), 985-994 (2012).
5. J. K. Furuyama, N. E. Wilson, B. L. Burns, R. Nagarajan, D. J. Margolis and M. A. Thomas, "Application of compressed sensing to multidimensional spectroscopic imaging in human prostate," *Magn Reson Med* **67** (6), 1499-1505 (2012).
6. A. A. Heikal, K. Wachowicz and B. G. Fallone, "MTF behavior of compressed sensing MR spectroscopic imaging," *Med Phys* **40** (5), 052302 (2013).
7. E. M. Haacke, R. W. Brown, M. R. Thompson and R. Venkatesan, *Magnetic Resonance Imaging: Physics principles and sequence design*. (John Wiley & Sons, 1999).

## Chapter Seven

### 7 Conclusion and Future Work

---

#### 7.1 Conclusion

The advancements in radiation therapy delivery techniques discussed in Chapter One highlight the importance of accurate tumor delineation as an integral part of the radiotherapy process. While the gross tumor volume (GTV) of solid tumors is usually visible and easily delineated using conventional anatomic imaging modalities, the microscopic extent, from which most recurrences originate, are only detectable using specialized biochemical imaging modalities. MRSI has been suggested as one of such modalities which can be used to delineate a biological target volume (BTV) for the purpose of identifying and targeting biological abnormalities and preventing such recurrences.<sup>1-5</sup> Unfortunately, implementation of MRSI in the radiotherapy process has been largely confined to research studies with wide clinical implementation lagging due to two main practical shortcomings: Firstly, efforts to biologically delineate tumors from MRSI have been largely subjective and inconsistent. Also, strong dependence on the scanner, scanning sequence used and peak quantification method (peak area vs. peak height), adds to the complexity of performing inter-institution studies which has been the main limiting factor in performing serial or population based studies.

Secondly, most commonly used MRSI sequences rely on nested phase encoding loops for spatial encoding, resulting in long scan times that are unsuitable for time-efficient clinical use. With the advancements in treatment delivery requiring improvement in the spatial resolution of MRSI, the associated increase in scan times has rendered MRSI increasingly harder to incorporate in everyday clinical MRI studies. The purpose of this

thesis is to tackle these two main practical hurdles to implementing MRSI in the radiotherapy process.

In Chapter Three we resorted to the statistically based CNI method of biological tumor delineation to address the subjectivity and user-dependence problems characterized above.<sup>6</sup> However, when implemented on the relatively higher spatial-resolution MRSI used in our study; we noticed that the original CNI method's assumptions need to be revised. In addition, we noticed that due to the statistical nature of the model itself, there exists a region of mixed population of normal and tumor tissues that is not accounted for in the original CNI model. It was therefore necessary to introduce adjustments to the existing method of tumor delineation to account for the observed shortfalls. We proposed a modification to the CNI method that would introduce a third region of mixed population of normal tissue and tumor to account for the increased detectable variation in the relative choline and NAA levels within normal tissue as well as the statistical uncertainty in voxel segmentation. In this manner, all the benefits of the statistical approach are preserved (namely lack of operator bias, and consistency between patients, scanners, centres, etc.) while clearly identifying which voxels have high tumor probability, and the voxels for which there is inherent ambiguity. The uncertainty region will indicate that a voxel is suspect, but at present its designation as an area to be treated will ultimately rely on the planner's experience and information gleaned from other sequences and/or modalities.

Unfortunately, it is the assertion of this work that automatic delineation of a BTV is only partially realizable using the current model. The person preparing the radiation therapy plan should have to be made aware of the limitations of the model and of the mixed-population statistical uncertainty zone.

To overcome the time-consuming nature of most MRSI sequences we decided to implement the relatively new technique of Compressed Sensing to MRSI. This thesis approached the issue of applying CS to

MRSI over three main steps: (1) development of a quantitative method to assess the utility of CS-MRSI and any associated costs in image quality, (2) correlation and prediction of the factors affecting the MTF of CS-MRSI, and (3) exploring potential methods of mitigating the shortcomings of CS-MRSI.

In Chapter Four, we developed a phantom-based method to measure the performance of MRSI which to the best of our knowledge is the first attempt to quantify the MTF of MRSI metabolite images.<sup>7</sup> Using the developed technique we investigated the MTF behaviour of CS-MRSI reconstruction, especially, the specific effects of CS reconstruction weights and peak SNR on MTF. Despite the non-linearity of the CS reconstruction process, our results showed robust MTFs with regards to peak-SNRs when proper care is taken in choosing the reconstruction weighting factor. More importantly, it was found that the optimal reconstruction weighting factor was dependent on peak SNR. Accordingly, prior knowledge of the expected peak SNR range is integral to yielding optimum MTF response of the CS reconstruction.

Moreover, when compared to Nyquist-sampled conventional MRSI reconstructions, our method was used to quantify an average decrease of 32.4% in spatial resolution in the CS-MRSI scans at 0.1 MTF compared to a loss of 48.6% for the equivalent Nyquist-sampled low-resolution scans, at 4-times acceleration. CS-MTF also showed a significant decrease in low-resolution response compared to the time-equivalent Nyquist sampled datasets; a direct cost of the increase in resolution. Such effects would have been impossible to detect using the commonly used normalized root mean square error (nRMSE) metric of deciding the optimum reconstruction weight.

With the development of an accurate, quantitative method for assessing the MTF of CS-MRSI, we set off in Chapter Five to investigate the relationship between CS-MTF and the manner in which k-space is sampled in CS-MRSI. We hypothesised that the CS-MTF is a subset of

the NS-MTF with the relationship controlled by the sampling ratio (the amount of undersampling) at each frequency. Using simulations and k-space sampling patterns produced using three different PDFs; we were able to test the hypothesis. The results showed strong visual and statistical agreement between the CS-MTFs of each of the three PDFs and their corresponding sampling-modulated NS-MTF. As such, that relationship established provides the user with the ability to theoretically assess the MTF of CS MRSI and compare the effect of different k-space sampling patterns without the need to perform individual MTF measurements.

Moreover, we successfully demonstrated that PDF-constrained k-space sampling patterns improved the agreement between the CS-MTS and the PDF-modulated NS-MTF, which results in a solution for the MTF of CS-MRSI that is not only predictable but also customizable to the user's needs. This provides the user with the potential to prescribe a desired CS-MTF response based on the nature of the spatial frequency range of the imaged object. For example, for applications where preserving low-resolution response is desired, sampling patterns generated using a half-Gaussian PDF would be more suitable than a PDF with a high probability of sampling far k-space (e.g. step function) which is more suitable for increasing the effective spatial resolution preserving response at high frequencies.

Finally, with the cost of accelerated acquisition using Compressed Sensing quantifiable and controllable by the user's choice of undersampling scheme, Chapter Six aimed to exploit the redundancy of k-space to provide prior information necessary to circumvent the short comings of CS-MRSI, namely, the reduced response at low spatial frequencies. Exploiting complex conjugate symmetry, we used simulations to demonstrate that provided proper phase estimation and adjustment, k-space can be pre-filled (mapped) with complex conjugates of the acquired k-space samples prior to CS reconstruction, increasing the apparent

sampling ratio by up to two-fold and the resulting CS-MTF response post reconstruction by the same magnitude.

More importantly, CMaCS reconstruction of experimentally acquired datasets showed similar improvements in MTF. With up to a two-fold increase in MTF noticeable between CMaCS and CS reconstructions at high-frequencies ( $> 0.8$  lp/cm) and more moderate improvement at lower frequencies, there is little doubt that provided proper phase estimation, CMaCS provides a costless improvement in response, compared to conventional CS-MRSI. However, full recovery of experimentally acquired CMaCS-MTF to levels similar to simulations has proven more complicated due to  $B_0$  inhomogeneities and sub-optimal phase adjustment, leading to inaccurate conjugate filling.

In conclusion, we believe that the work in this Thesis provides two essential steps towards wide clinical implementation of MRSI-based BTV delineation. The proposed modifications to the CNI method coupled with the application of CS to MRSI address the two main obstacles outlined in the beginning of this Chapter. However, there continues to be room for improvement and questions that need to be answered by future research as outlined below.

## **7.2 Future Work**

The interpretation of the voxels in the uncertainty region of the modified CNI method is at present not straightforward. Future work utilizing additional information extracted from serial studies or full two-dimensional correlation with histology in animal models may hopefully lead to an educated classification of this region.

Also, a more accurate method of phase estimation and adjustment is needed to maximize the gains of applying CMaCS on experimental datasets. This can be achieved by acquiring a low-resolution phase map or iterative higher-order phase estimation and adjustment.

Furthermore, a comparative study of automatic tumor delineation using conventional Nyquist-sampled MRSI vs. CS- and CMaCS-MRSI is needed to identify the effect of acceleration on tumor definition. The study should also attempt to define the PDF and acceleration factors that most optimally minimize the cost in inaccurate tumor delineation while maximizing the time gains.

## References

1. J. Chang, S. Thakur, G. Perera, A. Kowalski, W. Huang, S. Karimi, M. Hunt, J. Koutcher, Z. Fuks, H. Amols and A. Narayana, "Image-fusion of MR spectroscopic images for treatment planning of gliomas," *Med. Phys.* **33** (1), 32-40 (2006).
2. A. Di Costanzo, T. Scarabino, F. Trojsi, G. M. Giannatempo, T. Popolizio, D. Catapano, S. Bonavita, N. Maggialezzi, M. Tosetti, U. Salvolini, V. A. d'Angelo and G. Tedeschi, "Multiparametric 3T MR approach to the assessment of cerebral gliomas: tumor extent and malignancy," *Neuroradiology* **48** (9), 622-631 (2006).
3. S. J. Nelson, E. Graves, A. Pirzkall, X. Li, A. A. Chan, D. B. Vigneron and T. R. McKnight, "In Vivo molecular imaging for planning radiation therapy of gliomas: an application of 1H MRSI," *J. Magn. Reson. Imaging* **16** (4), 464-476 (2002).
4. A. Pirzkall, X. Li, J. Oh, S. Chang, M. S. Berger, D. A. Larson, L. J. Verhey, W. P. Dillon and S. J. Nelson, "3D MRSI for resected high-grade gliomas before RT: tumor extent according to metabolic activity in relation to MRI," *Int. J. Radiat. Oncol. Biol. Phys.* **59** (1), 126-137 (2004).
5. K. E. Wallner, J. H. Galicich, G. Krol, E. Arbit and M. G. Malkin, "Patterns of failure following treatment for glioblastoma multiforme and anaplastic astrocytoma," *Int. J. Radiat. Oncol. Biol. Phys.* **16** (6), 1405-1409 (1989).
6. T. R. McKnight, S. M. Noworolski, D. B. Vigneron and S. J. Nelson, "An automated technique for the quantitative assessment of 3D-MRSI data from patients with glioma," *Journal of magnetic resonance imaging : JMIR* **13** (2), 167-177 (2001).
7. A. A. Heikal, K. Wachowicz and B. G. Fallone, "MTF behavior of compressed sensing MR spectroscopic imaging," *Med Phys* **40** (5), 052302 (2013).

## Bibliography

---

1. E. Alexander, 3rd and J. S. Loeffler, *Seminars in surgical oncology* **14** (1), 43-52 (1998).
2. P. B. Barker, D. O. Hearshen and M. D. Boska, *Magn. Reson. Med.* **45** (5), 765-769 (2001).
3. J. Bishop and D. Plewes, presented at the 10th Annual Mtg. Soc. Magn. Reson. In Med., San Francisco, 1991 (unpublished).
4. F. Block, *Physical Review* **70**, 460-474 (1946).
5. M. J. Bostock, D. J. Holland and D. Nietlispach, *Journal of biomolecular NMR* **54** (1), 15-32 (2012).
6. P. A. Bottomly, US Patent No. 4,480,228 (1984).
7. R. N. Bracewell, *The Fourier Transform and its Applications*. (McGraw-Hill, 1978).
8. A. Brandes, M. Soesan and M. V. Fiorentino, *Anticancer research* **11** (2), 719-727 (1991).
9. M. J. Bronskill, presented at the AAPM summer school proceeding, 1992 (unpublished).
10. E. Candes and J. Romberg, *P Soc Photo-Opt Ins* **5674** (5674), 76-86 (2005).
11. E. J. Candes, J. Romberg and T. Tao, *IEEE Trans Inform Theory* **52** (2), 489-509 (2006).
12. J. Chang, S. Thakur, G. Perera, A. Kowalski, W. Huang, S. Karimi, M. Hunt, J. Koutcher, Z. Fuks, H. Amols and A. Narayana, *Med. Phys.* **33** (1), 32-40 (2006).
13. S. Chen, D. Donoho and M. Saunders, *SIAM J. Sci. Comput.* **20** (1), 33-61 (1999).
14. S. E. Combs, S. Konkel, D. Schulz-Ertner, M. W. Munter, J. Debus, P. E. Huber and C. Thilmann, *Radiat. Oncol.* **1**, 23 (2006).
15. I. Daubechies, M. Defrise and C. D. Mol, *Commun. Pure. Appl. Math.* **57**, 1413-1457 (2004).
16. A. Di Costanzo, T. Scarabino, F. Trojsi, G. M. Giannatempo, T. Popolizio, D. Catapano, S. Bonavita, N. Maggialetti, M. Tosetti, U. Salvolini, V. A. d'Angelo and G. Tedeschi, *Neuroradiology* **48** (9), 622-631 (2006).
17. D. Donoho, M. Elad and V. Temlyakov, *IEEE Trans Inform Theory* **52**, 6-18 (2006).
18. D. L. Donoho, *IEEE Trans. Inform. Theory* **52**, 1289-1306 (2006).
19. M. Elad, B. Matalon and M. Zibulevsky, *J. Appl. Comput. Harmonic. Anal.* **23**, 346-367 (2007).
20. H. A. Fine, K. B. Dear, J. S. Loeffler, P. M. Black and G. P. Canellos, *Cancer* **71** (8), 2585-2597 (1993).
21. J. Frahm, H. Bruhn, M. L. Gyngell, K. D. Merboldt, W. Hanicke and R. Sauter, *Magn. Reson. Med.* **11** (1), 47-63 (1989).
22. R. Freeman, *J. of Progress in NMR Spectroscopy* **32**, 59-106 (1998).

23. M. J. Fulham, A. Bizzi, M. J. Dietz, H. H. Shih, R. Raman, G. S. Sobering, J. A. Frank, A. J. Dwyer, J. R. Alger and G. D. Chiro, *Radiology* **185** (3), 675-686 (1992).
24. C. D. Fuller, C. R. J. Thomas, A. Wong, S. X. Cavanaugh, B. J. Salter, T. S. Herman and M. Fuss, *Radiother. Oncol.* **81** (1), 65-72 (2006).
25. J. K. Furuyama, N. E. Wilson, B. L. Burns, R. Nagarajan, D. J. Margolis and M. A. Thomas, *Magn Reson Med* **67** (6), 1499-1505 (2012).
26. J. K. Furuyama, N. E. Wilson, B. L. Burns, R. Nagarajan, D. J. Margolis and M. A. Thomas, *Magn Res Med* **67**, 1499-1505 (2012).
27. S. Geethanath, H.-M. Baek, S. K. Ganji, Y. Ding, E. A. Maher, R. D. Sims, C. Choi, M. A. Lewis and V. D. Kodibagkar, *Radiology* **262** (3) (2012).
28. S. Geethanath, H. M. Baek, S. K. Ganji, Y. Ding, E. A. Maher, R. D. Sims, C. Choi, M. A. Lewis and V. D. Kodibagkar, *Radiology* **262** (3), 985-994 (2012).
29. R. E. Gordon and R. J. Ordidge, presented at the Abstracts of the Society of Magnetic Resonance in Medicine 3rd Annual Meeting, New York, 1984 (unpublished).
30. E. M. Haacke, R. W. Brown, M. R. Thompson and R. Venkatesan, *Magnetic Resonance Imaging: Physics principles and sequence design*. (John Willey & Sons, 1999).
31. A. A. Heikal, K. Wachowicz and B. G. Fallone, *Med Phys* **40** (5), 052302 (2013).
32. A. A. Heikal, K. Wachowicz, S. D. Thomas and B. G. Fallone, *Radiology and Oncology* **42** (4), 232-239 (2008).
33. C. F. Hess, J. C. Schaaf, R. D. Kortmann, M. Schabet and M. Bamberg, *Radiother. Oncol.* **30** (2), 146-149 (1994).
34. W. S. Hinshaw, presented at the Proceeding of the IEEE, 1983 (unpublished).
35. F. A. Howe, S. J. Barton, S. A. Cudlip, M. Stubbs, D. E. Saunders, M. Murphy, P. Wilkins, K. S. Opstad, V. L. Doyle, M. A. McLean, B. A. Bell and J. R. Griffiths, *Magn. Res. Med.* **49**, 223-232 (2003).
36. S. Hu, M. Lustig, A. Balakrishnan, P. E. Larson, R. Bok, J. Kurhanewicz, S. J. Nelson, A. Goga, J. M. Pauly and D. B. Vigneron, *Magn Reson Med* **63** (2), 312-321 (2010).
37. S. Hu, M. Lustig, A. P. Chen, J. Crane, A. Kerr, D. A. Kelley, R. Hurd, J. Kurhanewicz, S. J. Nelson, J. M. Pauly and D. B. Vigneron, *J Magn Reson* **192** (2), 258-264 (2008).
38. G. Kantor, H. Loiseau, A. Vital and J. J. Mazon, *Cancer Radiother* **5** (5), 571-580 (2001).
39. S. J. Kim, K. Koh, M. Lustig and S. Boyd, presented at the Proc. of IEEE International Conference on Image Processing (ICIP), San Antonio, 2007 (unpublished).
40. P. Kleihues, D. N. Louis, B. W. Scheithauer, L. B. Rorke, G. Reifenberger, P. C. Burger and W. K. Cavenee, *Journal of neuropathology and experimental neurology* **61** (3), 215-225; discussion 226-219 (2002).

41. K. Kristiansen, S. Hagen, T. Kollevold, A. Torvik, I. Holme, R. Nesbakken, R. Hatlevoll, M. Lindgren, A. Brun, S. Lindgren, G. Notter, A. P. Andersen and K. Elgen, *Cancer* **47** (4), 649-653 (1981).
42. S. A. Kwee, M. N. Coel, J. Lim and J. P. Ko, *J. Neuroimaging* **14** (3), 285-289 (2004).
43. N. Laperriere, L. Zuraw and G. Cairncross, *Radiotherapy and oncology : journal of the European Society for Therapeutic Radiology and Oncology* **64** (3), 259-273 (2002).
44. U. Lassen, P. E. Kristjansen, A. Wagner, M. Kosteljanetz and H. S. Poulsen, *J. Neurooncol.* **42** (2), 161-166 (1999).
45. M. Law, S. Yang, H. Wang, J. S. Babb, G. Johnson, S. Cha, E. A. Knopp and D. Zagzag, *AJNR. American journal of neuroradiology* **24** (10), 1989-1998 (2003).
46. S. W. Lee, B. A. Fraass, L. H. Marsh, K. Herbort, S. S. Gebarski, M. K. Martel, E. H. Radany, A. S. Lichter and H. M. Sandler, *Int. J. Radiat. Oncol. Biol. Phys.* **43** (1), 79-88 (1999).
47. X. Li, H. Jin, Y. Lu, J. Oh, S. Chang and S. J. Nelson, *NMR Biomed.* **17** (1), 10-20 (2004).
48. C. C. Ling, J. Humm, S. Larson, H. Amols, Z. Fuks, S. Leibel and J. A. Koutcher, *Int. J. Radiat. Oncol. Biol. Phys.* **47** (3), 551-560 (2000).
49. D. N. Louis, H. Ohgaki, O. D. Wiestler, W. K. Cavenee, P. C. Burger, A. Jouvret, B. W. Scheithauer and P. Kleihues, *Acta neuropathologica* **114** (2), 97-109 (2007).
50. M. Lustig, D. Donoho and J. M. Pauly, *Magn Reson Med* **58** (6), 1182-1195 (2007).
51. M. Lustig, J. M. Santos, D. L. Donoho and J. M. Pauly, *Proc. of 14th Annual Meeting of ISMRM*, 2420 (2006).
52. P. R. Luyten, A. J. Marien, W. Heindel, P. H. van Gerwen, K. Herholz, J. A. den Hollander, G. Friedmann and W. D. Heiss, *Radiology* **176** (3), 791-799 (1990).
53. B. M.A. and R. C. Semelka, *MRI Basic Principles and Applications*. (John Wiley & Sons, 1995).
54. A. Magalhaes, W. Godfrey, Y. Shen, J. Hu and W. Smith, *Acad. Radiol.* **12**, 51-57 (2005).
55. T. R. McKnight, S. M. Noworolski, D. B. Vigneron and S. J. Nelson, *Journal of magnetic resonance imaging : JMRI* **13** (2), 167-177 (2001).
56. T. R. McKnight, M. H. von dem Bussche, D. B. Vigneron, Y. Lu, M. S. Berger, M. W. McDermott, W. P. Dillon, E. E. Graves, A. Pirzkall and S. J. Nelson, *J Neurosurg* **97**, 794-802 (2002).
57. D. W. McRobbie, *Phys. Med. Biol.* **31** (6), 613-626 (1986).
58. S. Mierisova and M. Ala-Korpela, *NMR Biomed* **14** (4), 247-259 (2001).
59. S. M. Mohapatra, J. D. Turley, J. R. Prince, J. C. Blechinger and D. A. Wilson, *Med Phys* **18** (6), 1141-1144 (1991).
60. S. J. Nelson, E. Graves, A. Pirzkall, X. Li, A. A. Chan, D. B. Vigneron and T. R. McKnight, *J. Magn. Reson. Imaging* **16** (4), 464-476 (2002).

61. D. G. Nishimura, *Principles of Magnetic Resonance Imaging*. (Stanford University, 1996).
62. R. J. Ordidge, M. R. Bendall, R. E. Gordon and A. Connelly, *Magnetic Resonance in Biology and Medicine*. (McGraw-Hill, New Delhi, 1985).
63. J. Pallud, B. Devaux, F. Nataf, F. X. Roux and C. Dumas-Duport, *Neurochirurgie*. **51** (3-4), 253-259 (2005).
64. A. Pirzkall, X. Li, J. Oh, S. Chang, M. S. Berger, D. A. Larson, L. J. Verhey, W. P. Dillon and S. J. Nelson, *Int. J. Radiat. Oncol. Biol. Phys.* **59** (1), 126-137 (2004).
65. M. C. Preul, Z. Caramanos, D. L. Collins, J. G. Villemure, R. Leblanc, A. Olivier, R. Pokrupa and D. L. Arnold, *Nat. Med.* **2** (3), 323-325 (1996).
66. E. M. Purcell, H. C. Torrey and R. B. Pound, *Physical Review* **69**, 37-38 (1946).
67. D. Rades, F. Fehlaue, J. Wrobley, D. Albers, S. E. Schild and R. Schmidt, *Oral Oncol.* doi:10.1016/j.oraloncology.2006.05.006. (2006).
68. M. D. Robson, J. C. Gore and R. T. Constable, *Magn. Reson. Med.* **38** (5), 733-740 (1997).
69. J. Sánchez-González, J. Tsao, U. Dydak, M. Desco, P. Boesiger and K. P. Pruessmann, *Magn Reson Med* **55** (2), 287-295 (2006).
70. C. M. Segebarth, D. F. Baleriaux, P. R. Luyten and J. A. den Hollander, *Magn. Reson. Med.* **13** (1), 62-76 (1990).
71. H. Shimizu, T. Kumabe, T. Tominaga, T. Kayama, K. Hara, Y. Ono, K. Sato, N. Arai, S. Fujiwara and T. Yoshimoto, *Am. J. Neuroradiol.* **17** (4), 737-747 (1996).
72. J. L. Starck, M. Elad and D. Donoho, *IEEE Trans. Image. Process.* **14**, 1570-1582 (2005).
73. M. C. Steckner, D. J. Drost and F. S. Prato, *Med. Phys.* **21** (3), 483-489 (1994).
74. A. S. Stern, D. L. Donoho and J. C. Hoch, *J Magn Reson* **188**, 295-300 (2007).
75. S. D. Thomas, University of Alberta, 2001.
76. Y. Tsaig and D. L. Donoho, *Signal Processing* **86** (3), 549-571 (2006).
77. J. Van Dyk, *The Modern Technology of Radiation Oncology*. (Medical Physics Publishing, 1999).
78. J. Walecki, E. Tarasow, B. Kubas, Z. Czernicki, J. Lewko, J. Podgorski, M. Sokol and P. Grieb, *Acad. Radiol.* **10** (2), 145-153 (2003).
79. K. E. Wallner, J. H. Galicich, G. Krol, E. Arbit and M. G. Malkin, *Int. J. Radiat. Oncol. Biol. Phys.* **16** (6), 1405-1409 (1989).
80. D. Xu, A. P. Chen, C. Cunningham, J. A. Osorio, S. J. Nelson and D. B. Vigneron, *J. Magn. Reson. Imaging* **24** (1), 69-74 (2006).
81. M. J. Zelefsk, H. Chan, M. Hunt, Y. Yamada, A. M. Sippy and H. Amols, *J. Urol.* **176** (4), 1415-1419 (2006).